

---

# Monitoring of Microwave Liver Ablation by Surface Body-matched Antennas



## Dissertation

zur Erlangung des akademischen Grades

## Doktoringenieur (Dr.-Ing)

von:

M.Sc. Muhammad Saad Khan

geb. am 15. November 1985 in Abbottabad, Pakistan

genehmigt durch die Fakultät für Elektrotechnik und Informationstechnik  
der Otto-von-Guericke Universität Magdeburg

Gutachter:

Prof. Dr. rer. nat. Georg Rose

Prof. Dr. -ing. habil. Holger Maune

Prof. Dr. Bernd Schweizer

Promotionskolloquium am 25. Oktober 2023

---

**Khan, Muhammad Saad:**

*Monitoring of Microwave Liver Ablation by Surface Body-matched Antennas*

Ph.D. Thesis , Otto-von-Guericke University

Magdeburg, 2023.

# Contents

## Abstract

### 1 Introduction

1.1 Motivation . . . . .	2
1.2 Aim of this Thesis . . . . .	3
1.3 Structure of this Thesis . . . . .	3

### 2 Clinical and Technical Background

2.1 Hyperthermia: Ultrasound, RF, Microwave and laser Ablation . . . . .	7
2.2 Dielectric Properties of Liver . . . . .	9
2.3 Microwave Ablation in Liver . . . . .	10

### 3 Concept Design

3.1 Proposed non-invasive Methods for Microwave Ablation Monitoring	13
3.2 Concept design approach . . . . .	15
3.3 Transmission based method . . . . .	17

### 4 Theoretical and Mathematical Modeling

4.1 Permittivity and conductivity of tissue materials . . . . .	19
4.2 Propagation of electromagnetic waves in liver . . . . .	21
4.3 Thermal propagation in biological tissues . . . . .	23

### 5 Materials and Methods

5.1 High power RF Source . . . . .	26
5.2 Materials under Test . . . . .	28
5.2.1 Animal Liver . . . . .	28
5.2.2 Sweet Potatoes . . . . .	30
5.2.3 Liver Phantoms . . . . .	32
5.3 Experimental Setup . . . . .	38
5.3.1 Setup for Liver phantom experiments . . . . .	38
5.3.2 Setup for transmission through sweet potato . . . . .	41
5.3.3 Ex-vivo Liver Ablation Setup . . . . .	43

### 6 Simulations and Measurements

6.1 Microwave applicator design . . . . .	47
6.2 Body-matched Antennas . . . . .	52

---

6.2.1	Bowtie-slot BMA . . . . .	52
6.2.2	Circular Patch BMA . . . . .	56
6.3	Microwave transmission through liver phantoms . . . . .	64
6.4	Microwave ablation in sweet potatoes . . . . .	68
6.5	Ex-vivo microwave ablation in animal liver . . . . .	75
<b>7</b>	<b>Summary and Outlook</b>	
7.1	Discussion . . . . .	83
7.1.1	Microwave applicator . . . . .	83
7.1.2	Body-matched antennas . . . . .	84
7.1.3	Transmission through liver phantoms . . . . .	85
7.1.4	MWA monitoring in sweet potatoes . . . . .	86
7.1.5	MWA monitoring in ex-vivo liver . . . . .	88
7.2	Comparison . . . . .	90
7.3	Conclusion . . . . .	92
<b>A</b>	<b>Notations and Abbreviations</b>	
<b>B</b>	<b>List of Figures</b>	
<b>C</b>	<b>List of Tables</b>	
<b>D</b>	<b>Bibliography</b>	

---

## Abstract

---

Microwave liver ablation monitoring is a current research issue. In this work, a transmission-based method is proposed to correlate the growth in the ablation zone in the liver during microwave ablation to the power received on the liver surface. A surface antenna matched to the liver is used to receive the signal from a microwave applicator inserted in three different kinds of materials: phantom materials mimicking the dielectric properties of liver, sweet potatoes which have similar dielectric properties as liver, and ex-vivo animal liver. The measured results are corroborated by the simulation and the results obtained from the theoretical model developed for the transmission of EM waves from a hot liver to a cold liver. A correlation is found between growth in the ablation zone and the received power at the surface antenna. The 2.4-2.5 GHz ISM band is used for microwave ablation in this work.

During this work, different phantom materials are prepared using Polyvinylpyrrolidone and Triton X-100 materials for mimicking the dielectric properties of the liver. Moreover, the capacitance model is used to derive the mathematical formulation to calculate the dielectric properties of these phantom materials from the measurement of reflection loss of a dielectric probe in the phantom materials for different frequencies and temperatures. Moreover, a high-power microwave source is developed from off-the-shelf components for stimulating high power up to 80 W in the materials under test. The surface antennas are designed for body-matched application which in this case is the liver. The designs of linearly polarized bowtie-slot surface and submerged (dipped) antennas are presented. For orientation independence in the azimuth plane for placing the antenna on the liver surface, a circularly polarized circular patch antenna is designed with and without a matching medium which enhances the performance of the circular patch antenna. Secondly, the design of a single-slot microwave applicator is presented which is used to stimulate high power in materials under test used during this work. The antennas are designed using CST studio suite 2020.

Two types of simulations are performed in this work. In the first simulation, the transmission of EM wave through a two-layer model consisting of a hot and a cold liver similar to the theoretical model is simulated. The second is an EM-thermal co-simulation which is carried out for obtaining different temperature profiles at different time instants while stimulating 50 W power in the liver at 2.45 GHz. Then using these temperature profiles resulting in the temperature-dependent dielectric properties variation, the EM simulations are carried out to see the variation in the received power on the surface antenna. The second simulation approach is the equivalent of monitoring changes in the received power on a surface antenna during microwave ablation in an ex-vivo liver. Corresponding to these simulations, experiments are performed with the hot and cold liver phantoms, sweet potatoes, and animal livers. There is a measured increase of 4.5 dB in the received power in two-layer phantom experiments when the

hot liver tissue radius increases from 1 cm to 2 cm for an overall distance of 4 cm between the microwave applicator and the dipped antenna. On the other hand, there is a 3 dB measured loss in the received power after 10 minutes of microwave ablation in the ex-vivo liver with 50 W microwave power at 2.45 GHz when the distance between the applicator and the antenna is again 4 cm. The change in received power is related to the growth in the ablation zone. Hence, the transmission-based method for monitoring microwave ablation in the liver is validated.

---

## Kurzfassung

---

Die Überwachung der Leberablation durch Mikrowellen ist ein aktuelles Forschungsthema. In dieser Arbeit wird eine transmissionsbasierte Methode vorgeschlagen, um das Wachstum in der Ablationszone in der Leber während der Mikrowellenablation mit der auf der Leberoberfläche empfangenen Leistung zu korrelieren. Eine an die Leber angepasste Oberflächenantenne wird verwendet, um das Signal von einem Mikrowellenapplikator zu empfangen, der in drei verschiedene Arten von Materialien eingeführt wird: Phantommaterialien, die die dielektrischen Eigenschaften der Leber nachahmen, Süßkartoffeln, die ähnliche dielektrische Eigenschaften wie die Leber haben, und Ex-vivo-Tierleber. Die Messergebnisse werden durch die Simulation und die Ergebnisse des theoretischen Modells bestätigt, das für die Übertragung von EM-Wellen von einer heißen Leber auf eine kalte Leber entwickelt wurde. Es wurde eine Korrelation zwischen dem Wachstum in der Ablationszone und der empfangenen Leistung an der Oberflächenantenne festgestellt. In dieser Arbeit wird das ISM-Band von 2,4-2,5 GHz für die Mikrowellenablation verwendet.

In dieser Arbeit werden verschiedene Phantommaterialien aus Polyvinylpyrrolidon und Triton X-100 hergestellt, um die dielektrischen Eigenschaften der Leber nachzuahmen. Darüber hinaus wird das Kapazitätsmodell verwendet, um die mathematische Formulierung zur Berechnung der dielektrischen Eigenschaften dieser Phantommaterialien aus der Messung des Reflexionsverlustes einer dielektrischen Sonde in den Phantommaterialien für verschiedene Frequenzen und Temperaturen abzuleiten. Darüber hinaus wird eine Hochleistungs-Mikrowellenquelle aus handelsüblichen Komponenten entwickelt, um hohe Leistungen bis zu 80 W in den zu prüfenden Materialien anzuregen. Die Oberflächenantennen sind für eine körperangepasste Anwendung, in diesem Fall die Leber, ausgelegt. Die Designs der linear polarisierten Bowtie-Slot-Oberflächen- und Tauchantennen werden vorgestellt. Für die Orientierungsunabhängigkeit in der Azimut-Ebene zur Platzierung der Antenne auf der Leberoberfläche wird eine zirkular polarisierte zirkulare Patch-Antenne mit und ohne Anpassungsmedium entworfen, was die Leistung der zirkularen Patch-Antenne verbessert. Zweitens wird der Entwurf eines Einschlitz-Mikrowellenapplikators vorgestellt, der zur Anregung hoher Leistungen in den in dieser Arbeit verwendeten Testmaterialien verwendet wird. Die Antennen werden mit der CST Studio Suite 2020.

entworfen.

In dieser Arbeit werden zwei Arten von Simulationen durchgeführt. In der ersten Simulation wird die Übertragung von EM-Wellen durch ein zweischichtiges Modell, bestehend aus einer heißen und einer kalten Leber, ähnlich dem theoretischen Modell, simuliert. Die zweite ist eine EM-thermische Co-Simulation, die durchgeführt wird, um verschiedene Temperaturprofile zu verschiedenen Zeitpunkten zu erhalten, während die Leber mit einer Leistung von 50 W bei 2,45

GHz stimuliert wird. Anhand dieser Temperaturprofile, die zu einer Veränderung der temperaturabhängigen dielektrischen Eigenschaften führen, werden dann die EM-Simulationen durchgeführt, um die Veränderung der an der Oberflächenantenne empfangenen Leistung zu ermitteln. Der zweite Simulationsansatz ist das Äquivalent zur Überwachung der Änderungen der empfangenen Leistung an einer Oberflächenantenne während der Mikrowellenablation in einer Ex-vivo-Leber. Entsprechend diesen Simulationen werden Experimente mit dem heißen und kalten Leberphantom, Süßkartoffeln und Tierlebern durchgeführt. In Experimenten mit zweischichtigen Phantomen wird eine Zunahme der empfangenen Leistung um 4,5 dB gemessen, wenn der Radius des heißen Lebergewebes bei einem Gesamtabstand von 4 cm zwischen dem Mikrowellenapplikator und der getauchten Antenne von 1 cm auf 2 cm erhöht wird. Andererseits gibt es einen gemessenen Verlust von 3 dB in der empfangenen Leistung nach 10 Minuten Mikrowellenablation in der Ex-vivo-Leber mit 50 W Mikrowellenleistung bei 2,45 GHz, wenn der Abstand zwischen dem Applikator und der Antenne wieder 4 cm beträgt. Die Änderung der empfangenen Leistung steht im Zusammenhang mit dem Wachstum der Ablationszone. Damit ist die transmissionsbasierte Methode zur Überwachung der Mikrowellenablation in der Leber validiert.



*"... And thy lord taught the bee to build its cells in hills, on trees, and in (men's) habitations; then to eat all of the produce (of the earth), and find with skills the spacious paths of its Lord."*

*The Noble Quran (16:68-69)*

*"The best of people are those that bring the most benefit to the rest of mankind."*

Prophet Muhammad (peace and blessings be upon him)



# 1

## Introduction

Radio- and Microwaves are in the non-ionizing part of the electromagnetic spectrum with numerous applications in health care and medicine. Microwaves are considered to be in the 300 MHz (1 m) to 300 GHz (1 mm) frequency range (see Figure: 1.1). The Industrial scientific and medical (ISM) band is assigned for medical applications in radio and microwaves; the frequencies in the ISM band used for medical applications are 9 kHz, 6.7 MHz, 13.5 MHz, 27.1 MHz, 40 MHz, 150 MHz, 434 MHz, 915 MHz, 2.45 GHz, 5.8 GHz, 24 GHz, 61 GHz, 122.5 GHz, and 245 GHz. [1].

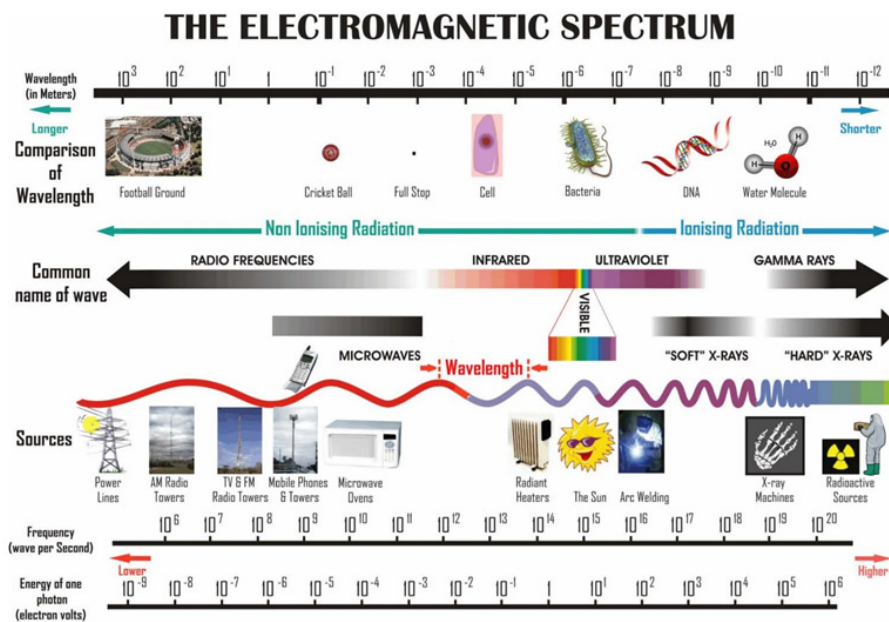


Figure 1.1: The electromagnetic spectrum: separating ionizing & non-ionizing part of the spectrum and indicating the slot for radio & microwaves. Photo courtesy: Australian Radiation Protection and Nuclear Safety Agency.

The microwaves are in a low-energy electromagnetic (EM) spectrum whose interaction with a living cell or biological molecule does not cause any chemical changes; therefore, microwaves can safely be used for any medical treatment or diagnostic purpose. However, high-power microwaves can cause thermal damage to an unwanted tissue such as a tumor [2]. These high power microwaves with thermal energy have medical applications in sterilization [3], heavy metal digestion [4], lysis [5], electroporation [6], and ablation therapy [7, 8]. Microwaves can also be used for diagnostic purposes where there is no thermal energy involved. Aided by surface antenna arrays, radar, and microwave tomography, a contrast in properties of healthy and malignant tissue can be diagnosed such as in breast cancer detection [9, 10, 11, 12, 13]. In addition to these applications, the new 5G technology enabled by wearable and implantable medical sensors has revolutionized the healthcare sector. Some applications of microwaves in e-healthcare such as non-contact security, behavior recognition, blood pressure, and pulse monitoring are discussed in [14].

## **1.1 Motivation**

---

Liver cancer is the fifth most common cause of cancer and the second most often cause of cancer-related death in men worldwide [15]. In Europe, 12.8 people out of 100,000 people are diagnosed with liver cancer out of which 11.3 people die, bringing the mortality to 88 % [16]. Therefore, there is a need for improvement in methods for diagnosis and treatment of liver cancer to bring down the very high mortality rate.

The focus of this work is on ablation therapy which is used for cancer treatment in the liver, lungs, kidneys, bones, and breasts [17, 18]. Microwave ablation therapy is widely used for the treatment of liver cancers; the reason is that the liver can regenerate itself and recover the tissues burnt during the ablation process as fast as the growth of the tumor itself [19]. Most microwave ablation systems are using 2.45 GHz ISM band for stimulating powers up to 140 W in 5-10 W steps for up to 600 s [20]. The temperature above 60 °C can reach in the first 30 seconds near the microwave applicator which is enough to denature the tumor tissues and hence permanently damage them.

Monitoring the growth of the ablation zone or temperature profile is crucial to control the ablation process; limiting the ablation process only to the tumor inside the liver and sparing the surrounding healthy tissues and organs. The small intestine and gallbladder are two organs under the liver which can also be damaged due to heating during the liver ablation if the tumor is seated near the lower border of the liver. Temperature monitoring using magnetic resonance (MR) thermometry is presented in [21] and the method is quite convenient as MR imaging (MRI) is also used for guiding the microwave applicator to the tumor in the liver. However, the flip side is that MR-based thermometry is susceptible to the movement of the patient and the results can be inaccurate. Additionally, MRI equipment is costly and bulky equipment whose availability cannot be made sure in every health facility. Therefore, a more portable, cost-effective, and non-invasive method for monitoring microwave ablation in the liver is required.

## **1.2 Aim of this Thesis**

---

The aim of this work is the development of a non-invasive method for monitoring microwave liver ablation. For this purpose, a microwave transmission-based method (TBM) is proposed to detect the changes in the magnitude of microwave power used for the ablation of liver tissue reaching the surface of the liver. The contrast in dielectric properties of heated and normal liver tissue accounts for the changes in the magnitude of microwave power reaching the surface of the liver sample being ablated. A microwave applicator and a high-power radio frequency (RF) source are developed for microwave ablation (MWA) in the liver. Furthermore, surface body-matched antennas (BMAs) are developed to detect these power changes. This is a unique method in which the power used for microwave ablation is also utilized for monitoring microwave ablation.

## **1.3 Structure of this Thesis**

---

In chapter 2, the clinical and technical background of MWA is presented. Firstly, there is a discussion about hyperthermia: ultrasound, RF, microwave, and laser ablation. MWA outshines the other ablation thera-

pies in different aspects. Secondly, the temperature dispersive dielectric properties of the liver are discussed briefly from the perspective of MWA monitoring. Thirdly, the previous works on MWA in the liver are presented along with their limitations for guiding this research.

In chapter 3, the concept design for this work is formulated. Firstly, all the non-invasive proposed methods for MWA monitoring are discussed. Secondly, three conceptual approaches are identified for non-invasive monitoring of MWA and the second approach (concept-2) is found to be more appropriate for MWA monitoring. Finally, an introduction of TBM and the reasons for choosing it are briefly discussed.

In chapter 4, theoretical modeling for MWA monitoring is presented. Firstly, the dielectric properties of tissue materials and their calculation from the reflection loss of the dielectric probe using the capacitance model are presented. Secondly, a two-layer model is presented for the propagation of EM waves through two liver phantoms mimicking the properties of a hot and a cold liver. Lastly, the thermal propagation in the liver is presented using the bio-heat equation.

In chapter 5, materials and methods are presented. Firstly, the making and working of the high-power RF source (HPS) are discussed which is used to excite high-power microwaves for MWA. Secondly, three materials under test (MUTs) are presented. Starting with animal liver and sweet potatoes (SP) as an alternative to the animal liver for ex-vivo studies. Then dielectric-equivalent phantoms of the liver, mimic the properties of the liver and the measurement of their properties is presented. Lastly, the experimental setups used for MWA in liver phantoms, sweet potatoes, and animal liver are presented and explained.

In chapter 6, all the simulations and measurements are presented. First of all, the design of a single-slot microwave applicator and its measurement in different MUTs is presented and its performance is compared with a commercially produced state-of-the-art microwave applicator. Next, the BMAs are presented and their need for MWA monitoring is explained. Two types of BMAs are presented: a bowtie-slot BMA which is linearly polarized and the other is a circularly polarized, circular patch antenna. The design, simulation, fabrication, and measurement of different variants of these BMA are presented here. Thirdly, for microwave transmission

through hot and cold liver phantoms, the simulation model and results, the experimental results, and the calculated results from the theoretical model are presented. Fourthly, MWA in sweet potatoes (SPs) as a substitute for the animal liver is presented. The reflected and received power, the temperature development during MWA in SPs, and the growth of the ablation zone are presented. The MWA in SPs is also compared with previous ex-vivo studies carried out on animal livers. Lastly, for monitoring of MWA in the ex-vivo liver, an EM-thermal simulation model of bowtie-slot surface BMA and microwave applicator inserted inside the liver is presented. The temperature profiles for all 10 minutes time instants with 50 W power are shown. The measured dielectric properties of animal liver during MWA are presented, then the measured ablation zone diameters are compared with the simulated one. Furthermore, simulated power received ( $|S_{21}|$ ) by surface body matched antenna and reflection loss ( $|S_{11}|$ ) of microwave applicator at 2.45 GHz is plotted against ablation time in comparison with the measured reflection and transmission loss. In the end, a relative change in received power in comparison to the initially received power and temperature growth in the ablation zone to ablation time are presented.

The last chapter is the discussion focused on the working of the microwave applicator and BMAs, transmission through liver phantoms, MWA monitoring in SPs and animal liver, and finally, the comparison of all calculated, simulated and measured results presented. In the end, there is the conclusion and an outlook upon the future work.





# 2

## Clinical and Technical Background

Hypocrites said, "Give me the power to produce fever and I will cure all disease". The efficacy of heat in treating wounds by burning is a time-tested method going on for centuries. Similarly, hot baths are also a universal practice for treating skin and other diseases since ancient times. For the last few decades, hyperthermia is an effective treatment for the treatment of cancer but also other diseases such as syphilis, gonorrhoea, arthritis, asthma and multiple sclerosis [22]. In this chapter, state-of-art in hyperthermia, characterization of dielectric properties of the liver, and experimentation with MWA in the ex-vivo liver are presented.

### **2.1 Hyperthermia: Ultrasound, RF, Microwave and laser Ablation**

---

Hyperthermia is a process of raising the temperature of the human body through an external source above 45 °C at which the tumor cells are denaturalized and damaged irreversibly. The malignant tumor cells have less blood perfusion rate than normal cells and therefore are more susceptible to heat in the 41-45 °C range. Hyperthermia is categorized into the whole body, regional and localized types: the whole body and regional hyperthermia are carried out by immersion in hot water, radiant heat, microwave and hot air cabinets, and perfusion of hot blood. The localized hyperthermia is carried out percutaneously with ultrasound (also trans-cutaneous), laser, RF and microwave energy focused on the target location [22, 23, 24].

Localized hyperthermia using ultrasound (US) is of two types: trans-cutaneous (non-invasive) and percutaneous. High intensity focused ultrasound (HIFU) is the only non-invasive method to produce hyperthermia;

however, the issue with this approach is that due to the sharp focusing of the US beam, the treatment of large tumors takes too long [23]. The other emerging method which is not yet used clinically is direct ultrasound ablation [25, 24], it is very precise and the directivity of the applicator can be used to protect critical areas and through beam-scanning ablation of larger volumes could be realized; however, more suitable applicators are still under-development for real clinical situations.

Radiofrequency ablation (RFA) is another method for producing localized hyperthermia percutaneously [23, 24]. The method is that RF electrodes are inserted into the target tumor location with the help of an RF electrode needle and high-frequency alternating currents are formed between them and grounding pads are placed externally on the patient's skin. Due to the alternating nature of RF currents, friction is produced near the electrode by already present ions in the tissues trying to catch up with changing the polarity of the electrodes. The effective area of electrodes is smaller in comparison to the external grounding pads; therefore, more heat is produced in the vicinity of RF electrodes thus causing thermal ablation of the target tissue. The amount of heat produced depends upon the RF energy delivered to the target tissue and heat dispersion is governed by the electrical conductivity and resistance of specific tissue. Usually, 150-200 W of RF power in the 450-500 kHz frequency range is excited for several minutes and a temperature above 100 °C is reached which is sufficient for causing irreversible damage to the tumor tissue. After a saturation point, due to the formation of gas bubbles and change in tissue resistance, the thermal damage of the tissue is stopped. With a single electrode a tumor size of up to 2.5 cm can be ablated but with some advanced electrodes up to 3-4 cm tumor can be ablated [25]. Another issue with RFA is that burns could be caused on the skin of the patient near the grounding pads which has led to increasing the number of grounding pads [25].

Thermal ablation due to EM radiation above 900 kHz is usually termed microwave ablation (MWA) [24]; however, practical systems operate at 915 MHz and 2.45 GHz. Microwave hyperthermia or MWA was introduced in the late 1970s for the treatment of cancerous tumors by using implantable microwave radiators [26, 27, 28]. The working principle is different than RFA, in MWA instead of the high-frequency alternating current, EM fields are directly applied to the target tissue. The principle is similar to dielec-

tric heating, when the electric field is applied to polar molecules like water, they try to realign with changing electric fields due to which kinetic energy is produced which produces friction and therefore heat. In MWA ablation, the electrical conductivity which enables the RF currents to flow does not hamper the EM fields; thus, MWA is not slowed down when the water content is diminished in the tissue. Also, MWA does not require any grounding pads for RF current flow rather the EM fields independently traverse through the target tissue. In conclusion, MWA is more efficient than RFA because it can ablate larger tissue volume in less time. In earlier MWA systems, microwave applicators had problems like heating along the shaft of the applicator which caused thermal damage along the insertion path of the applicator but in new designs, this problem has been solved by cooling through a water channel around the microwave applicator and using thicker power cables to absorb most of the heat in the return path [17, 23, 24, 25, 29, 30, 31, 32].

Laser ablation (LA) or laser-induced thermotherapy (LITT) is based on converting electrical energy to light energy which on absorption in the target tissue can instantly produce temperatures above 150 °C. LA is a less researched technique but is an effective technique because up to four fiber optic threads can be inserted from a gauge 21 device into the target location. However, the heat sink (presence of vessels) can hamper its effectiveness, the area where MWA still beats the other ablation methods [23, 24, 31, 32]. In conclusion, it could be said that MWA ablation is one method that is well-suited for thermal ablation in the liver for all conditions.

## **2.2 Dielectric Properties of Liver**

---

Interaction of EM waves with human beings and animals depends on the dielectric constant ( $\epsilon_r$ ) and electrical conductivity ( $\sigma$ ) of the specific tissue materials such as skin, and muscles, bones, blood, etc. The frequency dispersive material properties of various human tissues and organs up to 100 GHz are reported in [33]. The  $\epsilon_r$  and  $\sigma$  of liver tissue at body temperature at 2.45 GHz is 44.77 and 1.69 S/m respectively as reported in [33].

During microwave ablation of the liver, the temperature above 120 °C is reached in the ablation zone. Hence, for the interaction of EM waves with

the ablated liver tissue, there is a need to characterize the temperature dispersive properties of the liver. Temperature dispersive dielectric properties of animal liver during microwave ablation at 2.45 GHz are reported in [34, 35, 36]. In [36],  $\epsilon_r$  at 2.45 GHz ranges from 48 at 20 °C to 2 at 130 °C and  $\sigma$  at 2.45 GHz ranges from 2.15 S/m at 20 °C to 0.1 S/m at 130 °C. The contrast in material properties between heated liver and cold liver is a useful parameter for monitoring microwave ablation.

Animal livers such as bovine and porcine livers are used for liver ablation studies. However, there are also artificially synthesized phantoms that have dielectric properties similar to those of animal liver. Like in [37], a method for synthesizing polyvinylpyrrolidone (PVP) and salt-based tissue equivalent phantom materials is reported. Similarly in [38], Triton X-100 (TX-100) and salt-based phantom materials for 10 different biological tissues including the liver tissue are reported. Apart from artificially synthesized phantom materials, there also naturally occurring plant tissues that have similar properties to the liver. In [39], dielectric properties of sweet potatoes as reported in [40] are identified as similar to those of the liver. Hence, sweet potatoes and artificially synthesized phantom materials are suitable candidates for the study of the propagation of EM waves through liver tissue.

### **2.3 Microwave Ablation in Liver**

---

Clinically, thermal ablation is guided by imaging using ultrasound, computed tomography (CT), positron emission tomography (PET) or magnetic resonance imaging (MRI) [23]; however, it is also important to confine the ablation process only in the affected area but there is no adequate system to monitor ablation zone spread or temperature growth during the ablation procedure.

A significant amount of effort is being spent on the investigation of microwave ablation in the ex-vivo liver by studying the growth of the ablation zone with increasing microwave power and time [35, 41]. This is an indirect method of determining the extent of the ablation zone for different power and time schemes. Another approach is that of monitoring the change in reflection loss of the microwave applicator during the microwave ablation like in [35, 36] but this approach also is limited to change

in impedance matching of the microwave applicator just to the center of the ablation zone. In some works, temperature profiling of the ablation zone is done by measuring the temperature at different points in the ablation zone during the ablation by using localized temperature sensors [34, 42]. Firstly this is an invasive approach because the temperature sensors are inserted inside the liver to be deployed around the microwave applicator. Secondly, the temperature information is available only on a point or at best on a few points on a line as is the case with fiber-brag grating sensors [42].

Consequently, it can be deduced that the aforementioned methods are not sufficient for live monitoring of an ablation process and there is a need for non-invasive methods and techniques for monitoring the growth of the ablation zone and temperature.



# 3

## Concept Design

Microwave ablation is being practiced clinically since the early 2000s and since 2008 at University Hospital Frankfurt to treat patients with lung and liver tumors. As discussed earlier, MWA is a minimally invasive treatment that can ablate comparatively large tumors in a smaller amount of time without surgery. The microwave applicator is guided to the center of the tumor with the help of an MRI. However, MRI does not provide information about the growth of the ablation zone or temperature. In the following section, some of the proposed methods for non-invasive monitoring of the growth of the ablation zone or temperature during ablation are presented.

### **3.1 Proposed non-invasive Methods for Microwave Ablation Monitoring**

---

In [21], the magnetic resonance mediated radiofrequency ablation (MR-RFA) method is proposed. RFA is carried out using the RF field of the MR scanner itself, so no external RF generator is required. MR thermometry is carried out using the Proton resonance frequency (PRF) shift method and is validated by fiber-optic temperature sensors attached to the ablation needle inserted in the liver. Experiments are performed on agar phantoms, ex-vivo liver, and live animals. The work provides a one-window solution for thermal ablation, guidance, and monitoring of RFA. However, it inherits some of the problems of RFA itself used for liver ablation and the heat deposition in in-vivo experiments is not the same as in the case of ex-vivo experiments which limits its applicability. The temperature change imaged by the PRF method is 20 °C compared to the recorded value of 22 °C by fiber-optic temperature sensors. In conclusion, this method although

seemingly promising is recently proposed and is yet to mature further with clinical trials. The limitation of the work is obvious that the whole intervention has to be carried out in a specially equipped MR scanner. Therefore, there is still a need for a cost-effective and more portable microwave ablation monitoring system. Additionally, MR imaging is prone to patient geometry and the results could be affected due to the movement of the patient during the procedure.

Microwave imaging (MWI) is another promising non-invasive solution for monitoring the growth of the ablation zone during ablation. Microwave imaging or tomography depends upon the solution of inverse source and inverse scattering problems. In other words, based on the received microwave signals, the shape of the scatterer or the source is predicted. In the last few decades, a lot of effort has been spent on developing efficient algorithms through machine learning and compressive sensing to accurately reconstruct many real-life problems. Microwave imaging is proposed for the diagnosis of breast, brain, and lung cancers, brain stroke detection, and now for monitoring of microwave ablation of the liver also. In [43], a UWB array of antennas submerged into a matching medium surrounding phantoms mimicking liver ablation setup. The changes in the scattered signals (S-parameters) from the liver phantoms received by the surrounding antennas over a UWB frequency are used to reconstruct the ablation zone using the singular value decomposition (SVD) microwave imaging algorithm. This is a work in progress towards an actual microwave imaging-based thermal ablation monitoring system. Microwave imaging-based thermal ablation monitoring through S-parameters of the scattered signals over UWB frequency is also proposed in [44].

Another algorithmic method applied for microwave ablation monitoring is based on the time difference of arrival (TDoA) of microwave signals emitted from the center of the ablation zone by the microwave applicator received by the antennas surrounding the tissue under test as reported in [45, 46]. In these simulation studies, the time difference is calculated by first observing the time of arrival of the transmitted signal before ablation and then the time of arrival at different instances of microwave ablation. In the mathematical model, the radius of the ablation zone in a specific direction is related to TDoA, propagation velocity in pre-ablated tissue, and the fractional change in permittivity of ablated and pre-ablated tissue at



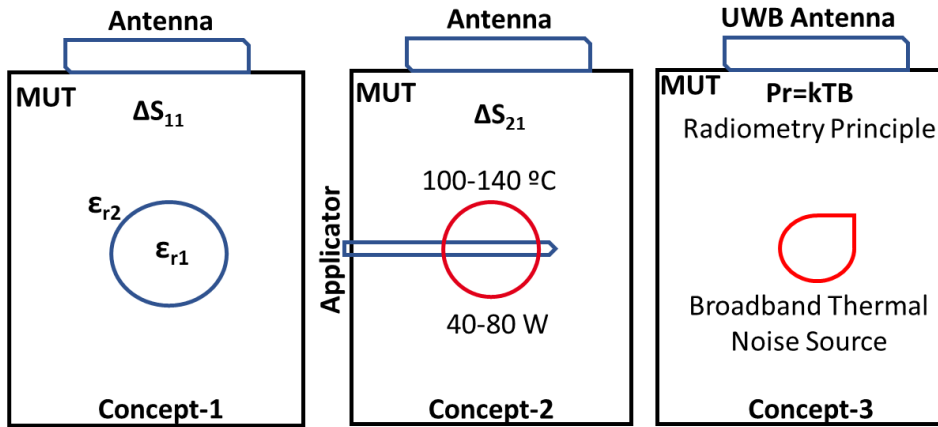


Figure 3.1: Conceptual design approaches for non-invasive monitoring of thermal ablation inside a material under test (MUT). Concept-1: Monitoring changes in the reflection loss ( $\Delta S_{11}$ ) of surface BMA due to dispersion dielectric properties. Concept-2: Monitoring changes in the transmission coefficient ( $\Delta S_{21}$ ) on surface BMA during microwave ablation. Concept-3: Measuring changes in received power due to the brightness temperature of a broadband thermal noise source.

the specific time instant. The remarkable aspect of these works is that it is claimed that the position of the receiving antenna does not have a major effect on the reconstruction of the ablation zone.

Microwave radiometry is another approach that can also be applied for microwave imaging. Detecting depth and changes in temperature inside the human brain using microwave radiometry is proposed in [47, 48, 49]. Similarly, in [50], a multi-frequency microwave thermograph is presented for estimating the temperature, depth, and size of a heat source in the human breast. The radiometry principle relies upon the  $P = kTB$  equation which related the power radiated by a heated source to the temperature and radiation bandwidth of the heat source; where K is the Boltzmann constant. The same radiometry principle could also be used for the detection of temperature changes inside the liver during thermal ablation.

### 3.2 Concept design approach

The problem of non-invasive monitoring of thermal ablation in tissue is approached with three types of concept studies as shown in figure 3.1.

Concept-1 is based on monitoring of changes in reflection loss of a surface BMA placed over a material under test (MUT) which changes dielectric properties inside it. This change in dielectric properties could be a result of a tumor that has usually different properties than the host tissue or it could also be a result of thermal ablation which heats the tissue resulting in a change in the dielectric properties. Some initial experimental studies are carried out with a surface UWB antenna placed on a liver phantom which is heated with a heating cartridge 7.5 cm below the antenna. There is a change of about 4 dB in reflection loss as the liver phantom is heated from 30 °C to 80 °C at the resonant frequency (1 GHz) of the antenna. However, in the rest of the band, there is no significant change in the reflection loss. Moreover, the magnitude of the reflection loss at the resonant frequency and the change are variable in different experiments.

Concept-2 is based on monitoring of changes in transmission coefficient ( $\Delta S_{21}$ ) for a microwave power transmitted by a microwave applicator inside a MUT and which is received by a surface BMA. It is similar to concept-1 in the way that the MUT undergoes a change in dielectric properties at the ablation zone but it differs in the way that there are two antennas involved whose individual reflection losses ( $S_{11}$ ,  $S_{22}$ ) and also the transmission coefficient ( $S_{21}$ ) between the two antennas change. However, the change in the reflection loss of the surface BMA ( $S_{22}$ ) is not changed much as compared to the reflection loss of the microwave applicator ( $S_{11}$ ) which causes the change in dielectric properties in the MUT and lies at the center of this change. In an initial simulation study reported in [51], a BMA is placed on the liver and a microwave applicator is inserted 7.5 cm below the BMA. After 300 s of MWA with 50 W power, there is a change of about 10 dB in the transmission at 915 MHz ISM band, 6 dB at 2.45 GHz ISM band, and about 3 dB change at 5.8 GHz ISM band.

Concept-3 is based on the radiometric principle which states that everything in the surroundings emits electromagnetic energy and the power emitted by that body is proportional to the brightness temperature ( $T$ ) and the bandwidth ( $B$ ) in which that power is measured. Therefore, an Ultra-wideband (UWB) BMA is required to receive the microwave power emitted by a thermal noise source over a large bandwidth. Then the changes in the power received by the microwave radiometer can be correlated to the rise

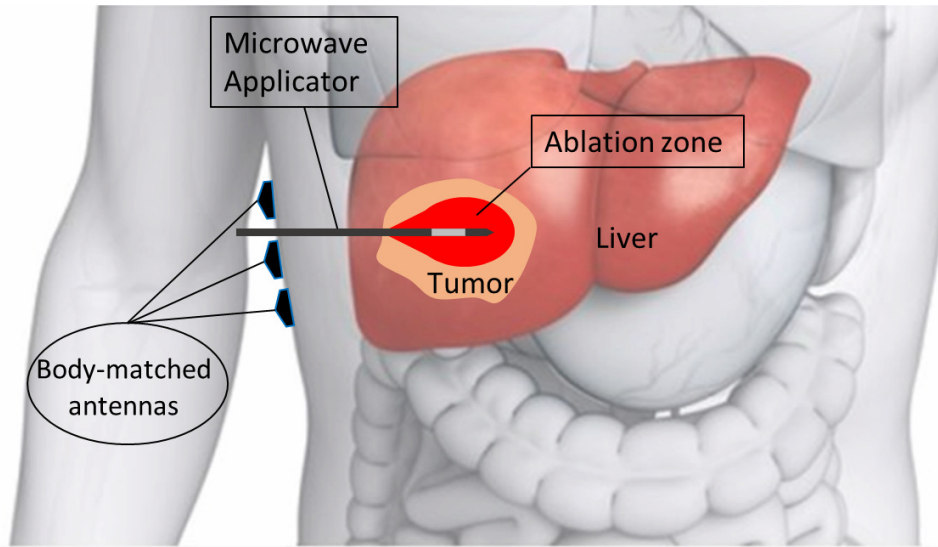


Figure 3.2: Conceptual design of the proposed transmission-based method for MWA monitoring. Body-matched antennas are placed on the patient's skin to measure the microwave power from the applicator inserted in the liver.

in brightness temperature of the target tissue during the ablation process. However, no further investigation of concept-3 is done.

The concept-2 is more suited for the monitoring of MWA because it takes advantage of the active microwave source at the center of the ablation zone which continuously emits power during the ablation. It is noteworthy that the change in the transmission at the ablation frequencies is regardless of the resonant frequency of the surface antenna. Moreover, the reflection loss in concept-1 relies on the reflections from the ablation zone which have to travel double the distance than in the case of direct transmission from the ablation zone to the surface antenna. Therefore a transmission-based method is developed for non-invasive monitoring of MWA in the liver.

### 3.3 Transmission based method

---

In this work, a transmission-based method is proposed for MWA monitoring in the liver as shown in figure 3.2. Combining various aspects of the aforementioned microwave imaging approaches, a microwave applicator is inserted in the liver as an EM source and a surface body-matched an-

tenna is placed on the liver surface to receive and detect power magnitude changes during microwave ablation. The received power is noted at the beginning of the ablation process and then the change in received power is observed during the ablation process which is related to the growth of the ablation zone.

The reason for choosing TBM is that: exciting more than 50 W power in a microwave applicator at 2.45 GHz provides a significant contrast in the receive power magnitude at the surface antenna during the microwave ablation. The transmission-based method can be used for microwave imaging technique more like in [45, 46] where there is an active microwave source (applicator) doing the thermal ablation at 2.45 GHz and also like in [43] where there is surface body matched antennas to detect the changes in the magnitude of microwave power on the surface. The transmission-based method is validated theoretically, in simulation, and measurements. The simulation and experimental setup carried out to validate the transmission-based method are closer to the real situation than the aforementioned proposed microwave ablation monitoring methods.

# 4

## Theoretical and Mathematical Modeling

It is important to theoretically and mathematically validate the transmission-based method for microwave ablation monitoring. Firstly, an introduction to the dielectric properties of tissue materials is given and then the reflection-based method to calculate the permittivity and conductivity of substances is presented which is used later to measure the properties of synthesized phantoms mimicking the properties of the hot and cold liver. Secondly, propagation of EM waves in the liver is studied in a two-layer model representing hot and cold liver for microwave ablation liver using a microwave applicator and the power received by surface body-matched antennas. In the end, the propagation of heat in biological tissues is studied for understanding the extent of the ablation zone created for a given microwave power stimulated in the liver for a certain time.

### 4.1 Permittivity and conductivity of tissue materials

The dielectric material has an arrangement of electric charges which on the application of an external electric field try to align themselves with the polarity of the field. The friction produced by this alignment contributes to the dielectric loss of the material. When the field has been removed the charges in the material tend back to their original state which is represented by the relaxation time ( $\tau$ ). A dielectric constant ( $\epsilon$ ) of a material represents the polarization ability of that material. Mathematically,  $\epsilon$  of a material is a multiple of the permittivity of free space ( $\epsilon_0$ ) and the relative permittivity ( $\epsilon_r$ ) of the material to free space as represented in equation (4.1):

$$\epsilon = \epsilon_0 \epsilon_r \quad (4.1)$$


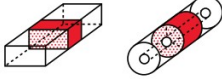
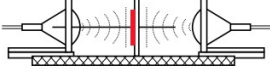
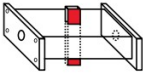
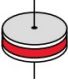

Coaxial probe $\epsilon_r$		Broadband convenient, non-destructive. Best for lossy MUTs; liquids and semi solids
Transmission line $\epsilon_r$ and $\mu_r$		Broadband Best for lossy to low loss MUTs; machineable solid
Free space $\epsilon_r$ and $\mu_r$		Broadband; non-contacting Best for flat sheets, powders, high temperatures
Resonant cavity $\epsilon_r$		Single frequency; accurate Best for low loss MUTs; small samples
Parallel plate $\epsilon_r$		Accurate Best for low frequencies; thin, flat sheets
Inductance measurement $\mu_r$		Accurate, simple measurement, a toroidal core structure is required

Figure 4.1: Dielectric properties measurement techniques [52].

The relative permittivity of a material is a complex quantity represented by equation (4.2). The real part  $\epsilon_r'$  is the dielectric constant of the material representing the polarization ability of the material and hence energy storage capacity. The imaginary part  $\epsilon_r''$  is called the dielectric loss number which characterizes the ability of a material to convert microwave energy into heat energy.  $\epsilon_r''$  depends upon the electrical conductivity ( $\sigma$ ) and the angular frequency ( $\omega$ ) of the material as represented in equation (4.3).

$$\epsilon_r^* = \epsilon_r' - j\epsilon_r'' \quad (4.2)$$

$$\epsilon_r'' = \frac{\sigma}{\omega \cdot \epsilon_0} \quad (4.3)$$

A coaxial probe model is used for the calculation of dielectric properties of a tissue material or phantom mimicking properties of tissue. The coaxial probe method is better suited for the dielectric properties measurement of liquids and semi-solid. Different methods used for calculation of dielectric properties of materials are shown in figure 4.1.

Firstly, the reflection loss ( $S_{11}$ ) of the material under test is measured with a dielectric probe containing a real and an imaginary component as represented in equation (4.4).

$$S_{11}^* = S'_{11} + jS''_{11} = Re + jIm \quad (4.4)$$

Then, angular frequency ( $\omega$ ), wave impedance ( $Z_o$ ) and geometry factor ( $K$ ) of the dielectric probe are required to calculate  $\epsilon'_r$  and  $\epsilon''_r$  of the material under test as represented in equation (4.5) and equation (4.6) respectively. The geometry factor ( $K$ ) of the probe can be found by using it in materials with known dielectric properties.

$$\epsilon'_r = \frac{1 - Re^2 - Im^2}{KZ_o\omega((1 + Re)^2 - Im^2)} \quad (4.5)$$

$$\epsilon''_r = \frac{-2Im}{KZ_o\omega((1 + Re)^2 - Im^2)} \quad (4.6)$$

## 4.2 Propagation of electromagnetic waves in liver

A transmission-based model for two tissue layers representing cold tissue ( $\alpha_1, \epsilon_{r1}, \sigma_1$ ) and hot tissue ( $\alpha_2, \epsilon_{r2}, \sigma_2$ ) is developed as illustrated in figure 4.2. The relative permittivity of a tissue  $\epsilon'_r$  and  $\epsilon''_r$  define its constitutive parameters: the magnitude of the relative permittivity ( $|\epsilon_r|$ ), electrical conductivity ( $\sigma$ ), characteristic impedance ( $Z$ ) and propagation constant ( $\alpha$ ) as described in equations (4.7), (4.8), (4.9) and (4.10):

$$|\epsilon_r| = \sqrt{\epsilon_r'^2 + \epsilon_r''^2} \quad (4.7)$$

$$\sigma = \epsilon_r'' \cdot \omega \cdot \epsilon_0 \quad (4.8)$$

$$Z = \frac{\mu_0 \cdot \mu_r}{\epsilon_r \cdot \epsilon_0} \quad (4.9)$$

$$\alpha = \frac{\omega}{c_0} \cdot \sqrt{\frac{\mu_r \epsilon_r'}{2} \sqrt{1 + \left(\frac{\sigma}{\omega \epsilon_0 \epsilon_r'}\right)^2} - 1} \quad (4.10)$$

Where  $\epsilon_o$  is the permittivity of free space  $8.85 \times 10^{-12}$  F/m,  $\mu_o$  is the permeability of free space  $4\pi \times 10^{-7}$  H/m, and  $c_o$  is the velocity of light in free space  $3 \times 10^8$  m/s.

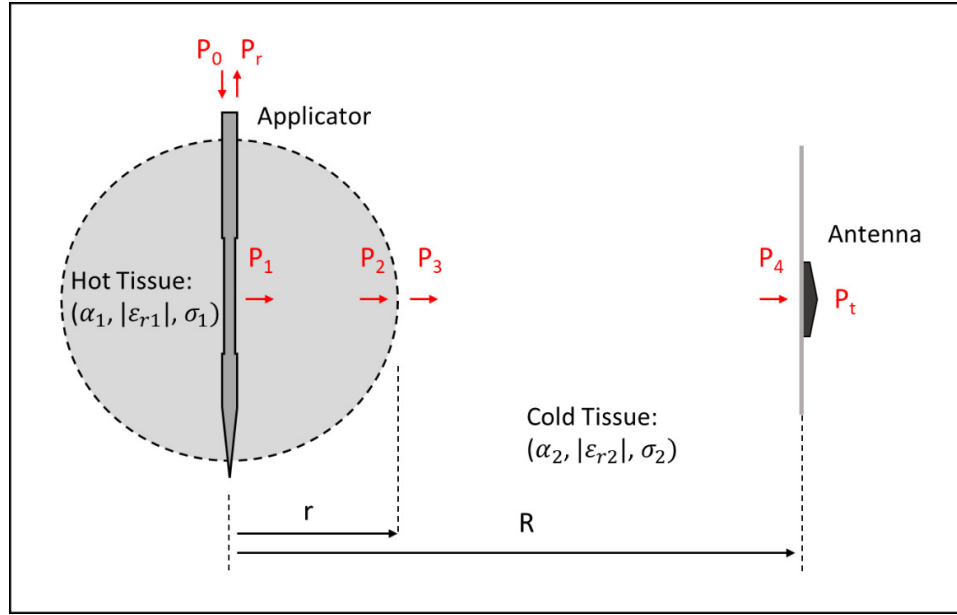


Figure 4.2: Illustration of the transmission-based theoretical model for microwave power traversing through two-layer model representing hot and cold liver tissues.

To begin with,  $P_0$  is the power stimulated into the applicator by an external HPS out of which  $P_r$  is reflected. The coupling factor ( $K_1$ ) determines the incident power radiated into the hot tissue ( $P_1$ ) as described in equations (4.11), (4.12) and (4.13):

$$P_r = P_0 \cdot 10^{\frac{|S_{11}|[dB]}{10}} \quad (4.11)$$

$$K_1 = 1 - 10^{\frac{|S_{11}|[dB]}{10}} \quad (4.12)$$

$$P_1 = K_1 \cdot P_0 \quad (4.13)$$

Here forth, the path loss in the hot tissue is determined by the propagation constant  $\alpha_1$  of the hot tissue and distance  $r$ ; hence, the power reached the boundary of hot and cold tissue ( $P_2$ ) is given by equation (4.14). At the boundary of hot and cold tissue, the power transmitted across the boundary into the cold tissue ( $P_3$ ) is determined by the transmission coefficient ( $T$ ) between the two mediums as illustrated in equations (4.15) and (4.16):

$$P_2 = P_1 \cdot e^{-2\alpha_1 \cdot r} \quad (4.14)$$



$$T = \frac{2Z_2}{Z_1 + Z_2} \quad (4.15)$$

$$P_3 = |T|^2 \cdot P_2 \quad (4.16)$$

Again the EM wave traverses across the cold tissue with a propagation constant  $\alpha_2$  for a distance of  $(R - r)$  and the power reached the boundary of the cold tissue with the BMA ( $P_4$ ) is given by equation (4.17). From there on, the power coupled into the antenna  $P_t$  is determined by the coupling factor  $K_2$  and geometry factor  $G$  of the antenna (with an effective area ' $A_{eff}$ ') which is calculated with an assumption that the wavefront is spherical from the microwave applicator till the BMA for a total distance of  $R$ , as given by equation (4.20). So finally, the complete theoretical model is given by equations (4.21) and (4.22) showing the relation between power stimulated ( $P_0$ ) and power received by the antenna ( $P_t$ ).

$$P_4 = P_3 \cdot e^{-2\alpha_2(R-r)} \quad (4.17)$$

$$K_2 = 1 - 10^{\frac{|S_{22}|[dB]}{10}} \quad (4.18)$$

$$G = \frac{A_{eff}}{4\pi R^2} \quad (4.19)$$

$$P_t = G \cdot K_2 \cdot P_4 \quad (4.20)$$

$$P_t = G \cdot K_1 \cdot K_2 \cdot |T|^2 \cdot e^{-2\alpha_1 r} \cdot e^{-2\alpha_2(R-r)} \cdot P_0 \quad (4.21)$$

$$\frac{P_t}{P_0} = G \cdot K_1 \cdot K_2 \cdot |T|^2 \cdot e^{-2\alpha_2 R} \cdot e^{-2(\alpha_1 - \alpha_2)r} \quad (4.22)$$

Here, a constant 'D' is defined as:  $G \cdot K_1 \cdot K_2 \cdot |T|^2 \cdot e^{-2\alpha_2 R}$ . The transmitted power in terms of S-parameters is given by equation (4.23).

$$|S_{21}| = 10 \cdot \log\left(\frac{P_t}{P_0}\right) = D \cdot 10 \cdot \log(e^{-2(\alpha_1 - \alpha_2)r}) \quad (4.23)$$

### 4.3 Thermal propagation in biological tissues

As in microwave ablation, continuously changing electric fields of the EM waves are applied to the tissue to be ablated. The polar molecules in the tissue such as water try to realign themselves with the changing electric field which produces constant friction in the tissue which generates heat.

Heat ( $Q_E$ ) generated by changing electric fields (E) is given by equation (4.24).

$$Q_E = \frac{1}{2} \omega \epsilon_o \epsilon_r |E^2| \quad (4.24)$$

Propagation of heat in biological tissues depends on the inhomogeneity of the tissues, different geometries of the organs due to many vascular paths of small and big vessels, the strong temperature dependence of the involved tissue materials, and heat produced by metabolic processes and thermal regulation due to blood perfusion. All of these factors have been catered for in the famous bio-heat equation (4.25) first introduced in [53].

$$\rho c \frac{\delta T}{\delta t} = \nabla \cdot k \nabla T + Q_P + Q_E + Q_M \quad (4.25)$$

Where; ' $\rho$ ' is the density ( $kg.m^{-3}$ ), ' $c$ ' is the heat capacity ( $J.kg^{-1}.K^{-1}$ ), ' $T$ ' is temperature (K),  $t$  is time (s), ' $k$ ' is thermal conductivity ( $W.K^{-1}.m^{-1}$ ). The left-hand side of the bio-heat equation gives the rate of temperature rise in a volume of material with certain specific heat and density. On the other hand, the first term of the right-hand side gives the heat distribution in the considered volume with thermal conductivity ( $k$ ). The other factors contributing to heat distribution are  $Q_E$ , ' $Q_P$ ' flow of heat due to blood perfusion, and ' $Q_M$ ' the heat produced by metabolic processes.  $Q_M$  is negligible as compared to other factors.  $Q_P$  heat distribution due to blood perfusion is a process of heat convection produced by the flow of blood in large (macrovascular) and small (microvascular) vessels.  $Q_P$  is mathematically described in equation (4.26).

$$Q_P = \rho_b c_b \omega_b (T_b - T) \quad (4.26)$$

Where;  $\rho_b$ ,  $c_b$  and  $\omega_b$  are density, specific heat capacity and perfusion coefficient of the blood respectively.  $T_b$  is the temperature of the blood and  $T$  is the temperature of the measurement point.  $Q_P$  could result in either flow of heat away from the ablation zone if the temperature of the ablation zone is higher than that of blood or vice-versa.

# 5

## Materials and Methods

The transmission-based method for monitoring microwave liver ablation is experimentally validated by a test setup consisting of various materials and methods. An introductory setup diagram is shown in figure 5.1 to explain the working of the transmission-based method for microwave liver ablation monitoring. The test setup consists of a high-power RF source (HPS), microwave applicator, body-matched antenna (BMA), temperature sensors, dielectric measurement probes, and materials under test (MUTs) such as tissue phantoms mimicking properties of liver, animal liver, and sweet potatoes, voltage network analyzer (VNA) and spectrum analyzer. The whole intervention is carried out inside an anechoic chamber for safety reasons. The microwave power is excited by the HPS into the microwave applicator which is inserted inside a MUT. On the surface of the MUT is a BMA that receives the microwave power which is read by a spectrum analyzer. For measurement of temperature and dielectric properties during the ablation process, a temperature sensor and dielectric probe are inserted in the MUT around the center of the ablation zone.

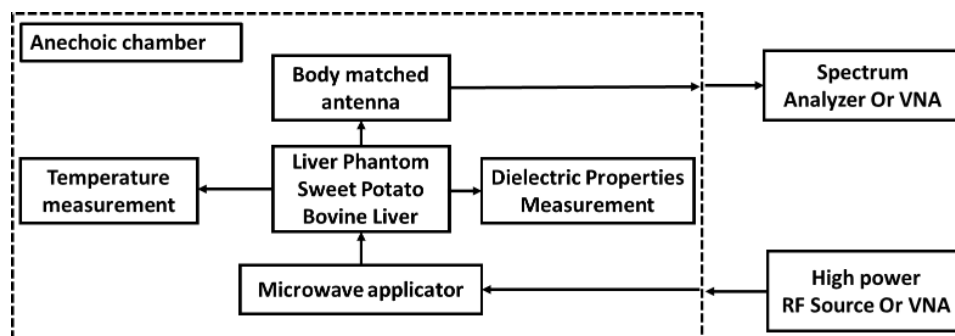


Figure 5.1: MWA monitoring experiment flowchart for transmission-based method.

In this chapter, firstly the assembly and working of the HPS are presented. Secondly, all the MUTs and their temperature-dependent dielectric properties are presented, starting with the animal liver which is used as a reference for other MUTs. Subsequently, sweet potatoes (SP) are introduced as a substitute material for liver used for ex-vivo MWA experiments. Finally, the synthesis of the tissue phantom materials mimicking the dielectric properties of the liver and measured results of these phantom materials are presented. Towards the end of this chapter, all the experimental setups used for microwave transmission through the two-layer tissue phantom models, the setup for MWA experiments with SPs, and finally the experimental setup for MWA in the ex-vivo liver are presented.

## 5.1 High power RF Source

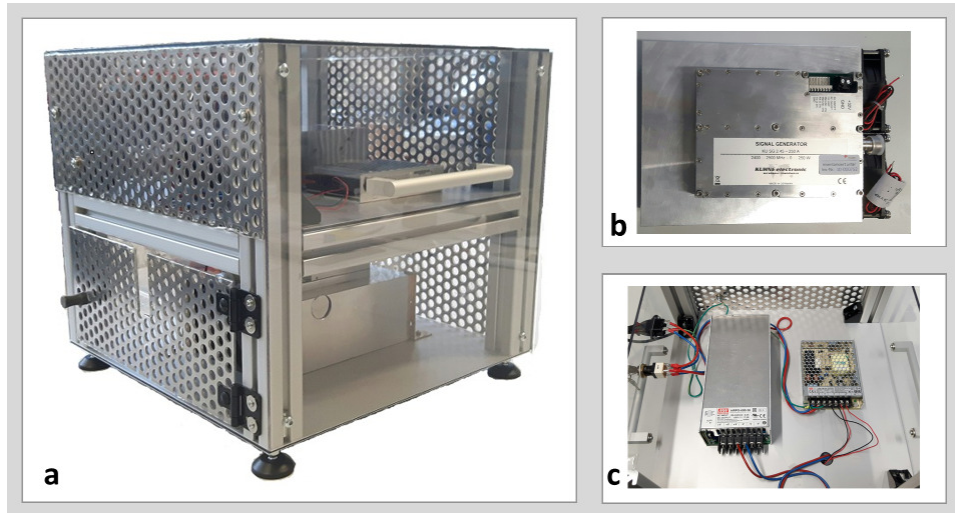


Figure 5.2: High-power RF source by Kuhne Electronics: (a) Housing (b) Signal generator (c) Power supply.

An HPS is used to excite up to 80 W microwave power required for microwave ablation of the liver at 2.45 GHz. The HPS is built from off-the-shelf components (signal generator and power supply) from Kuhne Electronics, in a parallel work [54]. The signal generator is mounted on a heat sink and has additional fans for cooling which are required as it can reach up to an RF power level of 250 W. The power and frequency settings of the signal generator are done through an external graphical user interface

(GUI). The initial power is 10 W and it can be increased further in steps of 10 W. The frequency range is 2.4-2.5 GHz and can be adjusted with a step of 0.05 GHz. The signal generator is run with a power supply of 32 V, with a maximum current of 17.5 A. Furthermore, there is an additional power supply of 24 V needed for the cooling fans. Furthermore, an LED is located on the side of the signal generator to signal the various operating states. The LED lights up green during normal operation. When this goes off, the voltage drops to a level of 30 V thereby terminating the signal generator. The red light indicates a temperature alarm of 85 °C, and the signal generator is automatically switched off and switches on again at an acceptable temperature (60 °C). For additional protection, the RF ON/OFF input, which switches the signal generator on and off, is connected to an external key switch. The housing of the HPS, signal generator, and power supply units are shown in figure 5.2.

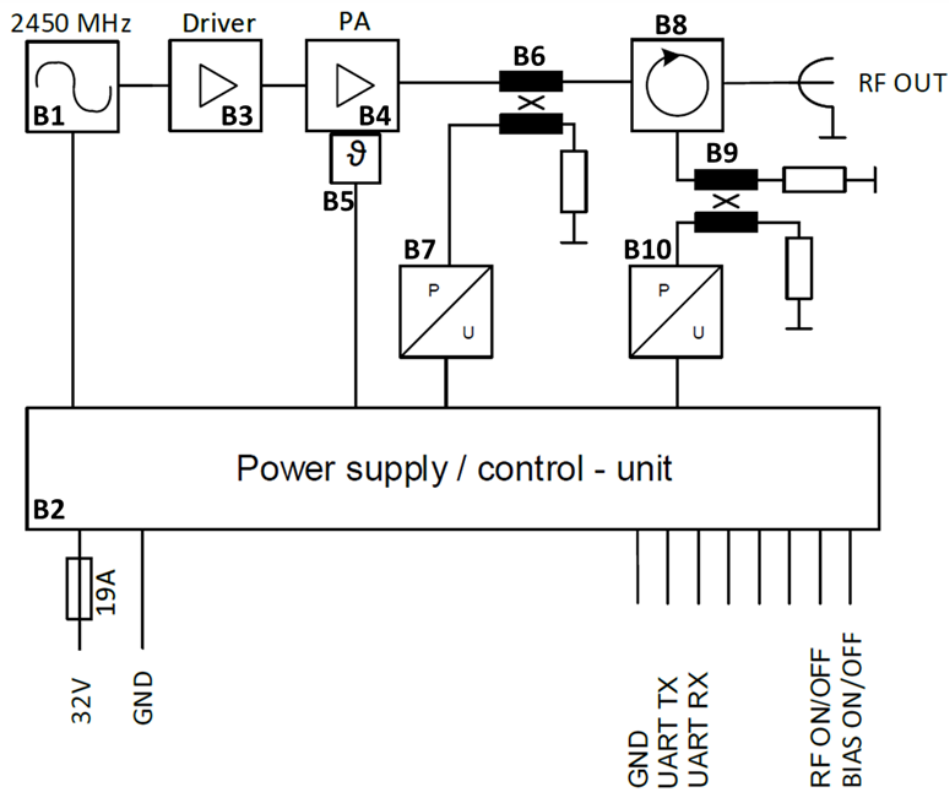


Figure 5.3: High-power RF source by Kuhne Electronics: circuit diagram of the signal generator [55].

The block diagram explaining the working of the signal generator is shown in figure 5.3. The explanation is as follows: the oscillator (B1) generates a 2.45 GHz signal and is connected to a power control unit (PCU). The PCU (B2) controls and regulates the entire signal generator. The signal is first processed by a low-power driver amplifier (B3) and then it is amplified to a given high RF power by a power amplifier (PA/B4). In B5, temperature measurements are performed by several temperature sensors and if the temperature is too high, the PCU switches the system to a safe mode. Furthermore in B5, the power is also monitored via the PCU, and part of the power is then decoupled via a directional coupler (B6) and converted to voltage in B7. The forward and backward shafts are controlled by a circulator (B8) which relays the forward signal to the RF OUT port and guides the reflected signal to an internal load. For measuring the reflected signal, a part of the reflected signal is decoupled via a second directional coupler (B9) and converted to a voltage by power/voltage converter (B10) so that the PCU can evaluate the signal. The GUI communicates with the PCU via a UART interface.

## 5.2 Materials under Test

Animal liver, sweet potatoes, and tissue phantom mimicking material properties of the liver are used as MUTs for microwave ablation monitoring experiments. The frequency dispersive dielectric properties of all human tissues are detailed by Camelia Gabriel in her seminal work [33]. The dielectric properties of the human liver at 2.45 GHz are given in this work as relative permittivity ( $|\epsilon_r|$ ) of 44.77 and electrical conductivity ( $\sigma$ ) of 1.69 S/m.

### 5.2.1 Animal Liver

The bovine liver is used for ex-vivo MWA experiments on the liver. The temperature dispersive dielectric properties of the bovine liver are characterized in the previous works [35, 36] and are suitable to be used for MWA monitoring experiments. The measured dielectric properties ( $\epsilon_r, \sigma$ ) in [36] of the animal liver is shown in figure 5.4. According to the sigmoidal fit [12] which covers the upper and the lower bounds of the measured values of  $|\epsilon_r|$  and  $\sigma$ , the  $|\epsilon_r|$  at 2.45 GHz ranges from 48 at 20 °C to 2 at 130 °C and

$\sigma$  at 2.45 GHz ranges from 2.15 S/m at 20 °C to 0.1 S/m at 130 °C. Hence, these values serve as a reference for MUTs to be used for MWA monitoring experiments for the liver.

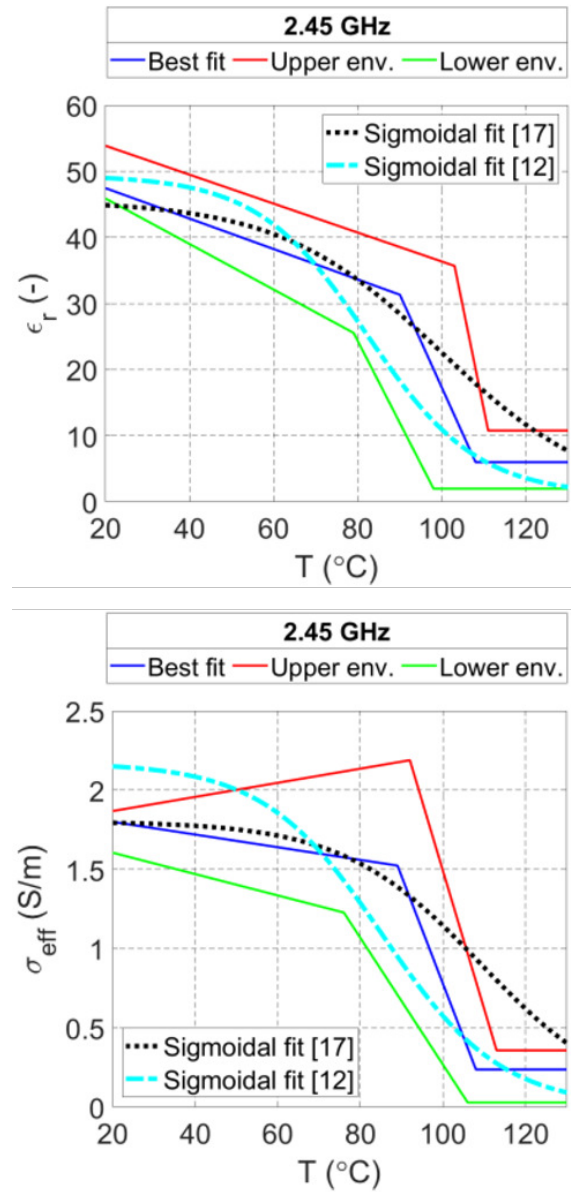


Figure 5.4: Measured relative dielectric constant ( $\epsilon_r$ ) and electrical conductivity ( $\sigma$ ) of animal liver with respect to temperature at 2.45 GHz [36].

In a parallel work [56], the bovine liver is characterized by weight loss (change in density) with time and permittivity and conductivity to in-

creasing temperature and the results are comparable with previous works. Two kinds of the liver are used in the experiment: one is procured from a butcher shop which is 24-48 hours old; however, it is preserved at freezing temperature. This liver is assigned a freshness grade '1'. The other liver is picked up directly from the slaughterhouse and brought to the laboratory in an ice box packed inside an airtight plastic bag. The experiments are performed on it within the first 8 hours after the slaughter. A freshness grade '2' is assigned to the liver picked up from the slaughterhouse. The weight loss of both types of livers is monitored over time and it is found that with grade-2 liver samples the weight loss per hour is 1.8 % while the grade-1 liver samples lose weight at 1.5 % per hour. Therefore, a gradual change in liver properties is expected from the time of slaughter.

### 5.2.2 Sweet Potatoes

Ex-vivo investigations on animal livers are carried out to measure localized temperature, temperature dispersive material properties, and the spread of the ablation zone with ablation time and power in order to comprehend MWA in the liver. However, the ex-vivo liver's physical characteristics are extremely unstable because, as time passes after slaughter, the animal's liver rapidly loses water and, as a result, the electrical conductivity of the ex-vivo liver changes. To overcome this challenge, a substitute material whose dielectric properties are less sensitive to time is needed. Sweet potatoes have been found to be an effective alternative material for ex-vivo MWA experiments on the liver because of their similar physical properties as those of liver, as demonstrated in [40]. Table 5.1 provides a comparison of the dielectric constant, electrical conductivity, water content, and density of sweet potatoes and animal liver at room temperature at 2.45 GHz.

Sweet potatoes are preferable to the animal liver for ex-vivo MWA investigations also due to other factors. Firstly, sweet potatoes are easier to handle than animal liver, as there is no involvement of blood during the experiments which is sometimes difficult to handle and obstructs the smooth performance of the experiment. Furthermore, sweet potatoes are less logistically challenging to store for long periods of time whereas it is difficult to store the animal liver even in a temperature controlled environment.



Table 5.1: Comparison of the physical properties at room temperature of the ex-vivo animal liver and sweet potato at 2.45 GHz [39].

Physical Property	Animal Liver	Sweet potato
Electrical Conductivity ( $\sigma$ )	1.7 S/m [33]	1.9 S/m [40]
Dielectric Constant ( $\epsilon_r$ )	43 [33]	52 [40]
Density	0.95 g/cm <sup>3</sup> [57]	1.07 g/cm <sup>3</sup> [40]
Water content	80.5 % [58]	75 % [40]

Moreover, the physical properties of sweet potatoes are more stable over time, whereas the properties of animal liver can drastically change due to the loss of moisture content, which can be 70-80 % of the total liver volume as reported in [58]. Lastly, during an ex-vivo experiment on the animal liver, the properties of the outer part of the liver may not be representative of the in-vivo environment, as the inner part of the liver is being ablated. Whereas, in sweet potatoes, the outer properties remain consistent during an ex-vivo experiment.

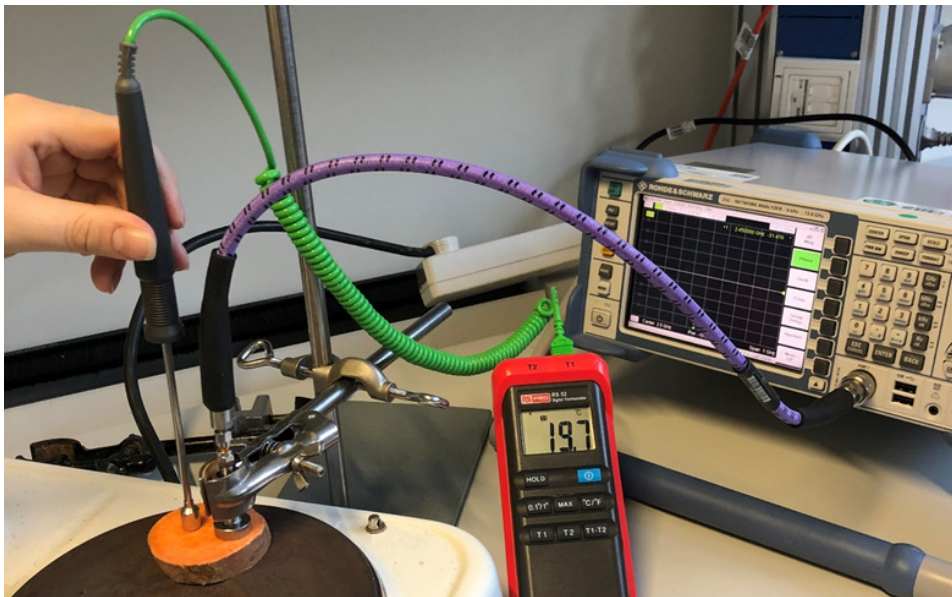


Figure 5.5: Experimental setup for measuring temperature dispersive dielectric properties of a SP placed on a heating plate with a high-temperature dielectric probe [39].

It's crucial to also determine the temperature-related material properties of sweet potatoes. This can be done by determining their dielectric and

conductive properties as a function of temperature using a heating plate, digital thermometer, high-temperature probe [59], and VNA at 2.45 GHz. The sweet potato is sliced into 1 cm thick pieces and placed on the heating plate, with the probe positioned on its surface, as depicted in figure 5.5.

The material properties of the sweet potato, calculated as described above, are presented in table 5.2. The electrical conductivity of the sweet potato decreases from 2.6 S/m at room temperature to 2.1 S/m at 60°C, then increases above 60°C due to the formation of water between the probe and the sweet potato, resulting in a similar trend for the dielectric constant ( $\epsilon_r$ ). The measurement method has a 10 % uncertainty. The changes in material properties with temperature for sweet potatoes were compared to those of the ex-vivo liver below 80°C, as reported in [36], and showed similar trends. The temperature-dependent dielectric properties of the sweet potato ( $\epsilon_r$  and  $\sigma$ ) at 2.45 GHz are illustrated in figure 5.6.

Table 5.2: Dielectric properties of sweet potato at 2.45 GHz in 20-75 °C temperature range [39].

Temperature	Relative Permittivity ( $\epsilon_r$ )	Electrical Conductivity ( $\sigma$ )
21 °C	57.5	2.6 S/m
39 °C	55.6	2.2 S/m
60 °C	50.7	2.1 S/m
75 °C	55.1	2.8 S/m

### 5.2.3 Liver Phantoms

The other type of MUT used as a substitute for liver in microwave ablation monitoring experiments is phantom materials synthesized with polyvinylpyrrolidone (PVP) and Triton X-100 (TX-100) materials. In [37], PVP and salt (NaCl) are used to produce phantoms with tissue equivalent dielectric properties. Different concentration of PVP and NaCl results in a range of  $\epsilon_r$  (45 to 78) and  $\sigma$  (0.1 to 2 S/m) values, the range includes the dielectric properties of the liver. Thus, liver phantoms can be realized with PVP and NaCl. Agar another substance can also be used as a gelling agent for the phantoms. There is also an online phantom recipe generator for PVP-based phantoms reported in this work by the advanced MRI (AMRI) group (available at: <https://www.amri.ninds.nih.gov/about.htm>).

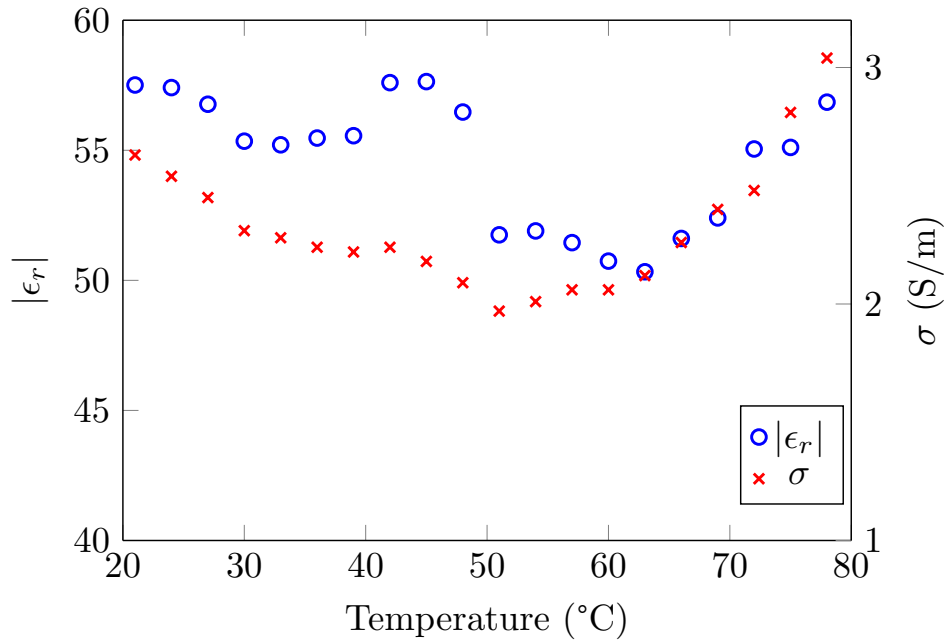


Figure 5.6: Change in dielectric constant and electrical conductivity of SP with the temperature at 2.45 GHz [39].

Similarly in [38], TX-100 and NaCl concentrations are used to synthesize dielectric-equivalent phantoms of various human tissue materials including the liver. According to [38], 30% volume concentration of TX-100 and 5 g/L of NaCl can produce  $\epsilon_r$  of 44.9 and  $\sigma$  of 1.1 S/m at 1.5 GHz as per cole-cole model.

In parallel work, [60], the liver phantom is prepared with PVP, NaCl, Agar, and distilled water. 350 ml of water is taken in which 2.189 g NaCl, 219.62 g of PVP, and 11.44 g of Agar are mixed with a prescribed method. The  $\epsilon_r$  and  $\sigma$  of this phantom is measured with dielectric probe and the formula's described in equations (4.5), (4.6), (4.7), and (4.8). The value of K used for the calculation is derived from a separate work [61], as  $1.1 \times 10^{-14}$ . The dielectric probe used is a high-temperature probe 'option 101' of the N1501A dielectric probe kit by Keysight technologies [59], as shown in figure 5.7. The temperature dispersive  $\epsilon_r$  and  $\sigma$  are measured as shown in figure 5.8. The  $\epsilon_r$  is 47.4 at 25 °C and drops to 30.9 at 65 °C whereas the  $\sigma$  at 25 °C is 2.09 S/m at it drops to 1.32 S/m at 65 °C.



Figure 5.7: High-temperature probe option 101 of N1501A dielectric probe kit: 1. High-temperature probe. 2. High temperature short. 3. Conductive disk. [59].

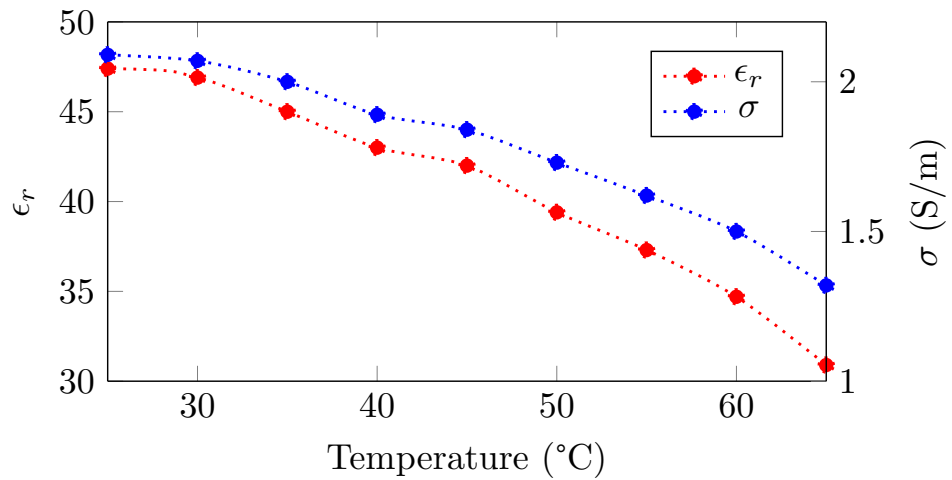


Figure 5.8: Temperature dispersive dielectric constant and electrical conductivity of PVP-based liver phantom at 2.45 GHz.

In another work, [62], TX-100-based liver phantoms are developed with different percentage concentrations of TX-100. A set of phantoms with 30 % and 40 % TX-100 concentrations are considered at 1.5 GHz as shown in table 5.3. The  $\epsilon_r$  of TX-100 phantom with 30 % concentration is measured

to be 68.8 at 30 °C. The value of  $\epsilon_r$  drops to 57.6 at 40 °C but then again rises to 64.9 at 50 °C. Afterward, it again drops slightly to 62.9 at 55 °C but then gradually rises to 66.3 at 70 °C at the end of the experiment. The  $\sigma$  value is measured to be 2.21 S/m at 30 °C and it drops to 1.89 at 55 °C but then again slightly rises and stabilizes at 2.02 S/m at 70 °C which is the end of the experiment. Similarly, with TX-100 phantom with 40 % concentration, the value of  $\epsilon_r$  oscillates between 41.6 and 57.7 at different temperatures between 30 °C and 70 °C. The value of  $\sigma$  for TX-100 phantom with 40 % concentration, 1.93 S/m and 1.41 S/m between 30-70 °C temperature range. The temperature dispersive dielectric properties of TX-100 phantom with 30 % and 40 % concentration at 1.5 GHz are measured as shown in figure 5.9 and figure 5.10 respectively.

Table 5.3: Recipe for salt, distilled water and TX-100-based liver phantoms at 1.5 GHz [62].

TX-100	30 %	40 %)
Water	1050 ml	600 ml
NaCl	7.5 g	5 g
TX-100	450 ml	400 ml
Total	1500 ml	1000 ml

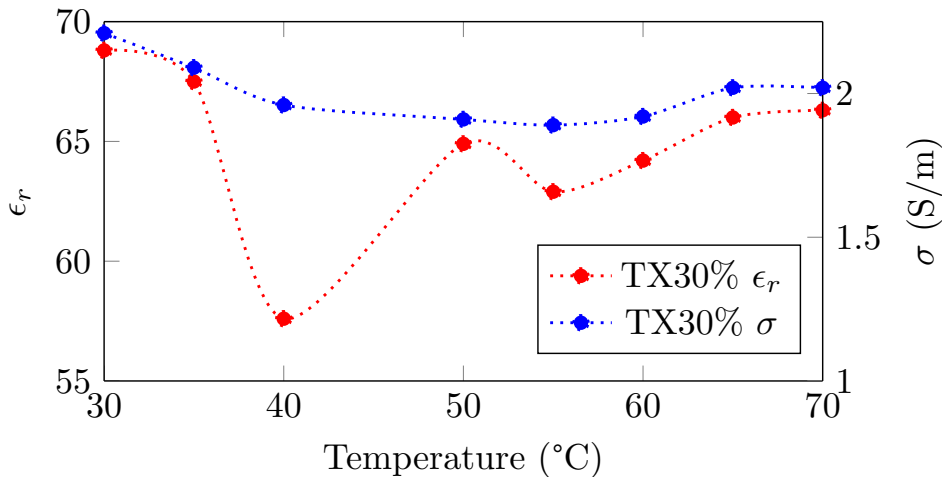


Figure 5.9: Temperature dispersive dielectric constant and electrical conductivity of TX-100 phantom with 30 % concentration at 1.5 GHz.

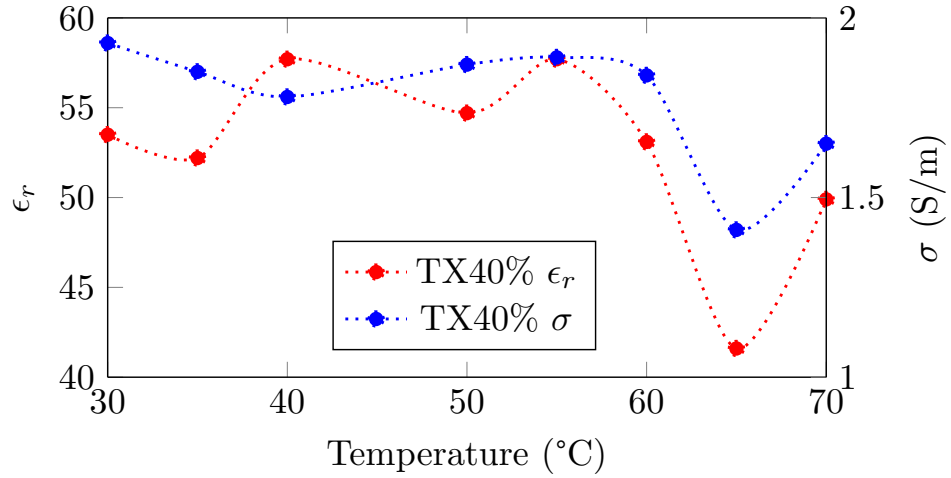


Figure 5.10: Temperature dispersive dielectric constant and electrical conductivity of TX-100 phantom with 40 % concentration at 1.5 GHz.

Table 5.4: TX-100 based liver phantoms for cold and hot liver at 2.45 GHz. [63]

TX-100 Concentration	With NaCl	Without NaCl
	$\epsilon_r, \sigma$	$\epsilon_r, \sigma$
TX-100 30 %	47.96, 2.01 S/m	47.12, 1.55 S/m
TX-100 70 %	12.21, 0.97 S/m	15.05, 0.96 S/m

It can be seen in both TX-100 and PVP-based liver phantoms that temperature dispersion of dielectric properties is not enough to meet the range the dispersion of dielectric properties an animal liver goes through during microwave ablation [36]. For this reason, another idea is adopted in [63], to produce separate phantoms for hot and cold livers, each corresponding to the respective dielectric properties of the hot and cold liver. Each phantom has then two variants: one with NaCl and one without NaCl. K factor of  $1.34 \times 10^{-14}$  is used in this study for the calculation of dielectric properties of phantoms derived from [64]. The phantom equivalent of the cold liver is TX-100 (30 %), without NaCl it has  $\epsilon_r$  of 47.12 and  $\sigma$  of 1.55 S/m which corresponds to the properties of the liver at 20 °C according to [36]. The phantom equivalent of the hot liver is TX-100 (70 %), without NaCl it has  $\epsilon_r$  of 15.05 and  $\sigma$  of 0.96 S/m which corresponds to the properties of the liver at 100 °C according to [36]. The properties of hot and cold liver

phantoms are tabulated in table 5.4. The TX-100 phantoms of different concentrations are shown in figure 5.11.



Figure 5.11: Phantoms with 30 %, 50 %, 60 % and 70 % concentration of TX-100.

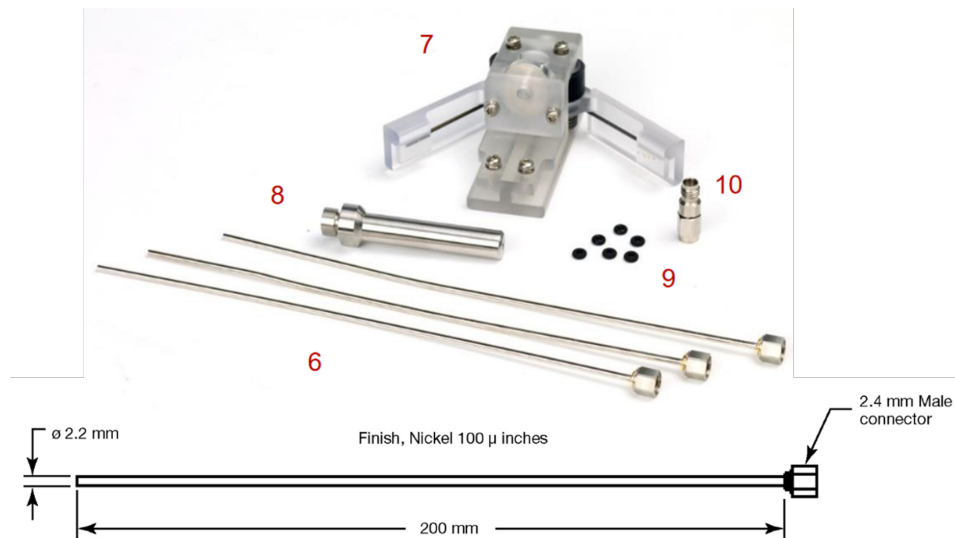


Figure 5.12: Drawing and contents of slim form probe 'option 102' of keysight N1501A dielectric probe kit: 6. Slim form probe. 7. Slim form short. 8. Slim form probe holder bracket. 9. O-rings 10. SMA adapter. [52].

The TX-100 phantoms are also measured with a slim-form probe and keysight software for the calculation of dielectric properties. The slim-form probe is described in 'option 102' of the N1501A dielectric probe kit by Keysight technologies [59], as shown in figure 5.12. The slim form

probe is more suitable for measuring liquid phantoms and can be easily inserted inside an animal liver during microwave ablation of the liver for measuring dielectric properties. Measured with slim form probe and keysight software tool, the hot liver phantom (TX100 70%) has  $|\epsilon_r|$  of 10.40 and  $\epsilon$  of 0.66 S/m while the cold liver phantom (TX100 30%) has  $|\epsilon_r|$  of 46.51 and  $\epsilon$  of 1.70 S/m. The measurements with the software tool are close to the values obtained from the K model developed in [61, 64].

### 5.3 Experimental Setup

---

After discussing all the MUTs and devices involved in validating the transmission based method for microwave ablation monitoring, the experimental setups for all the MUTs are discussed. To start with, the experimental setup for transmission through liver phantom materials is discussed, followed by the transmission setups through sweet potatoes and for ex-vivo liver experiments.

#### 5.3.1 Setup for Liver phantom experiments

For measuring the transmission through the two phantoms materials TX-100 70% and TX-100 30% corresponding to hot and cold liver tissues respectively, an experimental setup is developed which consists of an acrylic glass container divided by a 1 mm thin polyethylene separation plate. The MWA applicator is dipped into the hot phantom material compartment which is filled with TX-100 70%, through a fastening cover, whereas the receiving BMA (dipped type) is dipped in the cold phantom material compartment filled with TX-100 30% at various distances from the applicator, as shown in the figure 5.13.

There are two positions for the applicator 1 cm away from the separation plate and 2 cm from the separation plate. On the other hand, the dipped BMA has four possible positions 1 cm, 2 cm, 3 cm, and 4 cm from the separation plate. So this setup gives an equivalent of two ablation zone radii 1 cm and 2 cm or ablation zone diameters of 2 cm and 4 cm and an overall distance between applicator and antenna of 2 cm up to 6 cm. However, the overlapping distances for 2 cm and 4 cm ablation zone diameters are 3 cm, 4 cm, and 5 cm at which the transmission through two different equiv-



alent ablation zones could be compared. The setup is further improved in [65] by having a sliding mechanism to change the positions of both the antenna and applicator in cold and hot tissue compartments as shown in figure 5.14.

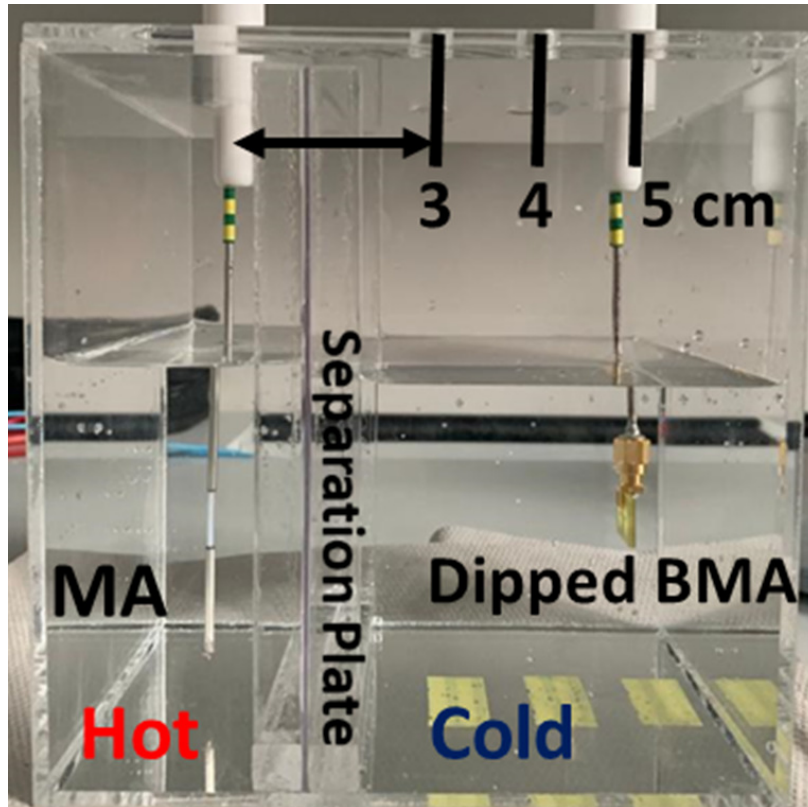


Figure 5.13: Planar phantom setup for two-layer hot and cold liver phantom transmission experiments: BMA & microwave applicator dipped in TX-100 30% (cold) and TX-100 70% (hot) tissue phantoms respectively at 3 cm, 4 cm and 5 cm fixed distances between the applicator and BMA [63].

In another parallel work, [66], an alternative setup is developed by inserting cylinders of different diameters ( $r$ ) filled with TX-100 70% (hot liver) into a cubic glass container filled with TX-100 30% (cold liver). The applicator is inserted in the hot liver cylinder and the antennas are placed around the applicator at different positions with a distance ( $R$ ) from the applicator as shown in figure 5.15. Furthermore, an RF source and spectrum analyzers are used to analyze the transmission through a variable distance of TX-100 30% and 70% solutions. Another elliptical cross-sectional form

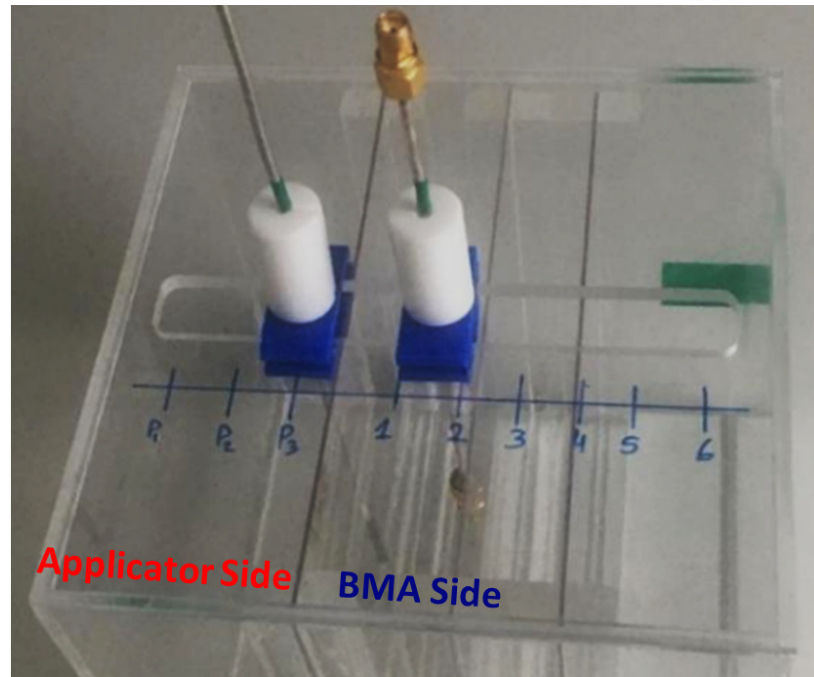


Figure 5.14: Planar phantom setup with a sliding mechanism for moving the applicator and BMA during the liver phantom transmission experiments [65].

of the setup similar to a patients belly is developed in [67], as shown in figure 5.16. The distance between the applicator and antenna ( $R$ ) ranges from 4 cm to 9 cm while the radius ( $r$ ) of hot liver phantom (TX 70%) ranges from 1 cm to 4cm.

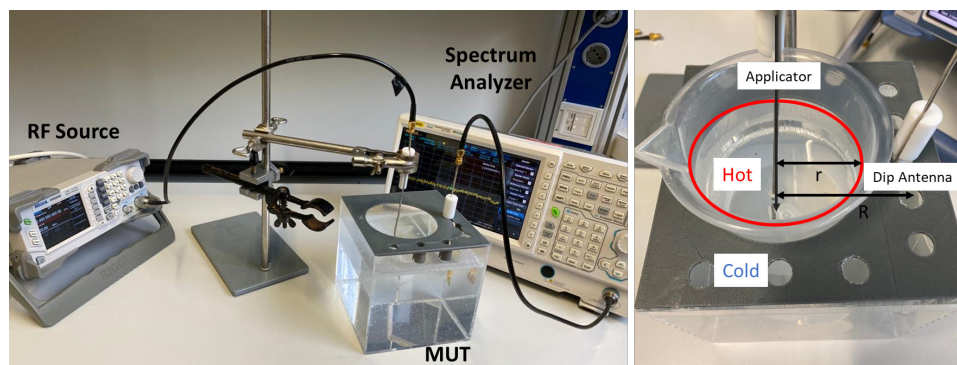


Figure 5.15: Cylindrical phantom experimental setup of two-layer hot and cold liver phantom for transmission experiments with variable hot tissue diameters ( $r$ ) and four fixed distances between the applicator and BMA [66].

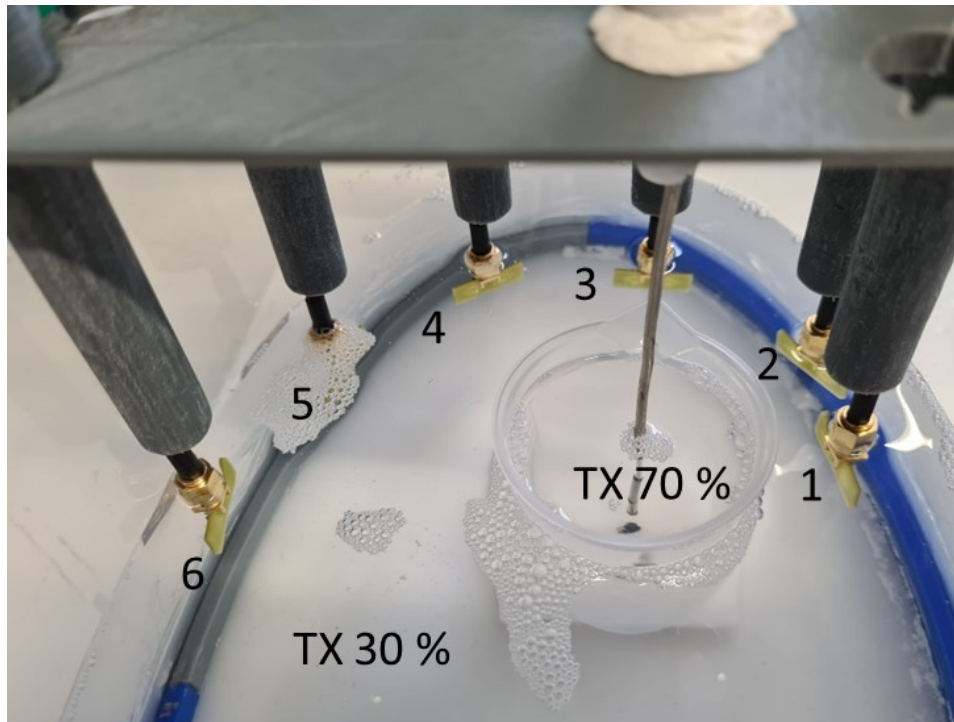


Figure 5.16: Elliptical cross-sectional phantom setup of two-layer hot and cold liver phantom for transmission experiments with variable hot tissue diameters ( $r$ ) and 6 fixed distances between the applicator and BMA [67].

### 5.3.2 Setup for transmission through sweet potato

The setup for the microwave ablation experiment using sweet potatoes in an anechoic chamber is depicted in figure 5.17. One end of the sweet potato is cut to accommodate the BMA, which is then securely attached to the sweet potato surface using rubber bands to eliminate any air gap. The center-to-center distance between the BMA and the applicator's slot is always 4 cm. A hole for inserting the microwave applicator is marked 4 cm below the sweet potato surface, with its precise position and depth determined using a level ruler. The hole for the temperature sensor is also marked.

As the MWA experiments with SP involves up to 80 W power, the experiments are conducted inside an anechoic chamber for safety reason. The high-power source and the spectrum analyzer used for stimulating high power and measured power received on the BMA, are outside the cham-

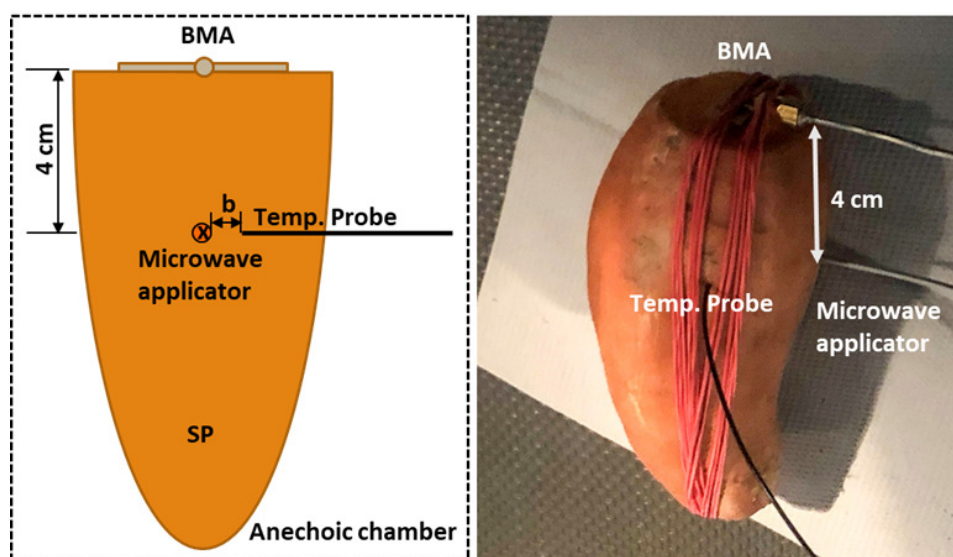


Figure 5.17: Experimental setup for MWA monitoring and temperature measurement during MWA in SP [39].

ber and are connected to the ports on the walls of the chamber which carry/receive power to the microwave applicator and from the BMA inside the chamber. Therefore, it is important to measure the loss in the cable network for the interconnection of all devices. For this purpose, a measurement setup as shown in figure 5.18 is devised. To quantify the loss incurred due to the N-cables and adapters, a transmission measurement is conducted. A signal generator and spectrum analyzer are connected to the N-connections on the wall of the anechoic chamber from outside and then two additional N-cables are connected inside the chamber and short-circuited to each other via N-N female adapters. To safeguard the spectrum analyzer, a 30 dB RF attenuator is used when the input power exceeds +30 dBm, which is the maximum power rating of the spectrum analyzer. A 10 dBm input power at 2.45 GHz is supplied from the signal generator, and the received power at the spectrum analyzer is -25.8 dBm, resulting in a total loss of 35.8 dB, including a network loss of 5.8 dB.

Double-distilled water is used as a medium to verify the measuring equipment for MWA experiments in an anechoic chamber as illustrated in figure 5.19. In the anechoic chamber, a water container with BMA on the water's surface and a microwave applicator submerged 7.5 cm (the distance between the BMA center and the applicator slot) below the water's surface

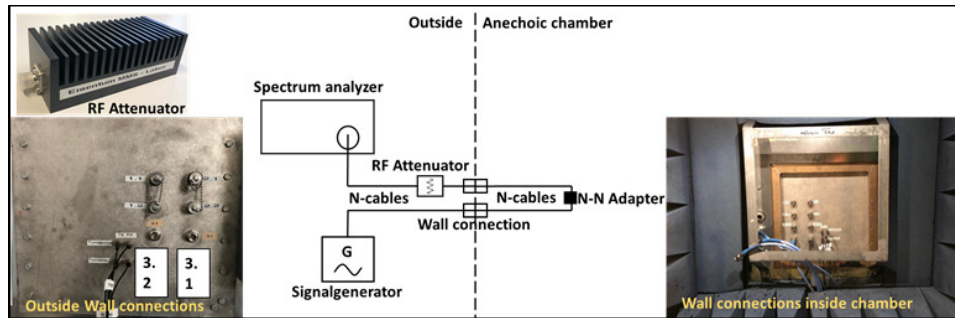


Figure 5.18: Calibration of the test setup for measuring the network loss due to power cables [39].

are used. The N connectors on the chamber wall are connected to the BMA and the applicator. A received signal of  $-40.6$  dBm is observed with a transmit power of  $47$  dBm at  $2.45$  GHz. The attenuation in the double-distilled water is  $51.8$  dB, which is obtained after subtracting the network loss of  $35.8$  dB from the overall power loss of  $87.6$  dB. This value closely agrees with the value of  $51.5$  dB loss obtained from the simulation of this setup in CST microwave studio.

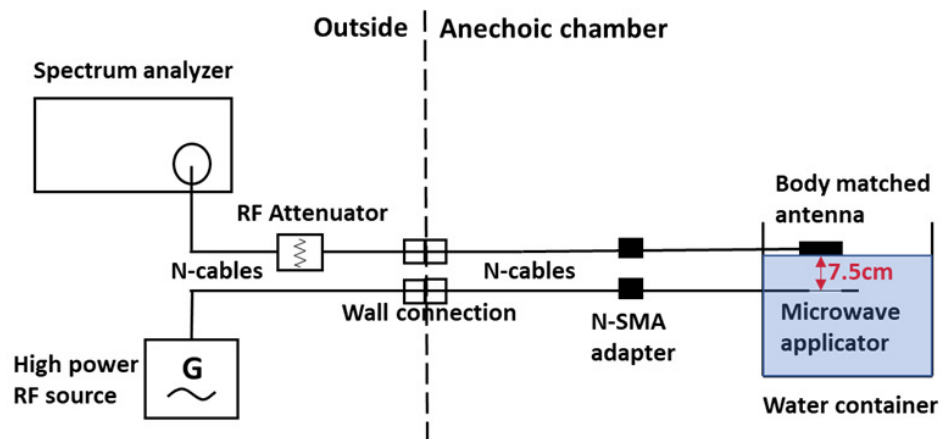


Figure 5.19: Testing of the experimental setup for MWA experiments in water as a medium [39].

### 5.3.3 Ex-vivo Liver Ablation Setup

The measurement setup of ex-vivo liver ablation experiments is similar to the measurement setup used for sweet potato experiments; however,

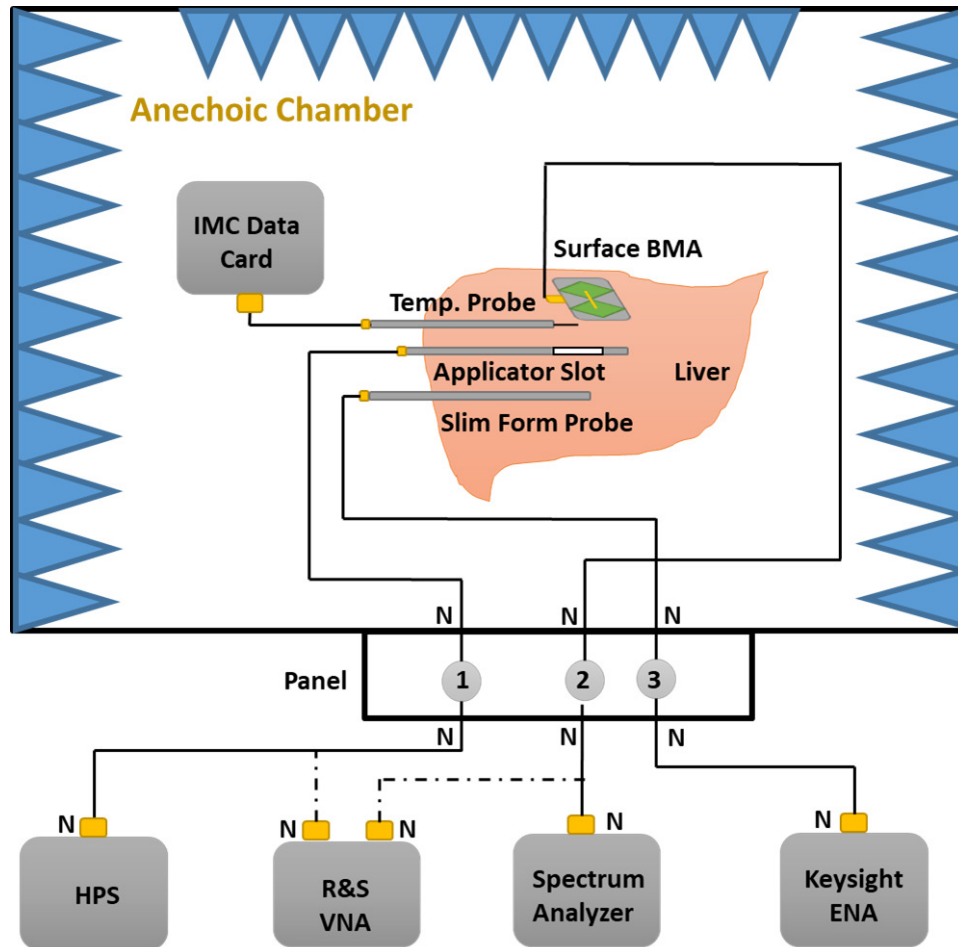


Figure 5.20: Block diagram of test setup inside and outside the anechoic chamber for: (i) Measuring dielectric properties of liver during MWA using slim-form probe. (ii) Measurement of temperature near ablation zone during MWA. (iii) Monitoring of received and reflected power during MWA in ex-vivo liver.

there is an addition in the setup for measurements of dielectric properties of the liver during and after the ablation. The measurement setup for monitoring MWA in the ex-vivo liver is shown in figure 5.20.

The signals are fed in and out via a panel of  $N$  connectors on the wall of the chamber. Three ports are used: port 1 is assigned to the microwave applicator inserted into the liver inside the chamber and outside to HPS (during the ablation) and R&S VNA (before and after ablation) for measurement of  $S_{11}$ . Port 2 is attached to the BMA inside the chamber placed on the surface of the liver sample and outside to the spectrum analyzer (dur-

ing ablation) and R&S VNA (before and after ablation) for measurement of  $S_{22}$ . Both, port 1 and port 2 with R&S VNA contribute to the measurement of  $S_{21}$  before and after the ablation. Port 3 is used for the measurement of liver properties during and after the ablation via a slim-form probe and ENA network analyzer from Keysight Technologies [59]. Furthermore, the temperature is measured in the ablation zone of the liver during and after the ablation with the help of fiber optic temperature probes from IMC [68] and LumaSense Technologies [69]. The temperature probe is guided near the applicator slot with the help of a catheter as shown in figure 5.21. The temperature data is stored in an IMC data card placed in AC and is later retrieved.



Figure 5.21: Preparation of the temperature sensor using the catheter as a guide for positioning in the liver tissue. a) Catheter tip is parallel to the applicator slot center. b) Measuring tip of the temperature sensor is parallel to the applicator slot center. c) Catheter rod for cleaning the guide.

The actual experimental setup is shown in figure 5.22. A large liver volume is cut off with fewer large blood vessels. The microwave applicator is inserted horizontally into the tissue 4 cm below the surface of the liver. The BMA is placed on the surface of the liver exactly above and parallel to the applicator slot and it is made sure that there is no air gap between the liver surface and BMA. To measure the material properties of the liver during MWA with the slim-form dielectric probe, the microwave power is switched off every minute to record the changing dielectric properties. This results in some MWA experiments with switching microwave power instead of continuous power. After the experiment, the liver sample is cut to optically measure the short-axis diameter (SAD) and long-axis diameter (LAD) of the ablation zone.

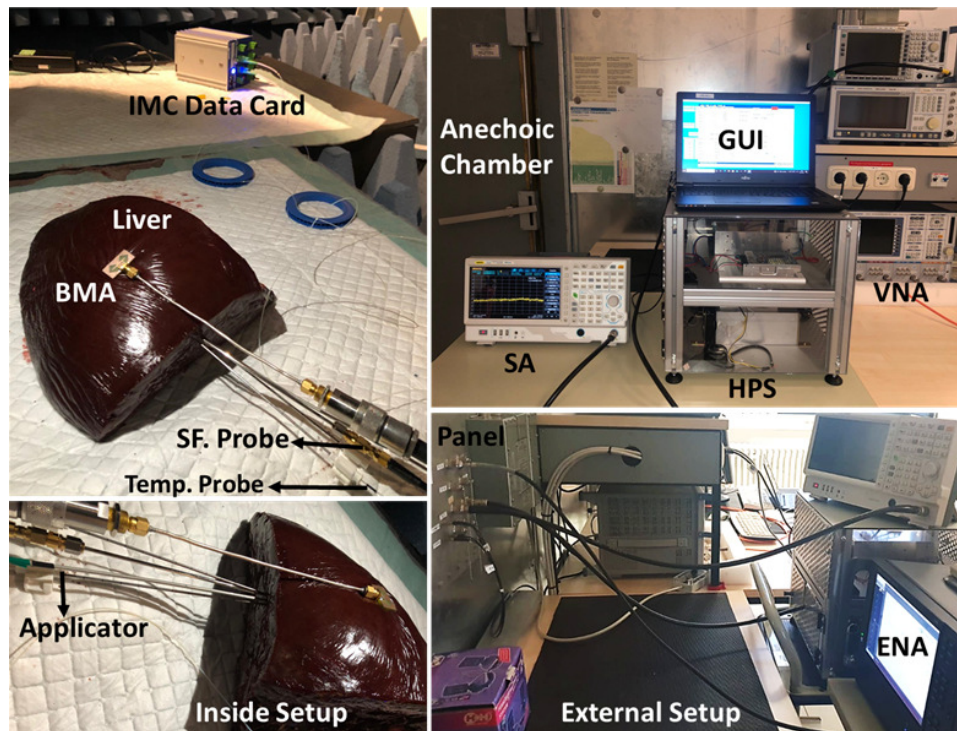


Figure 5.22: Experimental setup corresponding to the block diagram shown in figure 5.20 for measuring of dielectric properties of liver, temperature near ablation zone, and monitoring received and reflected power during MWA in the ex-vivo liver in an anechoic chamber.



# 6

## Simulations and Measurements

In this chapter, the design of the microwave applicator, body-matched antennas, the simulation, and experiments of MWA with liver phantoms, sweet potatoes, and animal liver are presented. Firstly, the design of a single-slot microwave applicator for transmitting high microwave power up to 80 W is presented. Afterward, the designs of linearly polarized and circularly polarized body-matched for surface and dipped scenarios for monitoring of MWA are presented. Secondly, there are two types of simulation performed: firstly, simulation is performed in the CST studio suite to simulate microwave transmission through 2 layers of liver phantoms corresponding to hot and cold liver tissues. These simulations evaluate the theoretical model for the propagation of microwave power from the microwave applicator dipped in the hot liver phantom to the BMA dipped in the cold liver phantom as shown in figure 4.2. The other type of simulation is EM-thermal MWA simulations performed in the CST studio suite which emulate the ex-vivo MWA experiments performed in the animal liver. Similarly, three sets of experiments are performed with the three MUTs: liver phantoms, sweet potatoes, and animal liver, as discussed in the previous chapter.

### **6.1 Microwave applicator design**

---

A microwave applicator is a device to stimulate high power in a tissue material for microwave ablation. Microwave applicators for thermal ablation were first reported in the late 1970s for the treatment of malignant tumors [26, 27, 28]. A lot of research is going on to develop highly efficient and precise microwave applicators. Many different designs like monopole, dipole, slot, choked, and triaxial designs of microwave applicators are reported in

[70]. A recent design is reported in [71], in which a dual slot microwave applicator is introduced with a metallic sleeve. Another new microwave applicator design is reported in [72] for laparoscopic and robotic liver resection. In [73], a dual mode microwave applicator is presented to excite high power as well as measure the dielectric properties of the tissue material to guide it to the center of tumor tissue. Some of the issues like heating along the shaft of the microwave applicator which causes skin burns are overcome in the commercially produced applicators [74]. Additionally, in commercial microwave applicators, temperature sensors are also incorporated into the tip to give localized temperature information.

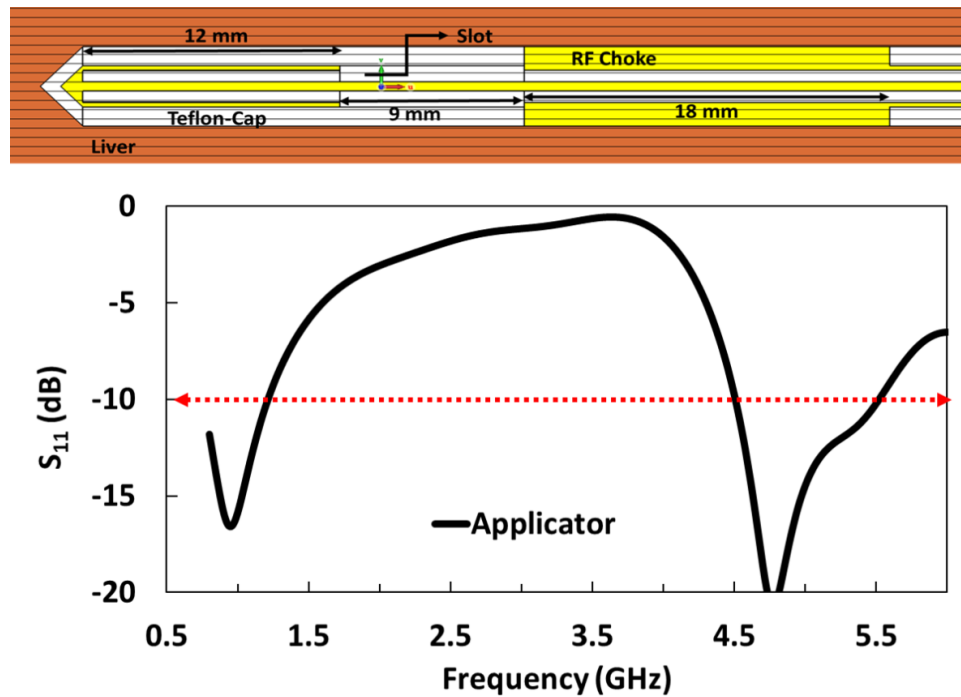


Figure 6.1: Microwave applicator initial design at 915 MHz and 4775 MHz. The simulation model and simulated reflection loss ( $S_{11}$ ) [51].

For purposes of this work, a single slot microwave applicator is designed and simulated using CST Studio Suite as shown in figure 6.1. The working principle is similar to an open-ended coaxial waveguide; however, the tip of the microwave applicator is made equal to a quarter wavelength of the design frequency to concentrate most of the power around the applicator's slot. Initially, a microwave applicator is designed with a tip of 12 mm and

a slot of 9mm with an RF choke of 18 mm. The applicator is simulated in liver material; the first resonance of the applicator is between 800 MHz to 1.2 GHz band which also includes 915 MHz ISM band whereas the second resonance is between 4.5-5.5 GHz. This design is reported in [51], the simulation model and reflection loss ( $S_{11}$ ) simulated result of the initially designed microwave applicator is shown in figure 6.1. The reflection loss is considered acceptable below -10 dB.

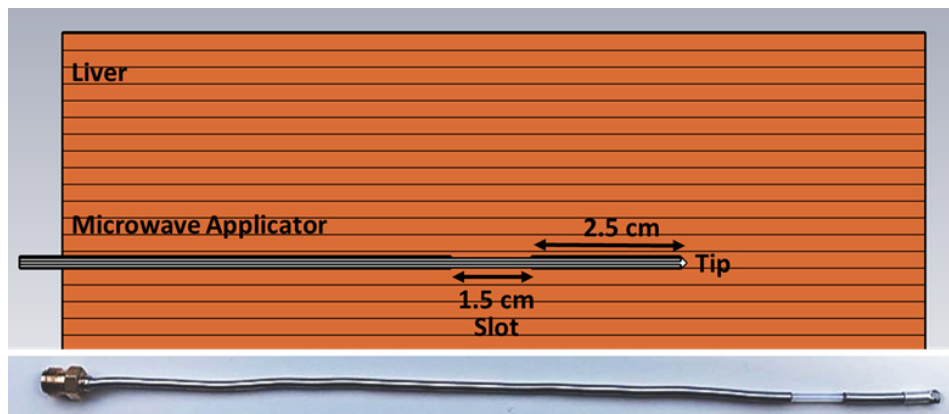


Figure 6.2: Microwave applicator design at 2.45 GHz: the simulation and fabricated model.

The design of the microwave applicator is iterated to resonate at the 2.4-2.5 GHz ISM band in which most microwave ablations systems operate and it is further simplified to remove the Teflon cap and the RF choke to make the applicator thinner so that it can be inserted into a MUT with ease. In the new design, the tip is 25 mm long and the slot is 15 mm making the radiating part of the applicator 4 cm long. The new design is also simulated in the CST studio suite, the applicator is inserted into a piece of liver. The applicator is fabricated with EZ86 semi-rigid, formable microwave cable [75]. The power handling of the cable is 92 W at 2 GHz and 65 W at 4 GHz and the nominal attenuation value is around 1 dB/m at 2.45 GHz. Therefore, it is suitable to excite about 80 W power into a MUT. A female SMA connector is assembled on one end of the applicator and at the other end, the outer conductor of the EZ86 cable is cut at 4cm from the tip and is slid 1.5 cm towards the open end and the leftover outer conductor is cut away. Finally, the tip of the inner conductor at the open end is connected to the outer conductor with a jacket sleeve and a crimping tool. The sim-

ulation and fabricated model of the microwave applicator are shown in figure 6.2.

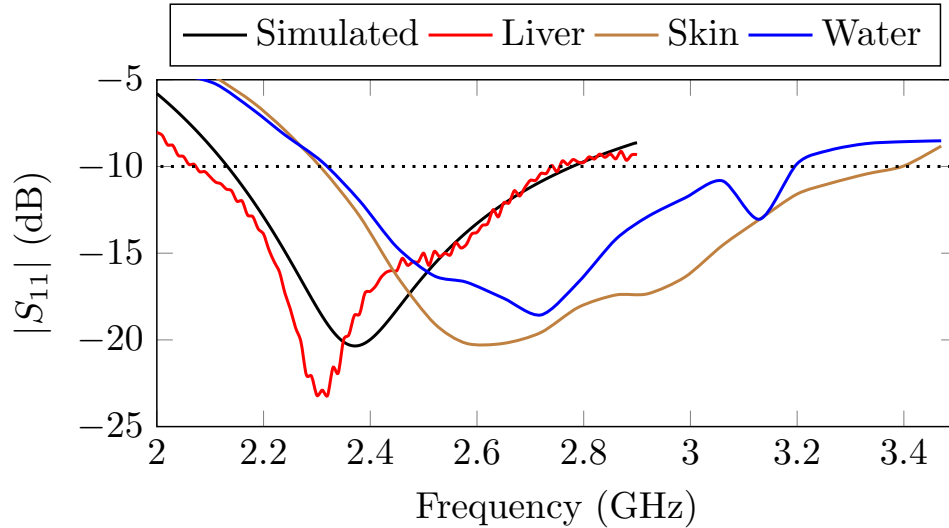


Figure 6.3: Simulated and measured reflection loss of microwave applicator inserted in the liver.

The reflection loss of the applicator is measured in freshly slaughtered animal liver, human skin, and water. The measured and simulated reflection loss of the microwave applicator in the liver is below -10 dB from 2.2-2.7 GHz; the results are comparable. The reflection loss of the applicator in water and skin is below -10 dB from 2.3-3.1 GHz as shown in fig 6.3. In all cases, the reflection loss is below -10 dB at 2.45 GHz, thus making the applicator suitable for ablation at the 2.4-2.5 GHz ISM band.

A commercial applicator Emprint from Medtronic [74] is also used for study purposes and also to benchmark the self-developed antenna. In the Emprint applicator, there are two thin water vessels used for cooling the applicator and a customized SMA connector to fit in the ablation system of Medtronic. The water pipes and the connector are cut and another standard SMA connector is attached to the power cable as shown in figure 6.4. For verifying the connector-cable assembly time-domain reflectivity (TDR) measurements are performed which show almost no reflections from the cable-connector interface which means that the applicator could be used for further experiments. The TDR measurements are shown in figure 6.5.

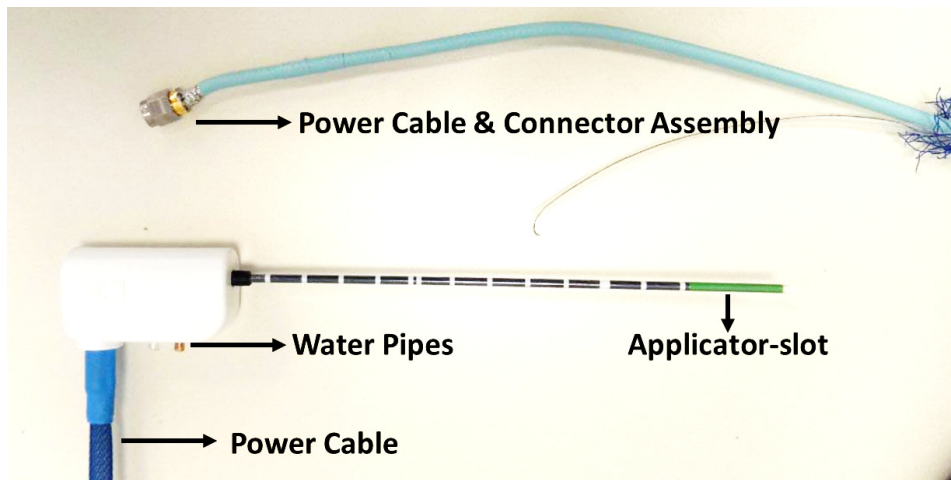


Figure 6.4: Emprint microwave applicator from Medtronic: The water pipes are removed and an SMA connector is installed at the other end of the power cable.

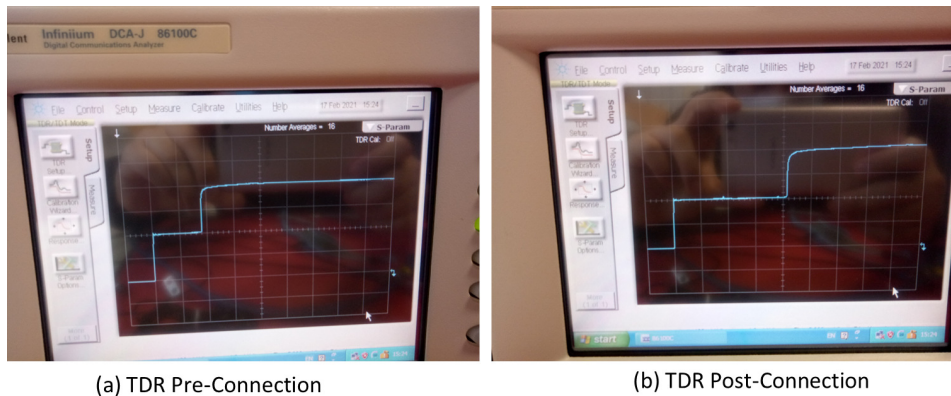


Figure 6.5: Time-domain reflectivity (TDR) measurements before and after connecting the SMA connector on the other end of the power cable. The change in the reflection point shows it is near the tip of the commercial applicator.

For true measurements, the Emprint applicator has to be filled with water to bring it into its design environment. At first, the reflection loss of the Emprint applicator is measured in air and then in water, skin, and sweet potato. The reflection loss of the Emprint applicator is around -5 dB in air and below -10 dB from 2.0-2.9 GHz in water and skin. Instead of the liver, the Emprint applicator is inserted in the sweet potato and the reflection loss is below -10 dB in the 2.4-2.5 GHz band. The reflection loss is -14 dB at 2.45 GHz in sweet potatoes. The measurement reflection loss results of

the Emprint applicator in water, skin, and sweet potato as shown in figure 6.6 are comparable with the results of reflection loss of the self-developed applicator as shown in figure 6.3.

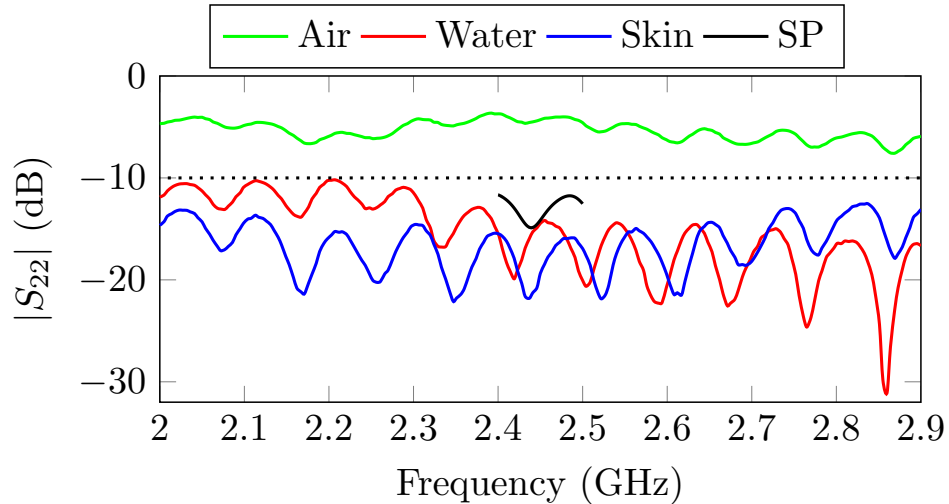


Figure 6.6: Reflection loss of Emprint applicator in air, water, skin, and sweet potato.

## 6.2 Body-matched Antennas

There are two types of body-matched antennas (BMAs) presented here: a linearly polarized bowtie-slot antenna and a circularly polarized circular patch antenna (CPA). The design, simulation, fabrication, and measurement of both antennas are presented here.

### 6.2.1 Bowtie-slot BMA

Bowtie antenna is a popular design for body-matched, microwave imaging, and implantable applications due to its flexible design, versatile feeding mechanisms, Ultra-wideband (UWB) impedance bandwidth, and a large antenna aperture contributing to a high geometry factor [76, 77, 78, 79]. In this work, a bowtie slot antenna with a co-planar waveguide (CPW) feed mechanism is designed. The antenna is matched to the liver surface as it is supposed to receive the power stimulated by the microwave applicator in the liver for ablating the tumor inside the liver.

Initially, a bowtie slot antenna is simulated in the CST studio suite on an FR-4 substrate. Two shunt stubs are coming out of the center of the bowtie slots for the impedance matching. The overall size of the antenna is 4 cm  $\times$  8 cm. The antenna is fabricated on an LPKF S100 circuit board plotter machine with the Boardmaster software [80]. An edge launch SMA connector is soldered with the antenna feed line [81]. The simulation and the fabricated model of the antenna are shown in figure 6.7. The antenna is measured on liver phantom prepared with PVP material ( as shown in figure 5.8) with Rhode & Schwarz voltage network analyzer (VNA) ZVL13 [82], as shown in figure 6.8. The design has been presented in [51].

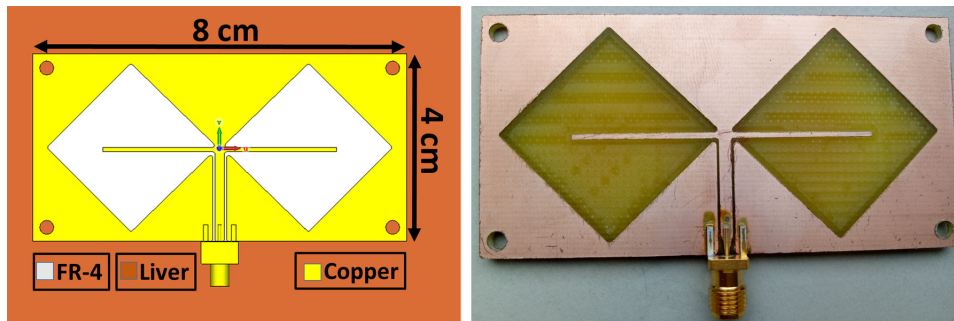


Figure 6.7: Simulated and fabricated model of UWB Bowtie-slot BMA on the liver.

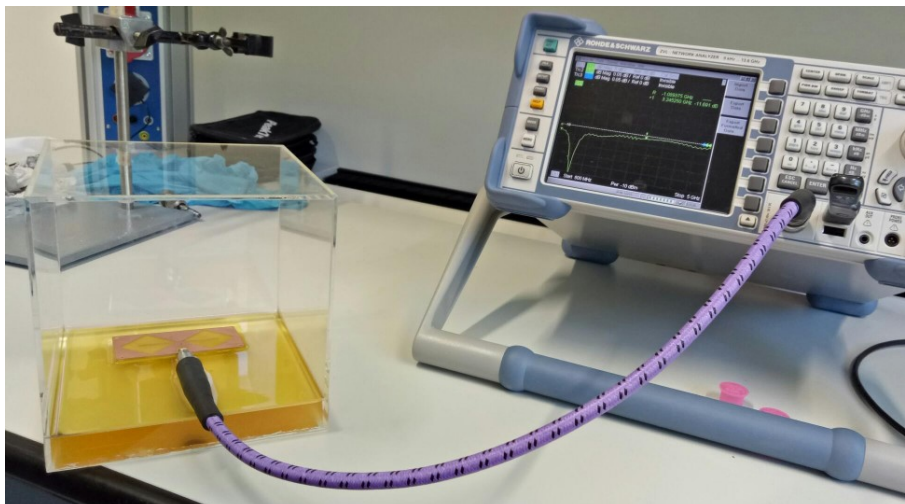


Figure 6.8: Measurement setup for reflection loss measurement of UWB Bowtie-slot BMA on PVP-based liver phantom.

As with BMAs which have the advantage of UWB reflection loss bandwidth due to being in contact with lossy human tissues. The simulated reflection

loss of the antenna on the liver surface is below -10 dB from 800 MHz to 6 GHz including all the ISM bands used for microwave ablation in the sub-6GHz category i.e. 915, 2450, and 5800 MHz. The antenna is measured on PVP-based liver phantom (see figure 5.8) without airgap and with airgap, on hand skin, and wearable jeans material. All the measured and simulated results are shown in figure 6.9. The reflection loss of the UWB bowtie-slot BMA is below -10 dB in simulation on the liver (black curve), measured on PVP-based liver phantom (red curve) and hand-skin (blue curve) in the 0.8-6 GHz band. However, the reflection loss deteriorates above -10 dB if there is an air gap between the antenna and liver phantom (brown curve) and also on jeans between antenna and skin (green curve). Therefore the antenna must be placed over the liver phantom without any air gap to function over the entire 0.8-6 GHz band. In the case of using the UWB bowtie-slot BMA on the skin surface, there should not be any hair or fabric between the antenna surface and the skin.

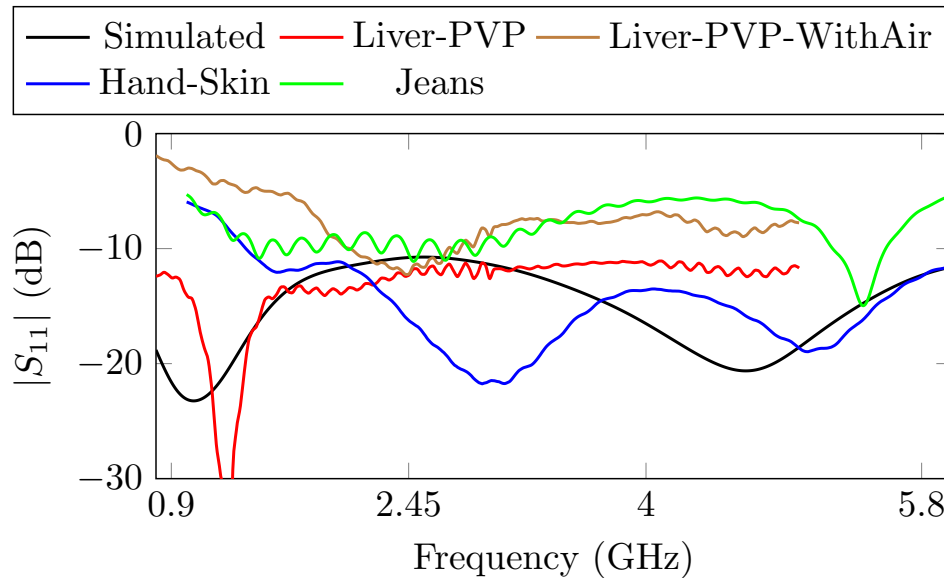


Figure 6.9: Simulated and measured reflection loss of UWB bowtie-slot BMA on PVP-based liver phantom, hand-skin, and jeans.

Later on, in research, only the 2.45 GHz band is used for microwave ablation; therefore, the BMA used to receive the power from the microwave applicator is designed only for 2.45 GHz which is half the size of the UWB bowtie-slot antenna. The advantage of having a smaller size is crucial as



a higher number of antennas can be placed on the liver surface for monitoring the power received from the microwave applicator during the ablation process. The newer version of the bowtie-slot antenna has two types: one is designed for the surface of the liver which could also be used on sweet potato and the other version called the 'dipped antenna' can be submerged into the liquid liver phantom for microwave ablation experiments. The simulated and fabricated models of the surface and dipped BMAs are shown in figure 6.10. The dipped antenna (21.58 mm × 10.53 mm) is slightly shorter than the surface antenna (22 mm × 11 mm); both the antennas are fabricated on an FR-4 substrate with 1.5 mm thickness and fed using the CPW feed mechanism.

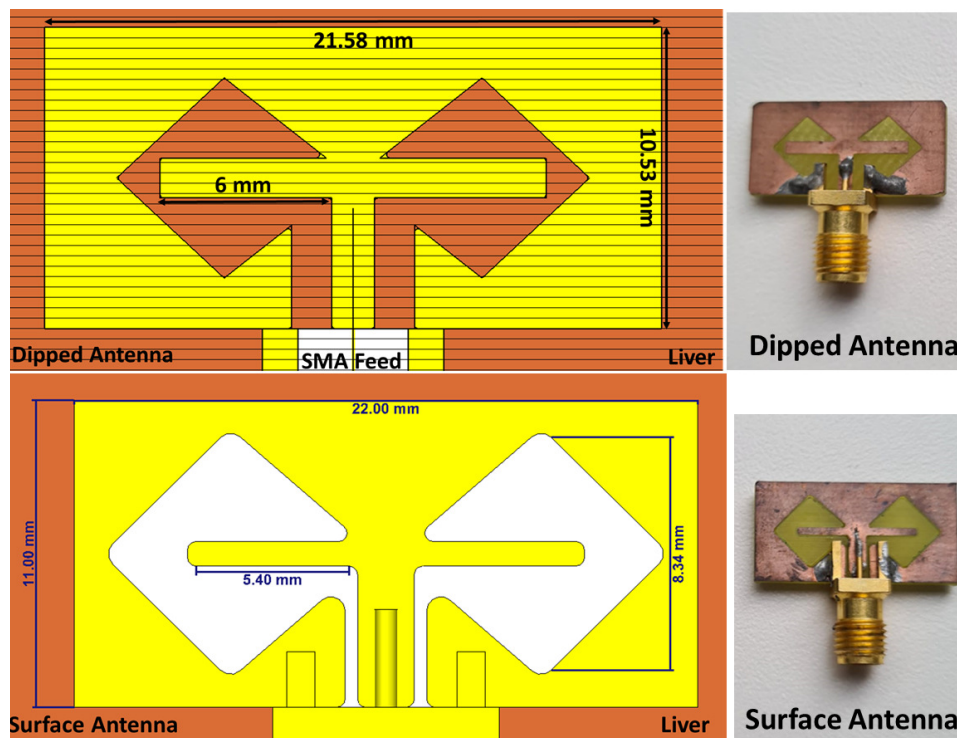


Figure 6.10: Simulated & fabricated models of bowtie-slot surface & dipped BMAs.

The dipped antenna is measured in tissue phantom material prepared with 30% TX-100 material and distilled water designated as cold liver in the previous chapter. On the other hand, the surface antenna is measured on a freshly slaughtered animal's liver. The measured and simulated reflection losses ( $|S_{22}|$ ) of both the antennas are shown in figure 6.11. The

simulated and measured reflection loss ( $|S_{22}|$ ) of the dipped antenna is just below -10 dB from 2.4-2.5 GHz and for the surface antenna the reflection loss is below -16 dB from 2.4-2.5 GHz. The overall reflection loss bandwidth of the surface antenna below -10 dB covers the 2.0-2.9 GHz frequency range. The resonance of the simulated surface antenna is at 2.52 GHz while the measured resonance of the surface antenna is at 2.22 GHz.

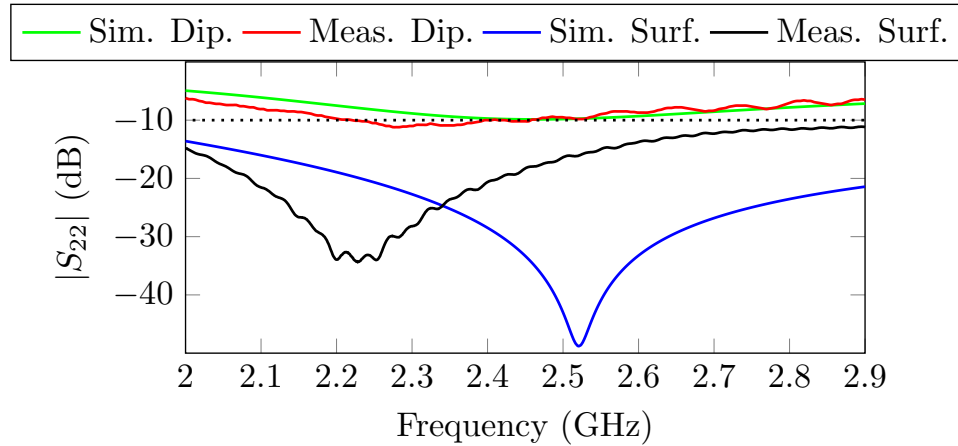


Figure 6.11: Simulated and measured reflection loss ( $|S_{22}|$ ) of surface BMA on the liver and dipped BMA in 30% TX-100 solution.

### 6.2.2 Circular Patch BMA

Circularly polarized antennas (CPA) placed on a tissue surface can receive a signal with an E-field of an arbitrary orientation from a microwave applicator or an implantable antenna inserted in the human body [83],[84],[51]. This novel application enables BMA placement on the tissue surface without concern for the orientation of the microwave applicator inserted into the human body. However, the air-tissue interface exhibits significant contrast in constitutive parameters, requiring a matching medium (MM) to be applied on the tissue surface to submerge the BMA [85]. This approach reduces the contrast between the BMA and the background, resulting in improved antenna performance. Circular polarization can be achieved in a microstrip patch antenna by exciting two orthogonal modes (TM<sub>10</sub>, TM<sub>01</sub>). This can be accomplished by truncating alternate edges of the patch antenna or feeding the antenna from two adjacent edges,

which are well-known techniques. In implantable or BMA applications, the lossy tissue material attached to the antenna significantly reduces its input impedance at the modal frequencies, allowing even the higher order modes (TM<sub>30</sub>, TM<sub>03</sub>) to be excited. Additionally, shorting pins and slots have also been used to create CP antennas for implantable biomedical applications [86], [87].

### Simulation

In an ex-vivo MWA experiment, a CPA designed to match the liver surface received a signal with arbitrary E-field orientation from a microwave applicator inserted into the liver [83]. To improve the matching of the CPA with the liver, a TX100-based liver phantom was used as a MM. The antenna was designed as a microstrip circular patch over a 1.5 mm thick FR-4 substrate and simulated in the CST studio suite, featuring two shorting pins and slots and a probe-fed SMA connector attached to the ground plane beneath the substrate. The antenna's far-field in the bore-sight direction was constituted by a liver tissue block  $(15\text{cm})^3$  placed in front of it. To further enhance the matching, the antenna was submerged in a 30 % concentrated TX-100-based liver phantom designated as "cold liver" in the previous section. Figure 6.12 outlines the simulation model, boundary conditions, and antenna design, with the antenna dimensions specified in table 6.1.

Table 6.1: Dimensions of CPA with and without MM [83].

Dimension	Without MM	With MM
Subrad	11.5 mm	10.9 mm
arclen, arclen2	2.05, 2.28 mm	3.54, 3.99 mm
arcwid, arcwid2	1.42, 0.40 mm	2.00, 0.40 mm
arcangle, arcangle2	10.4°, 34°	10°, 30°
arcrot, shang	15°, 19°	15°, 19°
$r_s, r_1, r_2$	0.635, 2.94, 1.5 mm	0.635, 3.35, 1 mm
w, $R_p, F_p$	2, 8.35, 6.68 mm	2.5, 7, 7.22 mm

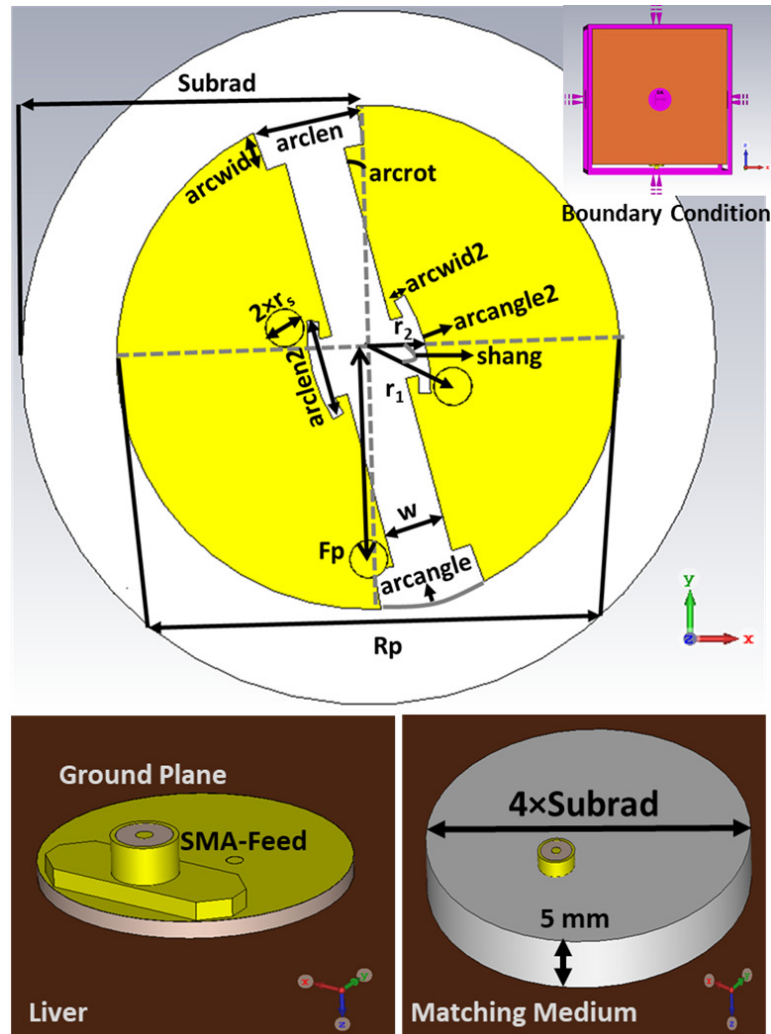


Figure 6.12: Design variables (shown in table 6.1), simulation models with & without MM, and boundary condition of circularly polarized CPA [83].

### Fabrication and measurements

The CPAs (with and without MM) are fabricated with an LPKF S100 Protomat machine on an FR-4 substrate with double-sided copper cladding and 1.5 mm thickness. The shorting pins are soldered on the patch connecting the ground and antenna layers. The pin of the probe-fed SMA connector is soldered on the antenna feeding point while the body of the connector is soldered to the ground. The shorting pins and the feeding

pin of the connector are carefully foiled after soldering to conform them to the surface of the antenna. The fabricated antennas with and without MM are shown in the figure 6.13.

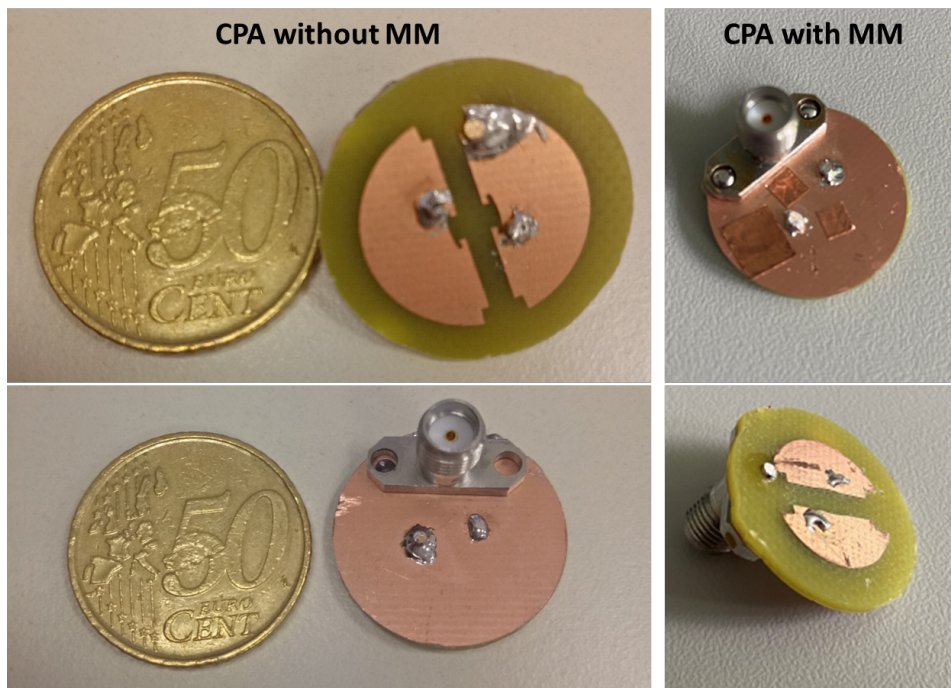


Figure 6.13: Top and back view of the fabricated CPA designs with and without matching medium in comparison with 50 cents coin.

The measurement of CPAs is supported by a parallel work [88]. The antennas are measured with R&S VNA on SP surface (substitute liver) with and without matching medium for reflection loss ( $S_{11}$ ) and transmission coefficient ( $S_{21}$ ) measurements. For the reflection loss measurements of CPA without MM, an antenna is simply fixed on the SP surface with the rubber bands so that there is no air gap between the SP surface and the antenna. On the other hand, The measurement of the CPA with MM is done by filling a plastic sleeve with TX-100 30% phantom as a coupling medium and dipping the antenna in it, and then putting it on the SP surface. The antenna is also measured on various types of skins such as hand, belly, and leg with TX-100 and electrode-gel couple mediums. The measurement setups for reflection loss measurements are shown in figure 6.14. The mea-

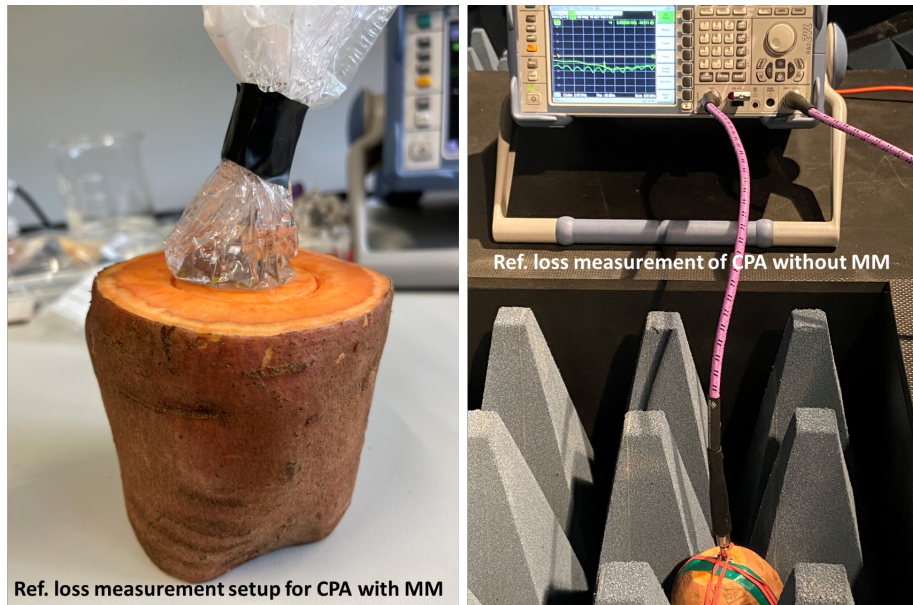


Figure 6.14: Test setups for measurement of reflection loss of the CPA with and without matching medium on sweet potato surface.

sured and simulated  $|S_{22}|$  result of the antenna with and without the MM is shown in Fig. 6.15.

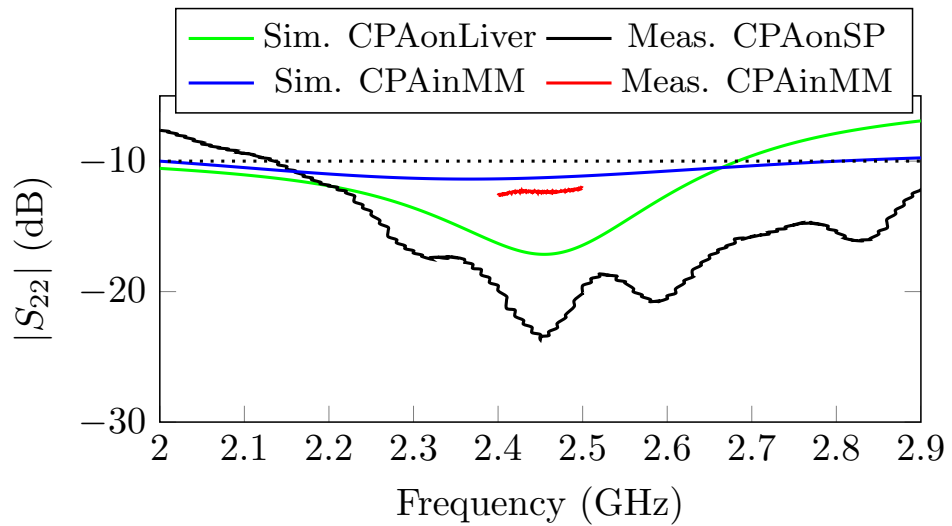


Figure 6.15: Simulated and measured reflection loss of CPA with and without MM on liver and sweet potato surfaces.

The reflection loss bandwidth of the antenna covers the ISM band (2.4-2.5 GHz). The reflection loss bandwidth is increased with the MM (2.0-2.9 GHz). The antenna is measured on sweet potato which is different than the simulation model in which it is simulated on a liver block. However, still the measured and simulated results agree due to similar properties of liver and sweet potato as discussed in previous chapter.

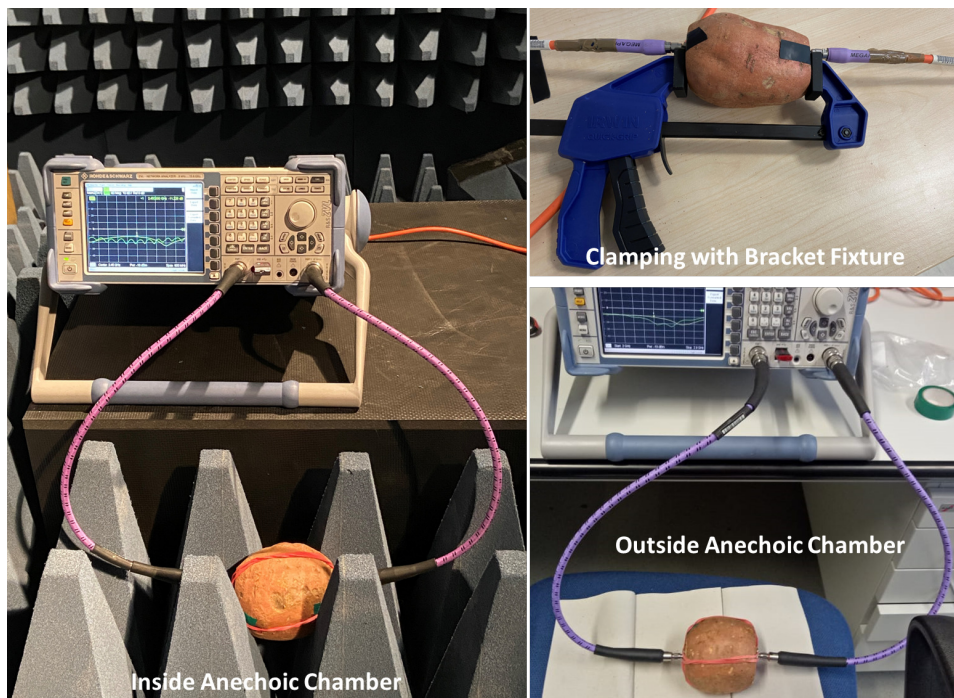


Figure 6.16: Measurement setups for transmission coefficient of CPA

The measurement of transmission coefficient ( $S_{21}$ ) is required for the calculation of AR. For the measurement, two antennas are fixed on the opposite sides of a SP with a bracket fixture or rubber bands to clamp them tightly on the SP surface so that there is no air gap between the antenna and SP surface. To measure the transmission through a sweet potato the transmit and receive antennas are rotated at  $0^\circ$ ,  $45^\circ$ , and  $90^\circ$  to each other. Both the antenna lie in the far-field from each other in a SP medium. The measurement is carried out outside and then inside an anechoic chamber to avoid reflections and interference from the surroundings. The axial ratio is calculated by finding the difference of  $S_{21}$  measurements at  $0^\circ$  and  $90^\circ$

as this difference is the ratio of horizontal and vertical E-field components which constitute the AR. Some of the measurement setups for transmission coefficient measurements of the CPAs are shown in the figure 6.16.

The measured transmission coefficient  $S_{21}$  of a transmit and receive CPAs fixed at the opposite ends of a 10 cm long SP and rotated at  $0^\circ$  and  $90^\circ$  to each other is shown in figure 6.17. It shows that the CPA rotated at  $90^\circ$  receives the signal within -3 dB of the signal received with no rotation ( $0^\circ$ ) between the 2.4-2.5 GHz band. While the simulated difference between linearly polarized bowtie-slot BMA antenna between cross pole and co-pole arrangements on 10 cm liver tissue is -33 dB. Thus CPA gives freedom of orientation in the placement of the antenna on the body.

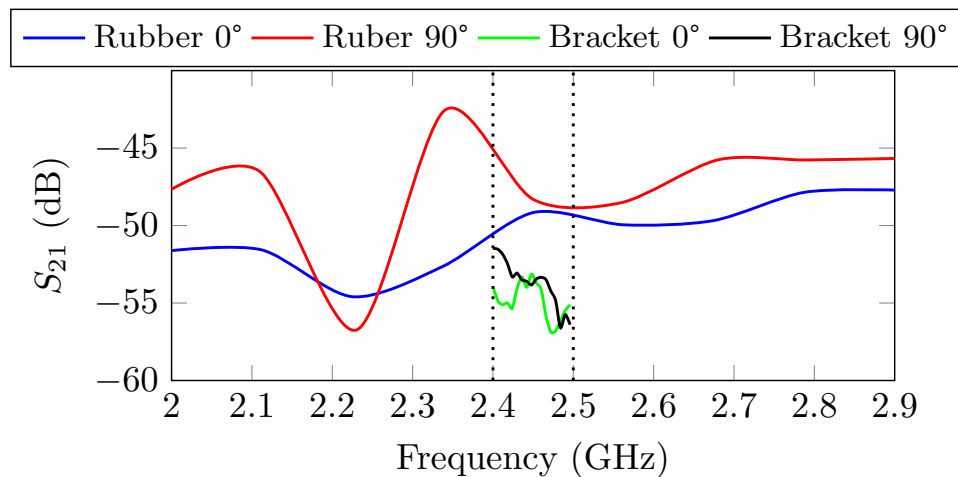


Figure 6.17: Measured  $S_{21}$  of CPAs rotated at  $0^\circ$  and  $90^\circ$  to each other.

Figure 6.18 compares the simulated AR bandwidth of the CPA with and without the MM. The simulated AR bandwidth of the antenna covers the ISM band (2.4-2.5 GHz), which is increased even more with the MM (2.14-2.90 GHz). The AR of the CPA is 0.3 at 2.45 GHz without the MM, while with the MM, it is 1.13. The figure also shows the calculated AR of the CPA inside and outside the anechoic chamber, which covers the required ISM band at 2.4-2.5 GHz. The AR with a bracket fixture is 0.66 at 2.45 GHz, while with a rubber band, it is 0.25.



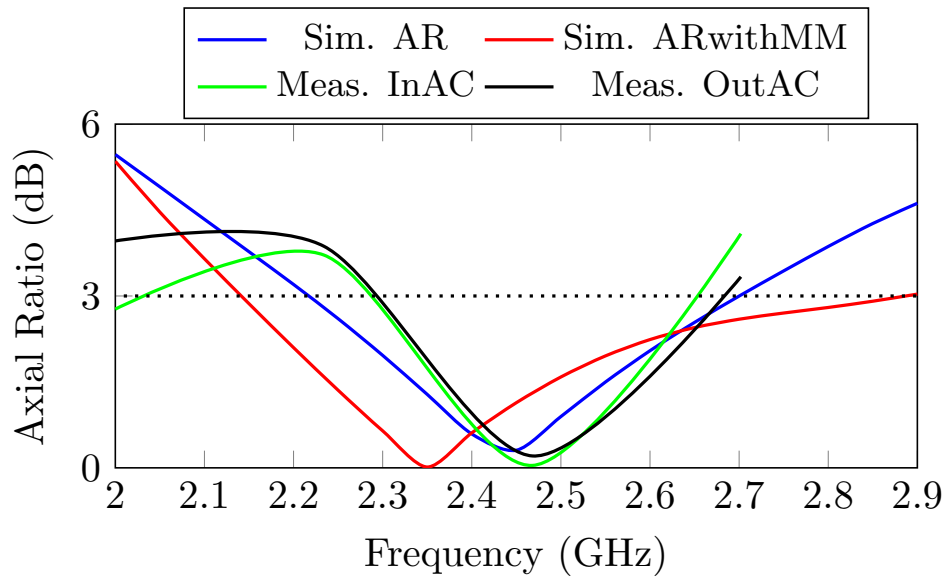


Figure 6.18: Simulated axial ratio of CPA with and without MM. Measured AR of CPA inside and outside Anechoic chamber.

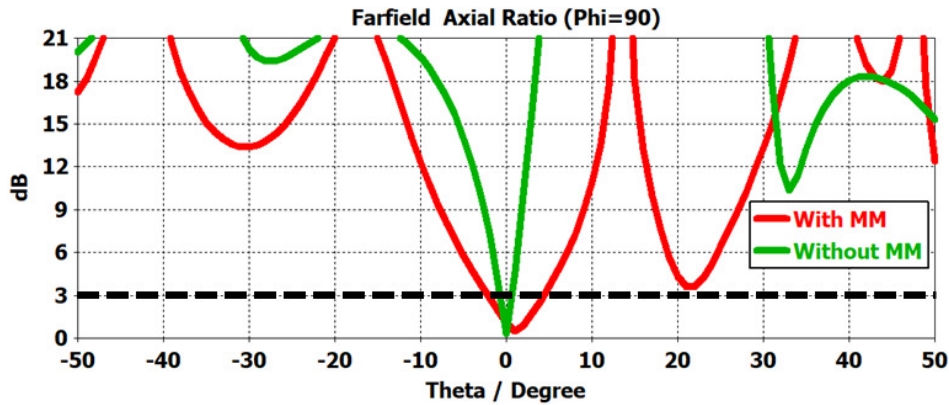


Figure 6.19: Simulated AR beam-width of the CPA at 2.45 GHz.

Figure 6.19 shows the simulated 3 dB AR beam-width of the circular patch CPA, which is 6 degrees around the bore-sight with the MM, compared to just 1 degree without the MM. This considerably increases the scan area of the antenna. Figure 6.20 shows the simulated gain of the circular patch CPA. The  $(15\text{cm})^3$  chunk of the lossy liver in front of the antenna with an electrical conductivity ( $\sigma$ ) of 1.7 S/m diminishes the forward gain of the

antenna compared to the backward gain. At 2.45 GHz, the simulated gain of the antenna is -42 dBi in the bore-sight direction.

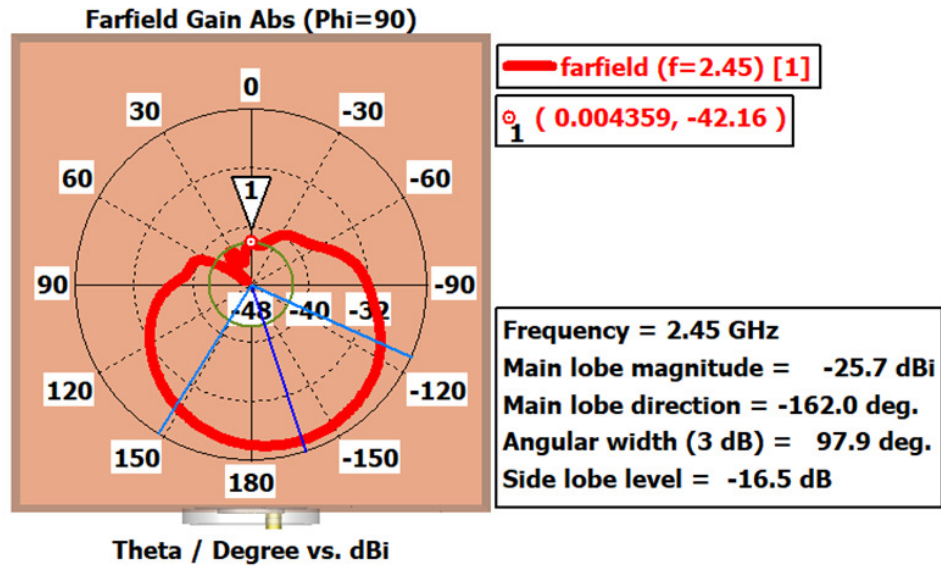


Figure 6.20: Simulated gain of CPA with MM at 2.45 GHz.

Thus, in conclusion, it can be said that CPA can be used as a surface BMA for monitoring MWA with a better degree of freedom of placement than a linearly polarized counterpart. Moreover, the probe feeding from the ground plane at the back makes the design convenient for placement on a body as compared to a side-fed bowtie-slot antenna with a CPW feed mechanism.

### 6.3 Microwave transmission through liver phantoms

Firstly, the values for the theoretical model are calculated for the transmission of microwave power from a hot tissue to a cold liver for a distance ( $R$ ) of 3 cm, 4 cm and 5 cm for different transmission distances through the hot liver ( $r$ ) using equation (4.22). Table 6.2 shows the value of the effective area of the bowtie-slot BMA ( $A_{eff}$ ), coupling factors ( $K1$  and  $K2$ ) of the microwave applicator, and the bowtie-slot BMA, the propagation constants ( $\alpha_1, \alpha_2$ ) in hot and cold liver at 2.45 GHz and transmission coefficient ( $T$ ) between the two tissues. The geometry factor ( $G$ ) given by equation (4.19)

Table 6.2: Values used for the theoretical model for EM transmission from hot to cold liver at 2.45 GHz [54].

Factor	$A_{eff}$	$K_1$	$K_2$	$T^2$	$\alpha_1(\frac{1}{m})$	$\alpha_2(\frac{1}{m})$
Value	2 cm <sup>2</sup>	0.94	0.81	0.4	49.35	65.57

is calculated for all the respective values of 'R': for 3 cm the value of 'G' is  $1.77 \times 10^{-2}$ , for 4cm the value of 'G' is  $9.95 \times 10^{-3}$  and for 5 cm the value of 'G' is  $6.37 \times 10^{-3}$ .

All the values obtained for the theoretical model are obtained from the measured data for reflection losses of the microwave applicator and the BMA and the measurement of the dielectric properties of TX-based hot and cold liver phantoms. To compare the calculated values of the transmission coefficient from the theoretical model with the experimental values, the experiments are performed to measure the transmission coefficient ( $S_{21}$ ) through the planar liver phantom setup as shown in figure 5.14. The distance between the antenna and the applicator (R) is fixed at 3 cm, 4 cm, and 5 cm and the transition distance (r) through the hot tissue (hot tissue radius) is 1 cm and 2 cm. The calculated and measured values of  $S_{21}$  with increasing hot tissue radius are shown in figure 6.21.

The calculated value of transmission coefficient ( $S_{21}$ ) for 3 cm distance (R) between the applicator and antenna ranges from -38 dB at 1 cm hot tissue distance (r) to -35.9 dB at 2.5 cm value of 'r'. Similarly for 'R' of 4 cm, the value of  $S_{21}$  ranges from -46.2 dB at 'r' of 1 cm to -43.3 at 'r' of 4 cm. Finally, for 5 cm 'R', the value of  $S_{21}$  ranges from -53.8 dB at 1 cm 'r' to -51 dB at 4 cm 'r'. According to the theoretical model,  $S_{21}$  has a linearly increasing trend with increasing 'r'. The experimental values of  $S_{21}$  for 'R' of 3 cm denoted by blue dots decrease from -35.8 dB at 'r' of 10 mm to -37.8 dB at 'r' of 20 mm. Conversely, there is an increase in the measured values (black dots) of  $S_{21}$  for both 4 cm and 5 cm distances when the hot tissue radius is doubled. For 'R' of 4 cm denoted by red dots the measured value of  $S_{21}$  increases from -44.3 dB at 'r' 10 mm to -39.8 dB at 'r' 20 mm and for 5 cm distance (black dots) the measured values increase from -49.0 dB at 'r' 10 mm to -44.5 dB at 'r' 20 mm.

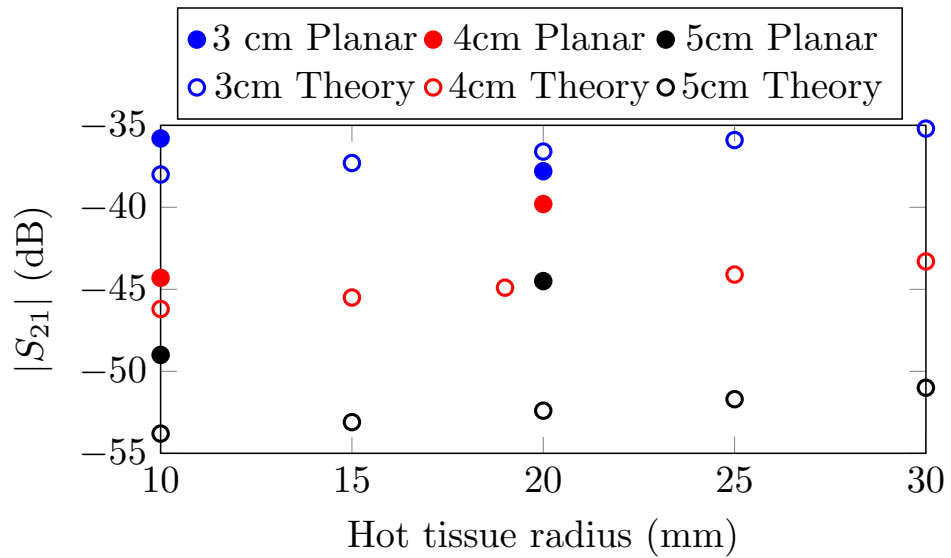


Figure 6.21: Variation in calculated and measured  $|S_{21}|$  values for different 3 cm, 4 cm, and 5 cm fixed distances between microwave applicator and BMAs dipped in hot and cold tissue phantoms in planar compartments with increasing transition distance ( $r$ ) through the hot tissue (hot tissue radius).

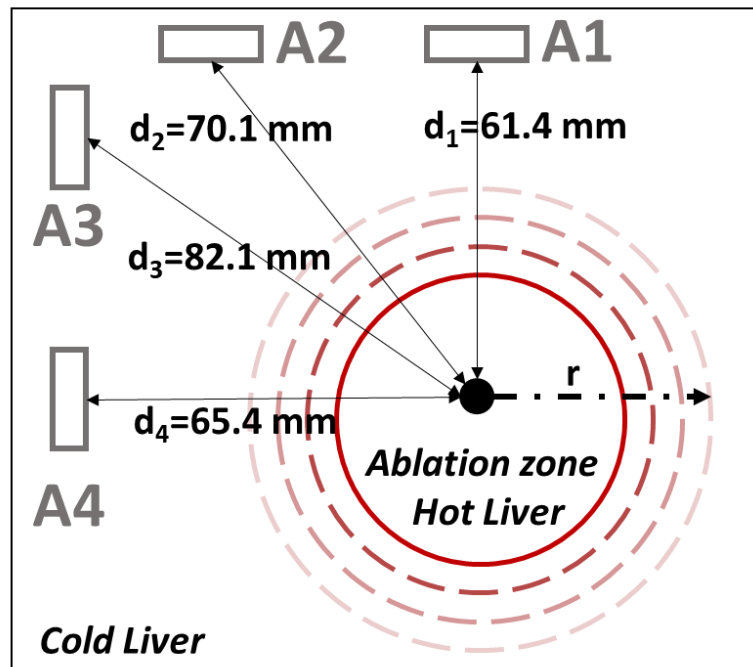


Figure 6.22: Simulation model of BMAs and microwave applicator dipped in two layers of a hot and a cold tissue phantom for transmission experiments with variable ablation zone radii for mimicking MWA experiments with high power microwave [66].

The microwave transmission through cylindrical hot and cold liver phantoms is simulated in the CST studio suite with two materials defined with the dielectric properties of cold liver phantom (TX-100 30%) and hot liver phantom (TX-100 70%), in a parallel work [66]. The simulation model is comprised of the microwave applicator dipped in a cylindrical compartment containing the hot liver phantom and the BMA is dipped in the surrounding cylindrical compartment filled with the cold liver phantom. The simulation model has four positions for the dipped bowtie-slot BMA in the cold liver phantom and the radius of the ablation zone or hot tissue ( $r$ ) is varied from 27.5 mm to 47.5 mm as shown in figure 6.22. The simulation model corresponds to the experimental setup shown in figure 5.15.

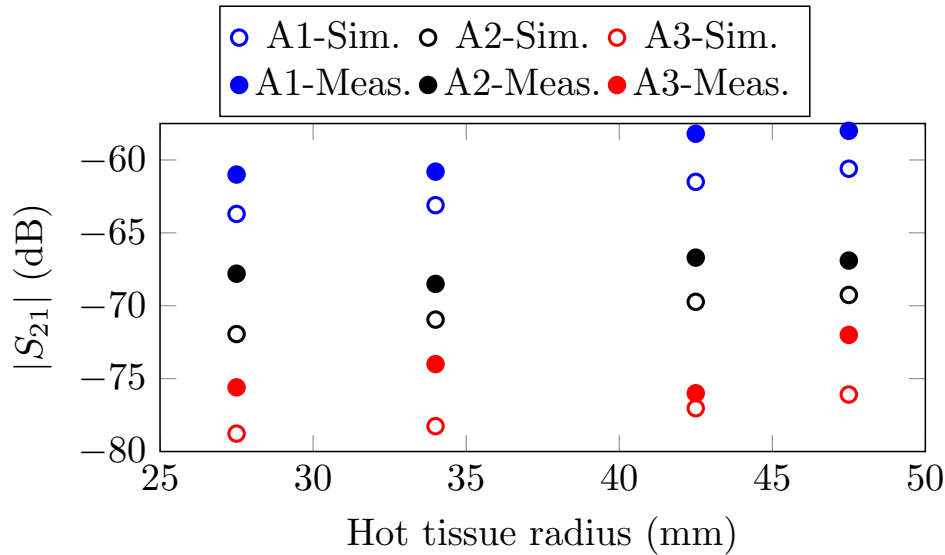


Figure 6.23: Variation in simulated and measured  $|S_{21}|$  values for different fixed distances between microwave applicator and BMAs dipped in hot and cold tissue phantoms in cylindrical compartments with increasing radius of hot tissue compartment.

The simulated and measured results for an increasing hot tissue radius for the different distances between the applicator and the BMA for cylindrical setup are shown in figure 6.23. The antenna position A1 has a distance ( $d_1$ ) of 6.14 cm from the applicator is the closest of all four positions and the antenna position A3 has a distance ( $d_3$ ) of 8.21 cm from the applicator which is the farthest of all the positions. Position A4 is omitted for the sake of clarity because it has a similar distance as compared to position

A1 and also a similar looking angle of the BMA to the center of the applicator slot as also in position A1. The simulated values of the transmission coefficient ( $S_{21}$ ) show an increase of the values at position A1-Sim (from -63.7 dB to -60.6 dB) and position A3 (from -78.8 dB to -76.1 dB) as the hot tissue radius increase from 2.75 cm to 4.75 cm. The measured values also show an overall increasing trend with an increase in the radius of the hot tissue commensurate with the simulation values similar to the calculated and measured transmission values as shown in figure 6.21.

#### 6.4 Microwave ablation in sweet potatoes

---

The MWA experiments with sweet potatoes involve microwave power of 50-80 W for different durations of time. First of all, the S parameters of commercial & self-developed microwave applicators and surface BMA are measured in sweet potato as shown in figure 6.24. The reflection loss of the self-developed applicator ( $S_{11}$ ) was measured to be -29.2 dB, which is lower than that of the commercial applicator at -14.1 dB. The reflection loss of the BMA ( $S_{22}$ ) was -19.7 dB, which is below the -10 dB threshold. The power received at the BMA ( $S_{21}$ ) was -39.1 dB for the self-developed applicator and -43.2 dB for the commercial applicator.

The reflected power for a 10-minute MWA experiment conducted using two applicators at 80 W for 2.45 GHz is shown in figure 6.25. During the first five minutes, both the self-developed and commercial applicators show a constant reflected power of 4.905 W and 1.115 W, respectively. The reflected power of the self-developed applicator is higher than that of the commercial applicator, and both show a similar increase in reflected power over time, which can be attributed to the progressive ablation process causing mismatch in the applicator. Figure 6.31 shows a photo of a cut-open sweet potato, which reveals that the application of high power (80 W) causes a burn hole to form immediately around the applicator. The reflected power of the self-developed applicator at 50 W power is shown in figure 6.25, where both a good and a poor example of applicator matching is shown. There is a measurement error of  $\pm 0.074$  W in all experiments due to the sensitivity of the HPS.

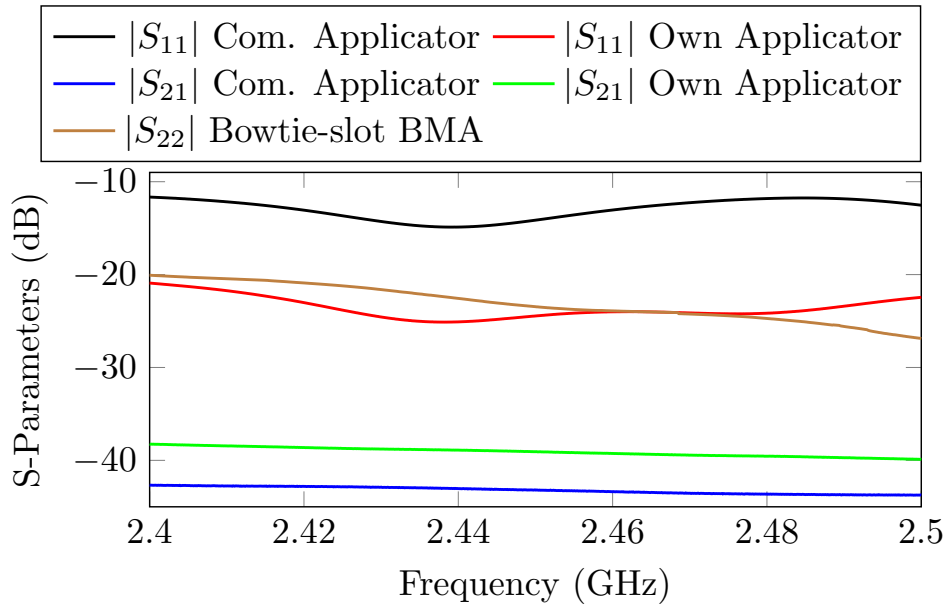


Figure 6.24: S-paramters measurement of self-developed microwave applicator, commercial applicator, and BMA in SP.

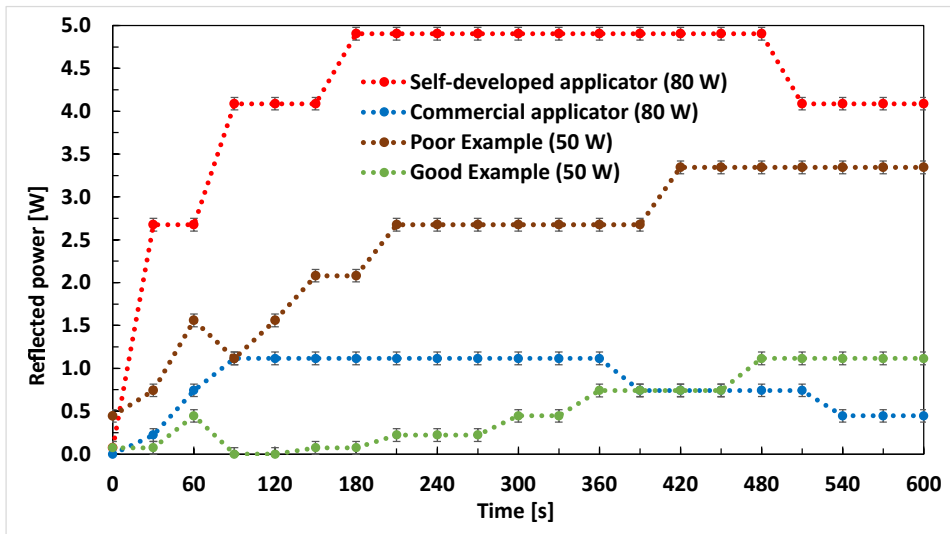


Figure 6.25: Comparison of reflected powers of commercial and self-developed applicators for 80 W MWA and poor and good examples of self-developed applicator matching for 50 W MWA in SP

After testing and calibrating of the MWA equipment, the reflected power of the self-developed applicator and the received power of the bowtie-slot

surface BMA during the MWA in sweet potato, increase in the ablation zone (short-axis diameter) with increasing ablation time, and the received power at the surface BMA versus increasing ablation temperature are presented in this section.

The experiment to measure the received and reflected power during MWA at 50 W for 600 seconds was conducted on sweet potatoes and the results are presented in figure 6.26. The measurements were taken several times with different levels of microwave power coupling, but the results shown here are from the most consistent and stable environment on a single day. In the first measurement (blue curve), the received power decreases from 30.9 mW to 29 mW in the first minute, then rises to 32.4 mW after 30 more seconds, before gradually dropping to 21.3 mW over the next 510 seconds. The reflected power in the first measurement increases from 0.1 W to 0.4 W in the first minute, and then reaches a maximum value of 2.1 W after fluctuating for a short period. In the second measurement (red curve), the received power starts at 16.3 mW and drops to 12.8 mW in the first 60 seconds, then increases to 16.4 mW before steadily decreasing to 9.8 mW over the next 540 seconds. The reflected power in this measurement also increases from 0.1 W to 0.7 W in the first 60 seconds, then fluctuates before increasing linearly to 2.1 W till the end of the measurement at 600 seconds.

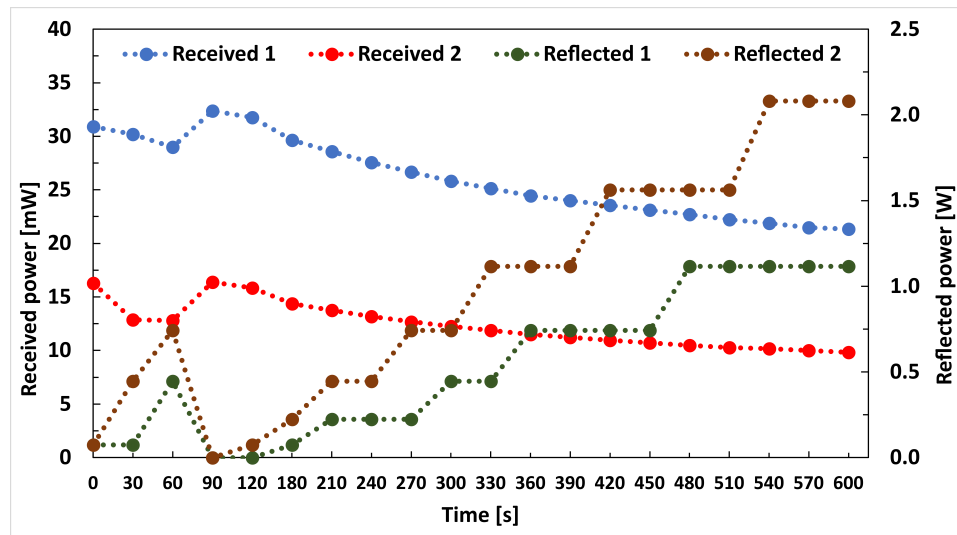


Figure 6.26: Received and reflected power vs. time for 50 W MWA in SP.



The relationship between the  $S_{11}$  (reflection loss) and time during MWA is shown in figure 6.27 for experiments at 50 W and 40 W in SP and 25 W and 40 W in bovine liver. The results indicate that the  $S_{11}$  value of the SP changes over time in response to the MWA. The blue curve shows the  $S_{11}$  value for the 50 W experiment, which starts at -28.3 dB and increases to -19.2 dB in the first minute. After 90 seconds, it drops to -39.8 dB, and then gradually increases to -15 dB at the end of the experiment at 600 seconds. The green curve represents the  $S_{11}$  value for a 25 W MWA experiment in bovine liver reported in [36], and it is similar to the  $S_{11}$  value at the end of the 50 W experiment in SP. The red curve shows the  $S_{11}$  value for the 40 W experiment in SP, which starts at -17.3 dB and increases to -14.1 dB after 180 seconds. The black curve represents the  $S_{11}$  value for a 40 W MWA experiment in bovine liver reported in [36], and it is comparable to the  $S_{11}$  value of the 40 W experiment in SP.

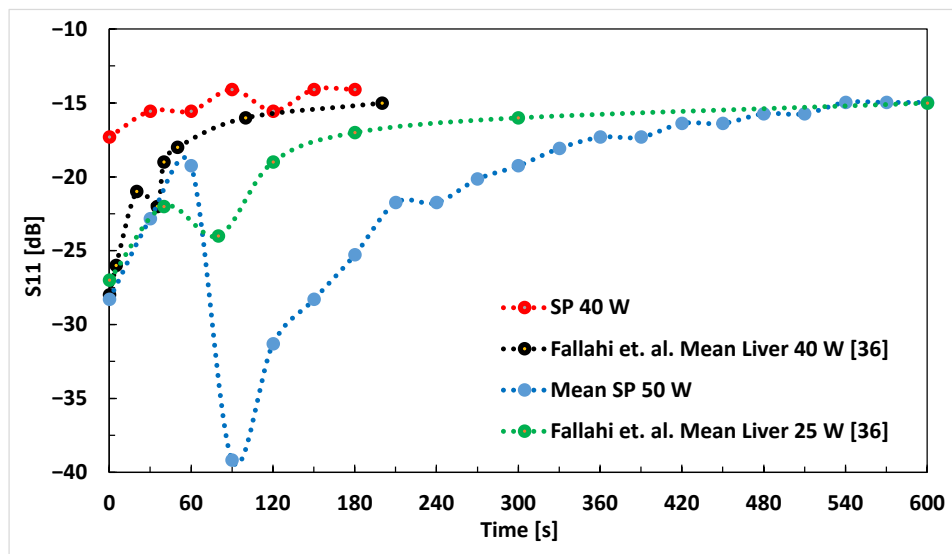


Figure 6.27:  $S_{11}$  as a function of time for 25 W, 40 W, and 50 W MWA experiments.

The figure 6.28 displays the size of the ablation zone SAD in SP as a function of time, under two microwave powers of 50 and 80 W at 2.45 GHz. The ablation zone appears elliptical with a short axis perpendicular to the microwave applicator. The results are also compared with a similar MWA experiment conducted on ex-vivo bovine liver, as reported in [35]. The measurement values (represented by green dots) are taken from figure 10 in [35] where the experiment was conducted at 30 W power. After each

experiment, the SP is cut open at the site of applicator puncture, and the perpendicular MWA SAD to the applicator channel is measured with an error of  $\pm 0.1$  cm. The SAD of the ablation zone for 50 W ranges from 0.6 to 3.3 cm, while for 80 W it ranges from 1.5 to 4.5 cm.

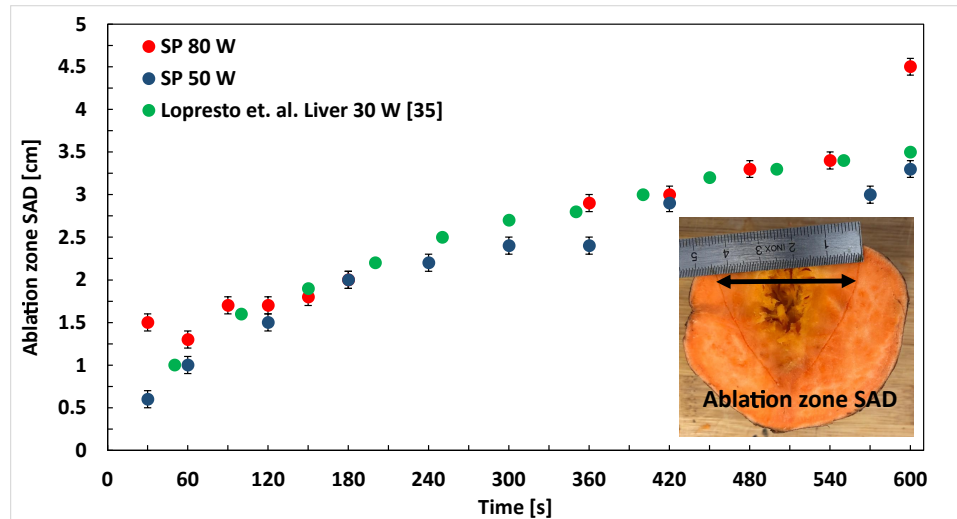


Figure 6.28: Ablation zone SAD as a function of time for 50 W & 80 W in SP & liver.

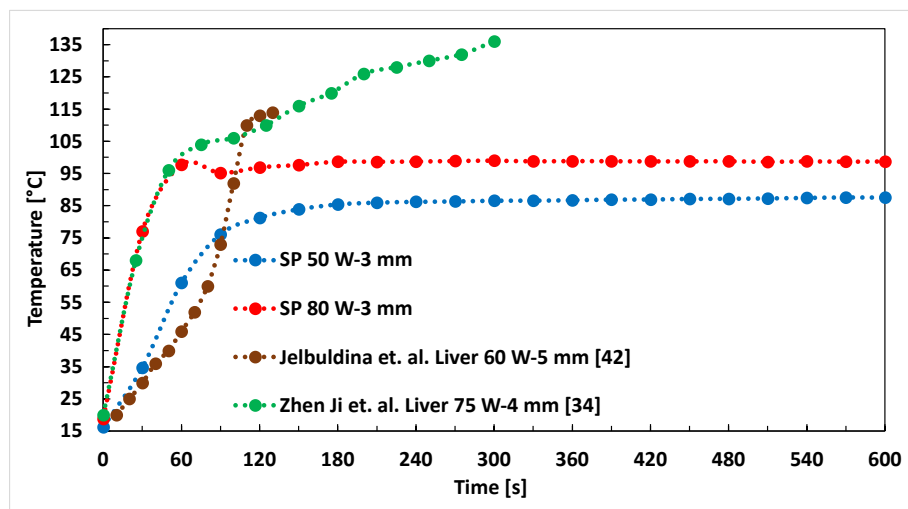


Figure 6.29: Temperature vs. time in MWA experiments.

Figure 6.29 shows the temperature of the SP during the MWA experiment for powers of 50 W and 80 W at 2.45 GHz. The temperature is measured with a sensor with a tip located 3-4 mm from the microwave applicator

slot, as depicted in the inset of the figure. The temperature measurement results for the SP MWA experiment are compared with results from ex-vivo MWA experiments on bovine liver (60 W, 130 s) reported in [42] and porcine liver (75 W, 300 s) reported in [34]. The temperature measurement values in the brown curve are taken from figure 6 in [42] and correspond to curve 'FBG 2.2' for 5 mm. The temperature measurement values in the green curve are taken from figure 10c in [34] and correspond to curve 'A' for 4 mm.

For the 50 W SP MWA experiment, as indicated by the blue curve, the starting temperature increases from 16.2 °C to 85.4 °C after 180 s and remains constant until the end of the measurement. The temperature values of the 60 W ex-vivo MWA on the bovine liver, as indicated by the brown curve, are comparable at 90 °C, after which the temperature continues to increase to 114 °C at 130 s. Similarly, for the 80 W SP MWA experiment, as indicated by the red curve, the starting temperature increases from 18.9 °C to 98.7 °C after 180 s and remains constant until the end of the measurement. The temperature values of the 75 W ex-vivo MWA on the porcine liver, as indicated by the green curve, are comparable at 60 °C, after which the temperature continues to increase to 136 °C at 300 s.

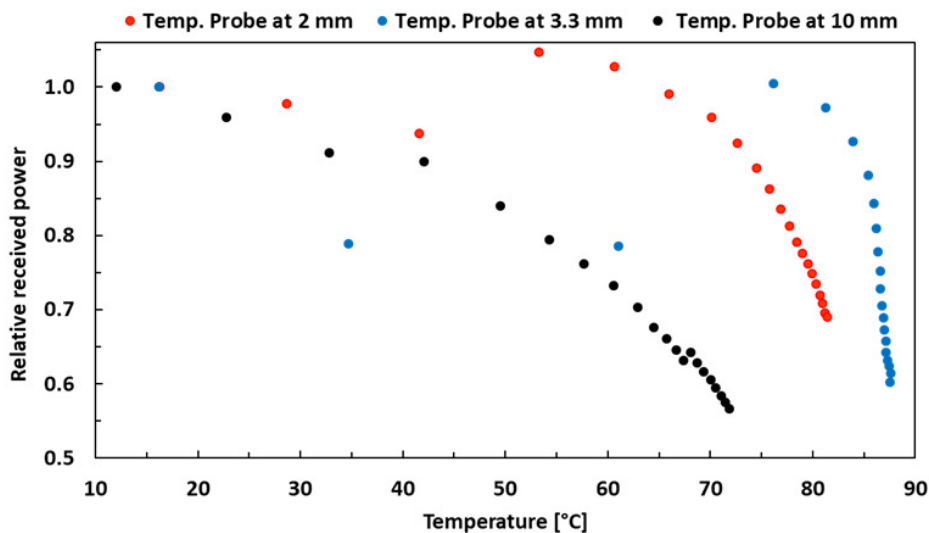


Figure 6.30: Relative received power vs. temperature for 50 W MWA in SP.

Figure 6.30 displays the relationship between the relative received power and temperature inside the SP for the 50 W MWA experiment. The relative received power is calculated as a ratio of the initial received power at time  $t = 0$  seconds. The figure includes three measurements taken at different distances from the center of the ablation zone, with temperature probes located 2 mm, 3.3 mm, and 10 mm away from the center. In all three measurements, it is observed that after a certain temperature, the relative received power starts to decrease as the temperature increases. The measurement taken with a temperature probe 3.3 mm away from the center (represented by blue dots) shows that the relative received power drops from 1 at 76°C to 0.6 at 88°C, representing a 40 % change. This correlation between an increase in temperature and a decrease in received power suggests that the material properties become more varied with increasing temperature, leading to increased losses in the SP due to heating. Finally, Figure 6.31 showcases some examples of the MWA performed on the SP at different power levels and times.

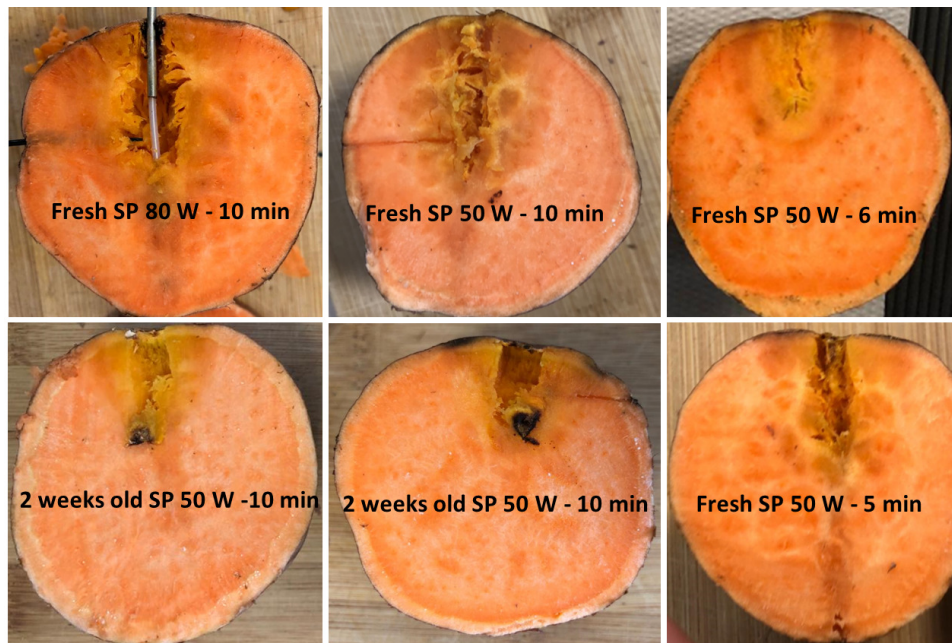


Figure 6.31: MWA in SPs for different times and powers.

## 6.5 Ex-vivo microwave ablation in animal liver

Ex-vivo MWA simulations and experiments are performed in the animal liver with 50 W at 2.45 GHz for a maximum of 10 minutes (600 s) time. The change in dielectric properties of the liver is measured during and after the MWA corresponding to the temperature dispersive dielectric properties defined in the EM-simulation, the SAD and the LAD of the ablation zone are measured and compared to the thermal simulation values, and the changes in S-parameters during MWA simulations and experiments are noted. The rise of temperature at different points from the center of the ablation zone is measured during MWA and finally, the changes in calculated relative received power are presented during MWA.

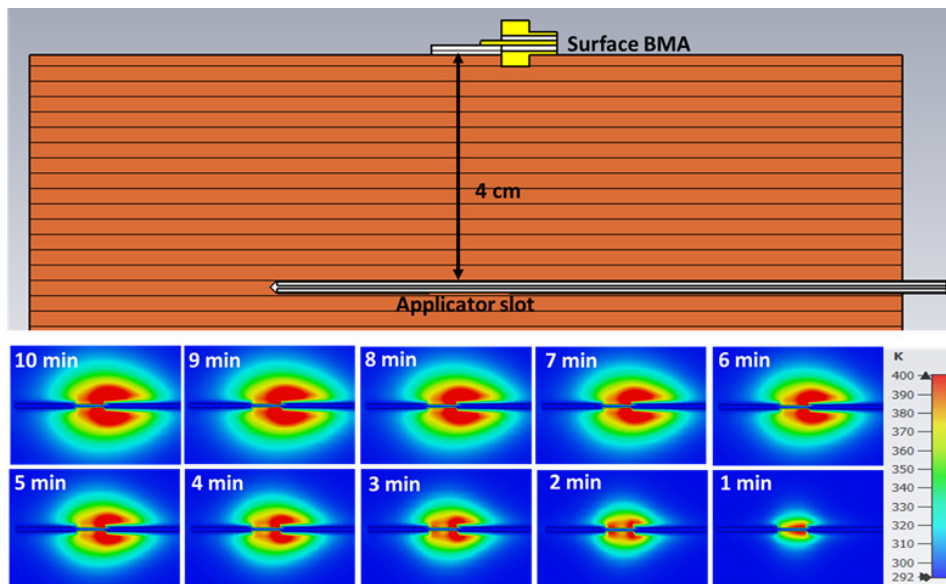


Figure 6.32: EM-thermal co-simulation model of a surface BMA and microwave applicator at a distance of 4 cm from each other and temperature profiles for 10 minutes ablation with 50 W microwave power at 2.45 GHz.

EM-thermal simulations of MWA in the ex-vivo liver are performed in the CST Studio suite with a time domain EM solver and thermal solver with open boundary conditions. Firstly, the temperature profiles in the liver are created in CST's thermal solver for all minutes during the 10 minutes MWA with 50 W power excitation at 2.45 GHz. The thermal conductivity of liver is set to  $0.469 \text{ W.m}^{-1}.\text{K}^{-1}$ . and specific heat of  $3600 \text{ J.kg}^{-1}.\text{K}^{-1}$ .

The blood-flow coefficient and Basal metabolic rate are ignored due to ex-vivo experiments. The material of the microwave applicator is changed from copper to a perfect electric conductor (PEC) to avoid heating due to conductive effects. The simulation model and temperature profiles for all 10 minutes are shown in figure 6.32. The temperature dispersive dielectric properties of the liver at 2.45 GHz as given in [36] are defined in the EM-simulation as shown in figure 6.33. Thereafter, for every temperature profile, the reflection loss of the microwave applicator ( $|S_{11}|$ ) and the transmission of EM wave from the microwave applicator to the surface BMA ( $|S_{21}|$ ) is simulated. The distance between the applicator and BMA is 4 cm.

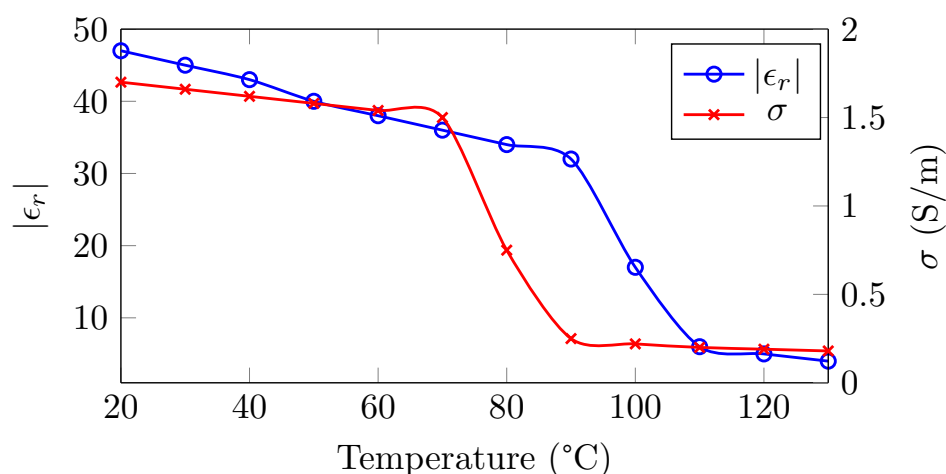


Figure 6.33: The temperature dispersive dielectric properties of bovine liver defined in the EM-simulation as given in [36].

First of all, the change in dielectric properties of the liver at 2.45 GHz during and after MWA is shown in figure 6.34. For the first 10 minutes of MWA the value of permittivity ( $|\epsilon_r|$ ) drops from 47.3 to 2.62 and the value of electrical conductivity ( $\sigma$ ) drops from 1.8 S/m to 0.12 S/m. Then the liver is let for cooling for 15 minutes, the value of permittivity ( $|\epsilon_r|$ ) increases from 2.62 to 7.81 and the value of electrical conductivity ( $\sigma$ ) increases from 0.12 S/m to 0.46 S/m.

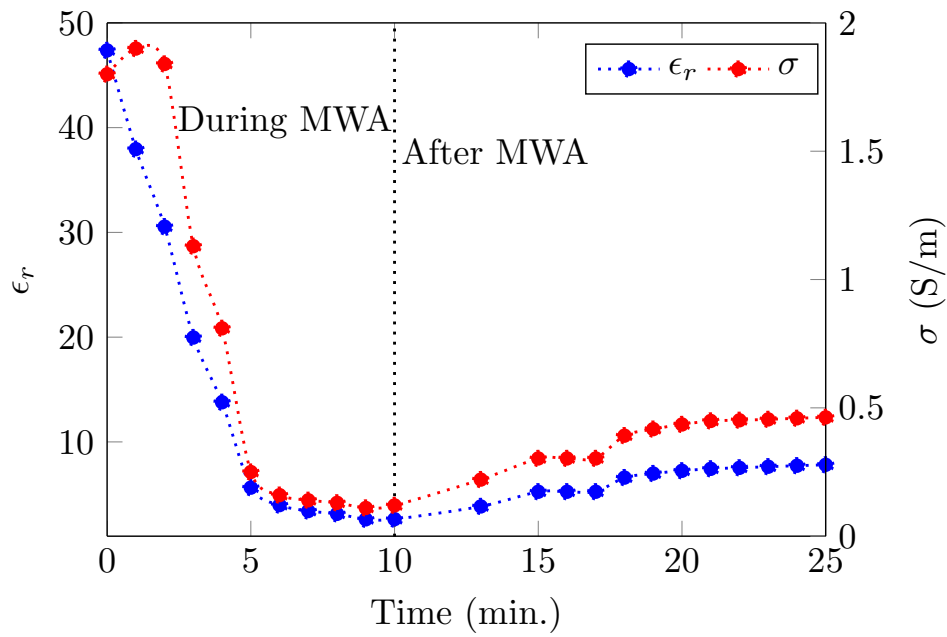


Figure 6.34: Measured dielectric properties of bovine liver during and after ablation with 50 W switching microwave power at 2.45 GHz.

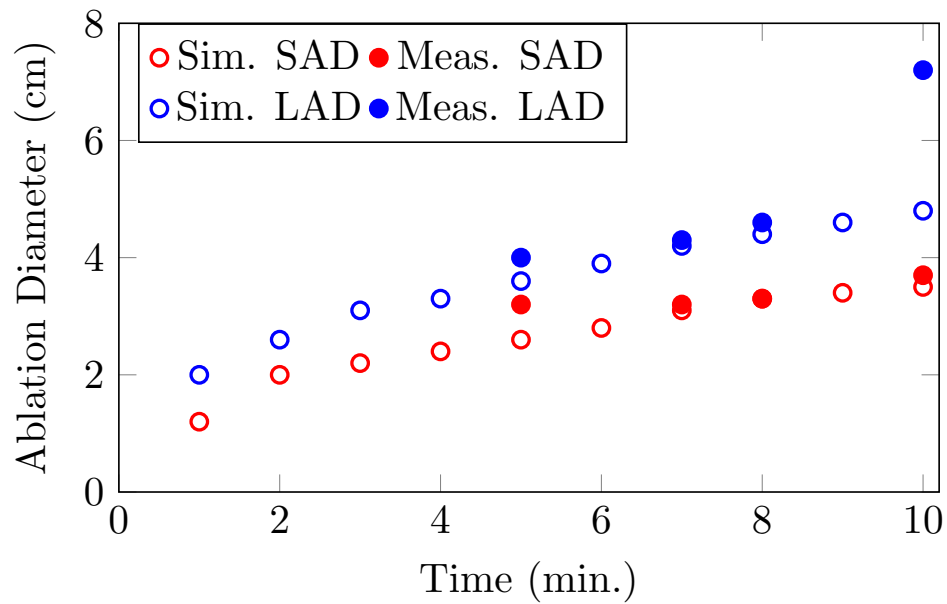


Figure 6.35: Simulated and Measured SADs and LADs for 50 W power at various time instants during MWA in the ex-vivo liver.

The ablation zone diameters (SAD, LAD) are measured after 5, 7, 8, and 10 minutes of MWA. At these chosen time instants there are no blood vessels involved during MWA which could hamper the ablation zone diameters. The SAD of the ablation zone is recorded as 3.7 cm as compared to the EM-thermal simulation value of 3.5 cm and similarly, the LAD of the ablation zone is recorded as 7.2 cm as compared to the simulation value of 4.8 cm after 10 minutes of MWA. The difference in measured and simulated LAD values after 10 minutes of MWA could be due to burning along the shaft of the microwave applicator due to conductive effects. The results of measured SAD and LAD are compared with the corresponding simulation values of the thermal simulation with 50 W power as shown in figure 6.35. A temperature value of 60 °C is taken as the lower criteria for estimating the damage zone for measuring ablation zones (SAD, LAD) in the thermal simulation results as shown in figure 6.32. The ablation zones produced for 5, 7, 8, and 10 minutes of MWA in the ex-vivo liver with 50 W power at 2.45 GHz are shown in figure 6.36.

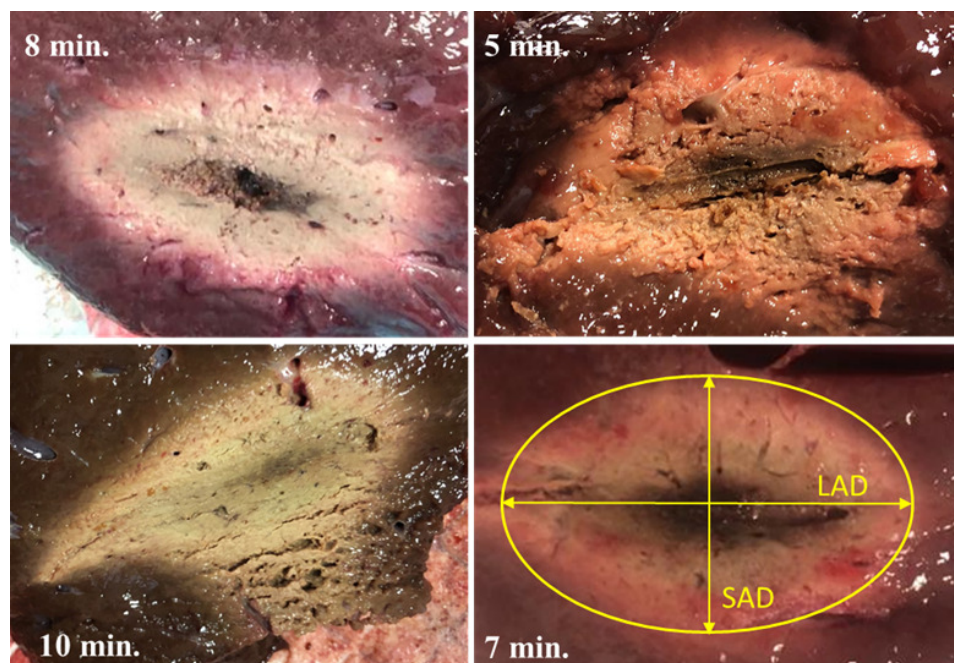


Figure 6.36: Ablation zones produced after 5,7,8 and 10 minutes MWA of the ex-vivo liver.



The power received by surface BMA and power reflected from the microwave applicator is recorded every 30 seconds during 10 minutes MWA of the ex-vivo liver. The absolute received and reflected measured power values are normalized on a logarithmic scale with reference to 50 W power excited and herein called  $|S_{11}|$  and  $|S_{21}|$  respectively. The measured and simulated S parameters at 2.45 GHz during 10 minutes MWA is shown in figure 6.37. The magnitude of S parameters measured before and af-

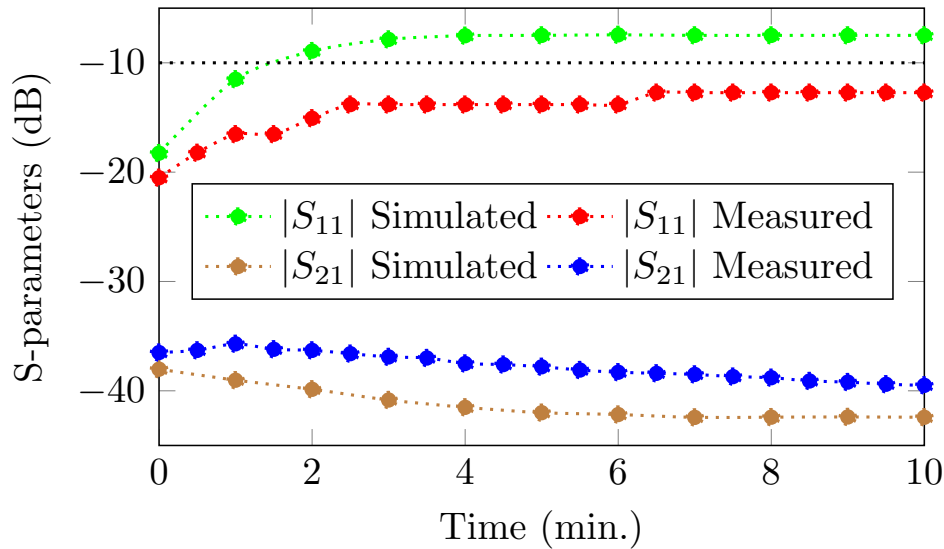


Figure 6.37: EM-thermal co-simulation and measured ex-vivo liver MWA results: scaled magnitude of reflection loss of microwave applicator ( $|S_{11}|$ ) and scaled magnitude of power received by BMA ( $|S_{21}|$ ) during MWA.

ter MWA are omitted for the sake of clarity. The measured magnitude of  $S_{11}$  value is -20.5 dB as compared to -18.26 dB simulated value in the beginning at time ( $t = 0s$ ). As the MWA progresses, the matching of the microwave applicator to the liver tissue deteriorates both in simulation and measurement, the simulated  $S_{11}$  magnitude value rises to -7.49 dB after 5 minutes and almost stays constant till the end of MWA at 10 minutes. On the other hand, the measured  $S_{11}$  values rise to -12.73 dB at 6.5 minutes into the MWA and then stay constant till the end. Conversely, the magnitude of  $S_{21}$  linearly drops as compared to the initially recorded value both in simulation and measurement. The measured magnitude of  $S_{21}$  value is -36.5 dB as compared to -38.02 dB simulated value in the beginning at time ( $t = 0s$ ). The simulated magnitude of  $S_{21}$  gradually decreases during

MWA until it reaches -42.42 dB at the end of MWA, thereby representing a change of 4.4 dB as compared to the start of MWA. On the other hand, the measured magnitude of  $S_{21}$  values briefly rises in the first minute of ablation to -35.7 dB and thereafter it linearly drops similarly to the simulated value to -39.4 dB at the end of 10 minutes of MWA, thereby representing a change of 3 dB during the MWA.

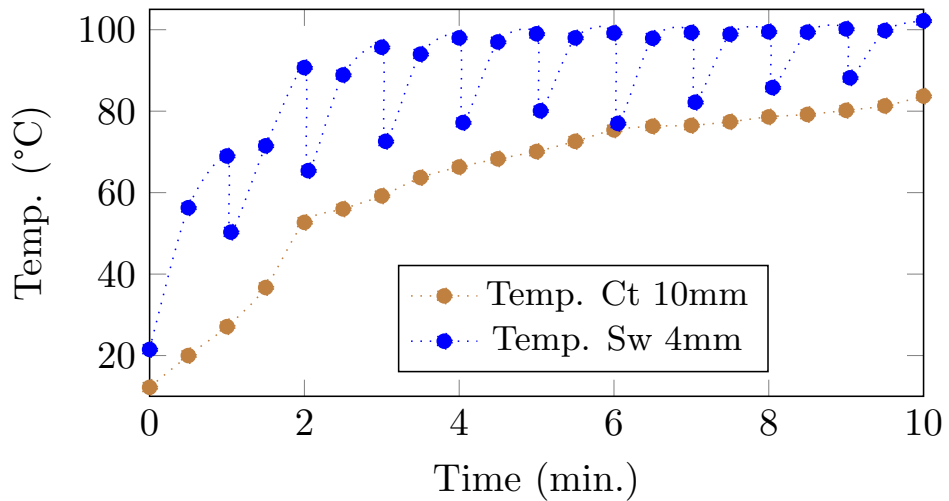


Figure 6.38: Temperature rise during MWA in the ablation zone in the ex-vivo liver with 50 W continuous and switching powers.

The temperature is measured during MWA in the ablation zone, temperature-time measurement is shown in figure 6.38. The temperature is measured 1 cm away from the ablation zone center with continuous power (Ct) and with switching power (Sw) at 4 mm away from the center of the ablation zone. The temperature rises to 83.7 °C at 10 mm away from the ablation zone with 50 W continuous power at 2.45 GHz and it rises to 102.2 °C at 4 mm away from the center of the ablation zone for 50 W switching power after 10 minutes of ablation.

Relative change in received power to initially received power is shown in figure 6.39. Results for two types of experiments are presented: one with the continuous (Ct) 50 W power and the other with the switching (Sw) 50 W power. As previously explained, Sw power is used because HPS is switched off every minute to record the properties of the liver during ex-vivo MWA. As also observed in figure 6.37, the relative received power in both cases decreases with the increase in temperature and growing SAD. With Ct power,

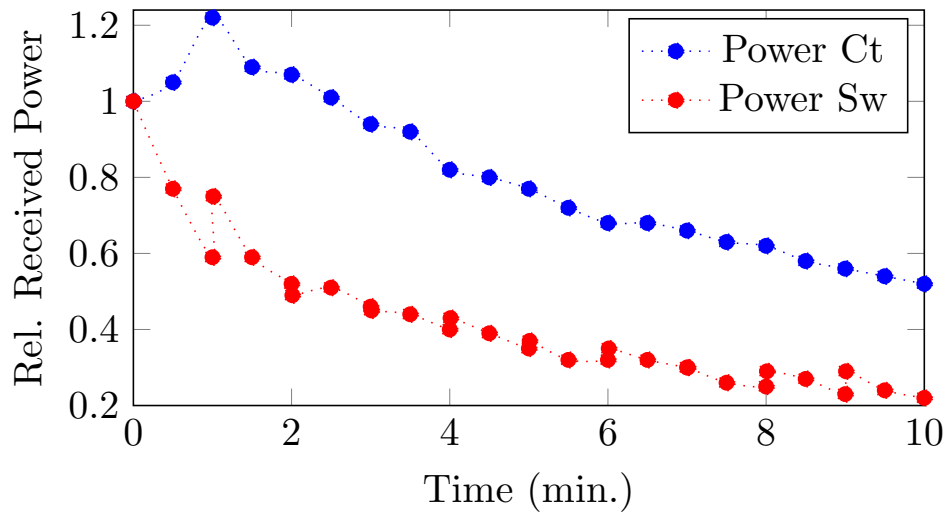


Figure 6.39: Relative received power to initially received power for continuous and switched transmit power during MWA in the ex-vivo liver.

the relative received power briefly increases to 1.22 and then linearly decreases to a factor of 0.52 (almost half) to the initially received power. In the case of Sw power, there is a gradual decrease of power with a stepped increase in power at the time instant where the power is switched. At the end of ablation with Sw power, the relative received power decreases to a factor of 0.22 (almost 1/5) to the initially received power.



# 7

## Summary and Outlook

In this chapter, the discussion of all the simulation and measured results is done. Subsequently, the results are summarized and compared to each other and to the state of the art. Finally, a conclusion and the outlook is given.

### 7.1 Discussion

---

The discussion is focused on the results of microwave applicator and BMAs, experiments with liver phantoms, MWA monitoring in sweet potatoes and animal liver.

#### 7.1.1 Microwave applicator

The design of a single-slot microwave applicator is suitable to excite up to 80 W power for MWA at 2.45 GHz. The applicator is well-matched to number of materials under test like: water, human skin, liver phantoms, sweet potatoes and animal liver as shown in figures [6.3, 6.24, 6.25, 6.27, 6.37] under room temperature. With the progress of MWA, the reflection loss of the microwave applicator inside the hot sweet potato and hot animal liver changes. The  $|S_{11}|$  of microwave applicator in SP as shown in figure 6.27 and  $|S_{11}|$  of microwave applicator in the animal liver as shown in figure 6.37 during MWA can be compared. It is observed that the  $|S_{11}|$  rises with the passage of ablation time; this is due to the change in dielectric properties of sweet potato and animal liver with rising temperature as shown in figures [6.34, 5.6].

The simulated  $|S_{11}|$  in animal liver rise from an initial value of -18.3 dB to -7.49 dB after 5 minutes, this magnitude remains constant till the end of

MWA. The rise in simulated  $|S_{11}|$  above the -10 dB threshold line for reflection loss of the microwave applicator is comparable to the rise of measured  $|S_{11}|$  above -10 dB during MWA with 40 W power at 2.45 GHz for 10 minutes as shown in the figure. 7 of [36]. The measured  $|S_{11}|$  in the animal liver rises to -12.7 dB from an initial value of -20.5 dB in the animal liver after 10 min. MWA as compared to -15 dB in SP after 10 min MWA from an initial value of -28 dB. The magnitude of  $S_{11}$  in SP is smaller as compared to the animal liver after 10 minutes of MWA; this is because the dielectric properties of SP do not change as much as the dielectric properties of animal liver during MWA. This could be associated with the seeping of water in the ablation zone during MWA.

### 7.1.2 Body-matched antennas

The body-matched antennas (BMAs) are designed to match to the animal liver and sweet potato surfaces and for matching with the PVP and the TX-100-based liver phantoms when dipped inside these phantoms. The design frequency is 2.45 GHz at which the MWA is carried out which is the reason that a smaller size bowtie-slot antenna is preferred as compared to a larger UWB variant of the bowtie-slot antenna.

The bowtie-slot antenna is fed from the side using the CPW technique with the help of an edge launch SMA connector and CPA is probe fed from the ground plane at the back of the antenna with a probe-fed SMA connector. The CPW feed of the dipped version of the bowtie-slot antenna is changed as compared to the surface version as shown in figure 6.10. This is due to the fact that there is a dielectric layer of liver phantom is formed over the antenna surface resulting into a stripline configuration as opposed to a stripline configuration of antenna feed in surface bowtie-slot antenna. This results in changing the input impedance of the antenna; therefore, the dimensions of the CPW feed, shunt stub lengths and even the size of the slot is optimized to adjust to the stripline configuration. However, both the feeding techniques (CPW and probe feed) are equally suitable for the placement of the BMA on the animal liver surface and the sweet potato surface. To avoid an air-cushion between the surface of MUT and the BMA, some fixing arrangements like rubber bands or fixing brackets are used. As

shown in figure 6.9, an air gap or a fabric material between the BMA and the surface of MUT deteriorates the reflection loss of the BMA.

The circularly polarized CPA is better suited for MWA monitoring as it provides the freedom of placement of the BMA on the surface of the MUT regardless of the orientation of the microwave applicator inserted in the MUT as observed in the transmission experiments performed with 2 CPAs with SPs where the antennas are placed at  $0^\circ$  and then rotated  $90^\circ$  to each other as shown in figures [6.17, 6.18]. The use of matching medium in CPAs enhances the 3 dB axial ratio beam-width as shown in the simulation result (figure 6.19). This means that the CPA can also be placed at  $\pm 3^\circ$  elevation angles around the top of the applicator slot at the surface of MUT.

### 7.1.3 Transmission through liver phantoms

The mathematical model presented in chapter 4, is used to calculate the transmission between the BMA and the microwave applicator in a two-layer hot and cold liver model. The calculated results are plotted with the transmission experiments carried out with a planar two-layer liver phantom setup as shown in figure 6.21. It is observed that the mathematically calculated values of the transmission between the applicator and the antenna in a two-layer (hot and cold liver phantom) model increase with the increase in transmission distance (hot tissue radius) in the hot liver phantom. In an experiment with the planar two-layer liver phantom setup, the transmission increased with hot tissue radius for 4 cm and 5 cm distance between the applicator and the antenna but decreases for 3 cm distance. This is due to a reading of the transmission at a 2 cm hot tissue radius at a 3 cm overall distance. This particular reading could be regarded as a false result due to unknown factors. The increasing trend of transmission with increasing hot tissue radius is also confirmed by the simulation carried out in the CST studio suite with the simulation setup shown in figure 6.22 and the corresponding cylindrical experimental setup shown in figure 5.15. The measurements shown in figure 6.23, at the antenna position A1 with an overall distance of 6.14 cm, show a consistently increasing trend of transmission values with increasing hot tissue radius commensurate with the simulation values. At the position A2 (overall distance of 7.01

cm), the transmission measurements do not show a clear trend, the transmission value decreases at a hot tissue radius of 3.4 cm then increases at 4.25 cm, and then again decreases at 4.75 cm, showing an overall decrease in the transmission with an increase in the hot tissue radius from 2.75 cm to 4.75 cm. Lastly, at position A3 (overall distance of 8.21 cm), the transmission increases from -75.6 dB at 2.75 cm hot tissue radius to -72 dB at 4.75 cm hot tissue radius. Thus it can be concluded that the overall trend of transmission power with increasing hot tissue radius is also increasing in measurements except for a few measurements. The error in measurements at positions A2 and A3 could be associated with antenna sensitivity at a higher distance and placement angle compared to the microwave applicator.

#### 7.1.4 MWA monitoring in sweet potatoes

In the MWA experiments on sweet potato, two microwave powers of 50 W and 80 W were used. The results showed that using a power of 80 W resulted in burning of the tissue as seen in the figure 6.31. To avoid burning effects and to adhere to the maximum power rating of the applicator, powers above 80 W were not used. The results of the 50 W and 80 W MWA experiments were compared in terms of maximum and minimum received powers, reflected powers, ablation zone sizes, time-dependent temperatures, and temperature-dependent received powers. The results showed that for 80 W MWA, the maximum reflected power, minimum received power, ablation zone size, and temperature were all higher compared to the 50 W MWA. A summary of all quantitative results of MWA in sweet potato for different time and temperature settings for the 50 W and 80 W experiments can be found in table 7.1.

Table 7.1: Summary of all quantitative results for 50 W and 80 W MWA experiments with SP

Result	50 W (min.)	50 W (max.)	80 W (min.)	80 W (max.)
Reflected power	0 W	2.1 W	0 W	4.9 W
Received power	9.8 mW	32.4 mW	21.6 mW [[39]]	30.6 mW [[39]]
Ablation zone SAD	0.6 cm (30 s)	3.3 cm (600 s)	1.5 cm (30 s)	4.5 cm (600 s)
Temp. vs. time	16 °C (0 s)	88 °C (600 s)	19 °C (0 s)	99 °C (600 s)
Pr vs. temp.	9.82 mW (88 °C)	32.25 mW (53.5 °C)	-	-



The results obtained from the MWA experiments performed on SP are compared to those of ex-vivo MWA experiments performed on animal liver. The comparison of the values of the dielectric constant, electrical conductivity, reflected power, ablation zone SAD, and temperature as a function of time between SP and animal liver is presented in table 7.2. The comparison between the two materials supports the use of SP as an alternative tissue material for ex-vivo MWA experiments in the liver. The values of the dielectric constant ( $\epsilon_r$ ) and electrical conductivity ( $\sigma$ ) of SP and liver are comparable in the temperature range of 50-60 °C, as shown in table 2 and figure 5.6. However, as the temperature increases, the ex-vivo liver loses water rapidly, resulting in a sharp decrease in  $\epsilon_r$  and  $\sigma$ . In contrast, the water in SP accumulates with increasing temperature, causing  $\epsilon_r$  and  $\sigma$  to increase above their room temperature values.

Table 7.2: Comparison between SP and animal liver MWA

<b>Result</b>	<b>SP</b>	<b>Liver</b>
$\epsilon_r$	50.3 (63 °C)	40 (60 °C) [36]
$\sigma$ (S/m)	1.97 (51 °C)	1.75 (50 °C) [36]
Reflection loss	15 dB (50 W-600 s)	15 dB (25 W-600 s) [36]
Reflection loss	14 dB (40 W-180 s)	15 dB (40 W-210 s) [36]
Temperature	76.1 °C (50 W-90 s-3 mm)	73.0 °C (50 W-90 s- 5mm) [42]
Temperature	97.8 °C (80 W-60 s-3 mm )	100 °C (75 W-60 s- 4 mm) [34]
Ablation zone SAD	3.3 cm (50 W-600 s)	3.5 cm (30 W-600 s) [35]

The results of microwave ablation experiments on sweet potato (SP) were compared with those of animal liver, which is used as a tissue substitute in ex-vivo microwave ablation monitoring experiments. The comparison of various parameters such as dielectric constant, electrical conductivity, reflected power, ablation zone size and temperature as a function of time between SP and animal liver are shown in table 7.2. The results showed that the values of the dielectric constant and electrical conductivity of SP and animal liver are comparable in the 50-60 °C temperature range. However, as the temperature increases, animal liver loses water rapidly, causing the dielectric constant and electrical conductivity to decrease sharply. On the other hand, in SP, the water content accumulates with increasing temperature, resulting in an increase in the dielectric constant and electrical conductivity values above room temperature.

The reflection loss of the microwave applicators in both SP and animal liver demonstrates the efficient design of the applicator and its match with the material. The reflection loss values for SP and animal liver were almost equal, reflecting similar material characteristics as shown in table 5.1. Additionally, the temperature in SP and animal liver was found to be equal until a certain point, after which the temperature remained constant in SP, while it continued to increase in the ex-vivo microwave ablation of animal liver. This can be attributed to the rapid loss of water in ex-vivo microwave ablation of animal liver, compared to the slow loss of water in SP due to the skin and outer tissues that prevent water from escaping and the water evaporated by microwave ablation being replaced by water seeping in from the surrounding tissues.

The comparison of ablation zone size in table 7.2 also supports the suitability of SP as a tissue substitute. The ablation zone size was found to be slightly bigger with a 30 W microwave applicator in animal liver than with a 50 W microwave applicator in SP, due to the rapid loss of water in ex-vivo microwave ablation of animal liver. It can be concluded that SP can be used as a substitute material for ex-vivo microwave ablation monitoring experiments, offering similar results and a more realistic simulation of in-vivo microwave ablation.

As shown in figures [6.26, 6.30], the received power decreases with an increase in ablation time and temperature. When viewed in conjunction with the increasing ablation zone diameter shown in figures [6.28, 6.31], which increases with ablation time, it can be inferred that the relative received power compared to the initially received power decreases with growing ablation zone diameter and rising temperature. This is in contrast to the increasing trend observed in the transmission coefficient with increasing hot tissue radius of the liver phantoms. The reason behind this phenomenon is explained in the next section.

### **7.1.5 MWA monitoring in ex-vivo liver**

EM-thermal simulation is carried out in the CST studio suite to simulate MWA in the ex-vivo liver. The SADs of the ablation zones created with the 50 W power excited from the microwave applicator in the simulation tool are very close in value to the measured values of the SADs of the ablation

zones created with MWA in the ex-vivo liver. After 10 minutes of MWA in the ex-vivo liver with 50 W power at 2.45 GHz, the measured value of SAD is 3.7 cm as compared to the simulated value of 3.5 cm as shown in figure 6.35. A jump in the measured value of LAD (7.2 cm) after 10 minutes of MWA as compared to the simulated value of LAD (4.8 cm) could be due to the elimination of heat convection effects in the simulation due to the use of PEC material for microwave applicator. However, in practice heating along the shaft due to the higher skin temperature of the microwave applicator is a reported problem. Thus it can be concluded that the temperature profiles created in EM-thermal simulation are close to the real scenario.

The measurement of dielectric properties during MWA as shown in figure 6.34 provides useful information about the comparison of the MWA performed with the self-developed applicator in the ex-vivo liver in this work with state-of-the-art. In [36], the dielectric properties of ex-vivo liver change during MWA as shown in figure 5.4. The  $\epsilon_r$  is at 48 before the start of the ablation which drops to 2 at 130 °C which is achieved at the end of MWA. In this work, the initial value of  $\epsilon_r$  is 47.3 which drops to 2.62 at the end of 10 min MWA. Similarly,  $\epsilon$  in [36], decreases from 2.15 S/m to 0.1 S/m and in this work it drops from 1.8 S/m to 0.12 S/m. Thus the dispersion in dielectric properties of animal liver observed in this work is closely comparable with the most recent state-of-the-art [36]. Similarly, a little rise in the dielectric properties, after MWA in this work is similar to a slight rise of dielectric properties after MWA in figure 4. of [35].

In figure 6.37, it is observed again that the received power ( $S_{21}$ ) in MWA in the ex-vivo liver decreases both in simulation and measurement with increasing ablation time which is consistent with the decreasing trend of received power observed in MWA in SPs. For measuring the dielectric properties of the liver during MWA, the microwave power is switched off at every minute interval of MWA. This results in a slower rise of temperature in the ablation zone of the liver as shown in figure 6.38. However, the relative change in received power is 78 % which is greater with switching power as compared to 48 % change in relative received power with the continuous power as shown in figure 6.39. Thus, it could be concluded that the switching power is better suited for monitoring MWA in the ex-vivo liver.

## 7.2 Comparison

Two approaches are used to validate the transmission-based method for monitoring MWA in the liver. The first approach is from the standpoint of the theoretical model and the studies carried out on tissue phantoms and the second approach is using the EM-thermal co-simulation model of CST Studio Suite and comparing it with MWA in SPs and ex-vivo liver.

The absolute value of received power obtained from calculated results of the theoretical model, EM-thermal co-simulation, measurement with 2 layer liver phantom model, sweet potato experiments, and MWA in the ex-vivo liver are compared in table 7.3. All the results given are: for a distance of 4 cm between the applicator slot and antenna, with 50 W continuous power at 2.45 GHz for SAD between 3.3 cm to 4 cm.

Table 7.3: Comparison of results for 50 W - 2.45 GHz MWA experiments at 4 cm distance between the microwave applicator and the BMA.

<b>Results for 4 cm</b>	$ S_{21} $ (dB)	SAD (cm)
Theoretical model	-44.8	4
EM-thermal co-simulation	-42.2	3.5
Measured 2 layer phantom	-39.8	4
Measurement in sweet potato	-37.1	3.3
MWA ex-vivo liver	-39.5	3.7

As shown in the table 7.3, the calculated transmitted power from the theoretical model for two-layer tissue phantom is -44.8 dB and the measured result for two-layer tissue phantom is -39.8 dB showing a difference of 5 dB which can be attributed to the geometry factor of the antenna and difference in actual dielectric properties of tissue phantoms and the ones assumed in the theoretical model. Again from table 7.3, comparing the absolute value of received power between the EM-thermal simulation and MWA in the ex-vivo liver, there is a difference of 2.7 dB in received power which can again be attributed to the difference in temperature-dependent dielectric properties of the liver as in figure 6.33 and the temperature dispersive material properties measured during the MWA in the ex-vivo liver as shown in figure 6.34.

Now coming towards the relative change in received power in EM-thermal co-simulation and MWA in SPs and ex-vivo liver, the table 7.4 gives the

Table 7.4: Change in  $|S_{21}|$  and relative received power for 10 min. ablation with 50 W power and 4 cm distance between microwave applicator and BMA.

Value	$\Delta S_{21} $	$\Delta$ in relative received power
EM-thermal co-simulation	-4.4 dB	63.7 %
MWA in sweet potato	-1.82 dB	40% ([39])
MWA in ex-vivo liver	-3 dB	78% (Sw), 48% (Ct)

change in  $|S_{21}|$  and percentage change in relative received power to initially received power for EM-thermal co-simulation and MWA in SPs and ex-vivo liver. The overall change in  $|S_{21}|$  is -4.4 dB in EM-thermal co-simulation compared to -1.82 dB in MWA in SP and -3 dB in MWA in the ex-vivo liver with continuous power. In terms of percentage change in relative received power to initially received power, there is a 63.7 % decrease in EM-thermal co-simulation, 40 % in MWA in SPs, and 48% for MWA in the ex-vivo liver with continuous power and 78% with switching power for 10 minutes ablation time.

However, there is an increasing trend in received power with increasing hot tissue radius, in the case of two-layer theoretical and experimental models. Theoretically, there is an increase in  $|S_{21}|$  from -46.2 dB to -44.8 dB (38% increase) for a propagation distance of 4 cm when the radius of the hot tissue increases from 1 cm to 2 cm as shown in figure 6.21. Experimentally, the  $|S_{21}|$  increases from -44.3 dB to -39.8 dB (4.5 dB increase) for a propagation distance of 4 cm when the radius of the hot tissue increases from 1 cm to 2 cm as shown in figure 6.21.

There is an increasing trend in the received power with increasing hot tissue radius in the two-layer (hot and cold liver) theoretical model, EM simulations, and experiments. On the other hand, there is a decreasing trend of the received power with increasing ablation-time or SAD in EM-thermal co-simulations and MWA in SPs and ex-vivo liver. A possible explanation could be that in EM-thermal simulations and corresponding ex-vivo liver and sweet potato experiments more layers are formed with varying dielectric properties due to the gradual dissipation of heat produced by the microwave power. Thus, there are multiple transmission coefficients between the neighboring layers in the propagation path which causes the received power to decrease for a fixed transmission distance (R). Although the  $\sigma$  of the hotter tissue is lower than the colder tissues yet with the in-

crease in the size of the ablation zone, the received power decreases in ex-vivo MWA experiments. Conversely, in the two-layer theoretical model and two-layer liver phantom simulations and experiments, there is only a single transmission coefficient between the hot and cold liver. Therefore, the received power increases with the radius of hot tissue which has a lower  $\sigma$  value than the cold tissue.

However, in both cases, there is a change in received power observed with increasing hot tissue radius and increasing ablation time. This shows that the transmission-based method is effective in observing the changes in dielectric properties caused during the MWA and the extent of the change caused inside the liver tissue.

### 7.3 Conclusion

---

In this work, a transmission-based method is presented for MWA monitoring in the ex-vivo liver. The method is tested theoretically, in simulation, with phantom studies, in sweet potatoes, and with ex-vivo liver ablation. The theoretical and simulation results are comparable with the phantom studies, sweet potato, and ex-vivo liver ablation experiments. The contrast in the liver tissue properties and the stimulated power used for MWA is enough to produce a discernible signal change at the surface of the liver which can be measured and correlated with the ablation zone diameter. Hence, it can be concluded that the transmission-based method can be used for monitoring MWA. This is the first study to directly receive a signal from a microwave applicator during a MWA process with the help of a surface BMA. The main target application of this work is the development of an imaging system for temperature monitoring and microwave applicator guidance for MWA. The focus of this work is on measuring the magnitude of the received power during microwave ablation using surface body-matched antennas.

In a future work, a setup can be developed for monitoring phase of the received signal from the microwave applicator at the body surface during the MWA. An array of surface antennas can be used for receiving the signals from different angles from the center of the applicator's slot. The time-difference of arrival information can also be calculated from the phase variation of the received signal during the MWA. Hence, the

time-difference of arrival algorithm can be employed for estimation of the ablation zone using microwave imaging. Furthermore, the microwave applicator design could be improved by making it dual-mode i.e. using it not only for ablating the target tissue but also for measuring the properties of the target tissue before, during, and after the MWA. The test setups used in this work of MWA in the SP and the animal liver can also be used for testing new microwave applicator designs for better matching to the target tissue. Moreover, the BMAs can also be improved by designing them on flexible substrates which can be easily pasted on the patient's skin for an in-vivo studies. The design of BMAs can be altered to match with a stack up of muscle, fat, and skin layers added on the top of the liver. Other antenna designs like waveguide applicators and end-fire Vivaldi antennas can also be tried for performance comparisons with the broadside surface body matched antennas.

Finally, an in-vivo MWA monitoring could be performed with the system involving a dual-mode applicator, an array of flexible BMAs matched with the skin layer, and measurement setup for measuring both the magnitude, phase, and time-difference of arrival of the incoming signals from the microwave applicator at surface BMAs during the MWA. This can be coupled with an efficient microwave imaging algorithm for live reconstruction of the ablation zone during the MWA.







## Notations and Abbreviations

### Notations

---

Symbol	Meaning
$\epsilon_r$	relative dielectric constant
$\sigma$	electrical conductivity
$\tau$	Relaxation time
$\epsilon_0$	Permittivity of free space
$\omega$	Angular frequency
$\rho$	Density
$c$	Heat capacity
$k$	thermal conductivity
$Q$	Heat energy
$E$	Electric field
$G$	Geometry factor

---



---

**Abbreviations**

Abbreviation	Meaning
ISM	Industrial scientific and medical
EM	Electromagnetic
MR	Magnetic resonance
MRI	Magnetic resonance imaging
TBM	Transmission-based method
RF	Radio frequency
MWA	Microwave ablation
BMA	Body-matched antenna
HPS	High power RF source
MUT	Material under test
SP	Sweet potato
US	Ultra-sound
HIFU	High intensity focused ultra-sound
RFA	Radio frequency ablation
LA	Laser ablation
LITT	Laser induced thermal therapy
PVP	Polyvinylpyrrolidone
TX-100	Triton X-100
CT	Computed Tomography
PET	positron emission tomography
MR-RFA	Magnetic resonance mediated radio frequency ablation
PRF	Proton resonance frequency
UWB	Ultra wideband
MWI	Microwave imaging
SVD	Singular value decomposition
TDoA	Time difference of arrival
VNA	Voltage network analyzer
GUI	Graphical user interface
PCU	Power control unit
TDR	Time domain reflectivity
NaCl	Sodium chloride
BAN	Body area network
CP	Circularly polarized
CPA	Circularly polarized antenna or circular patch antenna
SAD	Short axis diameter
LAD	Long axis diameter
Sim.	Simulated
Meas.	Measured

---



# B

## List of Figures

1.1 The electromagnetic spectrum: separating ionizing & non-ionizing part of the spectrum and indicating the slot for radio & microwaves. Photo courtesy: Australian Radiation Protection and Nuclear Safety Agency. . . . .	1
3.1 Conceptual design approaches for non-invasive monitoring of thermal ablation inside a material under test (MUT). Concept-1: Monitoring changes in the reflection loss ( $\Delta S_{11}$ ) of surface BMA due to dispersion dielectric properties. Concept-2: Monitoring changes in the transmission coefficient ( $\Delta S_{21}$ ) on surface BMA during microwave ablation. Concept-3: Measuring changes in received power due to the brightness temperature of a broadband thermal noise source. . . . .	15
3.2 Conceptual design of the proposed transmission-based method for MWA monitoring. Body-matched antennas are placed on the patient's skin to measure the microwave power from the applicator inserted in the liver. . . . .	17
4.1 Dielectric properties measurement techniques [52]. . . . .	20
4.2 Illustration of the transmission-based theoretical model for microwave power traversing through two-layer model representing hot and cold liver tissues. . . . .	22
5.1 MWA monitoring experiment flowchart for transmission-based method. . . . .	25

5.2 High-power RF source by Kuhne Electronics: (a) Housing (b) Signal generator (c) Power supply. . . . .	26
5.3 High-power RF source by Kuhne Electronics: circuit diagram of the signal generator [55]. . . . .	27
5.4 Measured relative dielectric constant ( $\epsilon_r$ ) and electrical conductivity ( $\sigma$ ) of animal liver with respect to temperature at 2.45 GHz [36]. . . . .	29
5.5 Experimental setup for measuring temperature dispersive dielectric properties of a SP placed on a heating plate with a high-temperature dielectric probe [39]. . . . .	31
5.6 Change in dielectric constant and electrical conductivity of SP with the temperature at 2.45 GHz [39]. . . . .	33
5.7 High-temperature probe option 101 of N1501A dielectric probe kit: 1. High-temperature probe. 2. High temperature short. 3. Conductive disk. [59]. . . . .	34
5.8 Temperature dispersive dielectric constant and electrical conductivity of PVP-based liver phantom at 2.45 GHz. . . . .	34
5.9 Temperature dispersive dielectric constant and electrical conductivity of TX-100 phantom with 30 % concentration at 1.5 GHz. . . . .	35
5.10 Temperature dispersive dielectric constant and electrical conductivity of TX-100 phantom with 40 % concentration at 1.5 GHz. . . . .	36
5.11 Phantoms with 30 %, 50 %, 60 % and 70 % concentration of TX-100. . . . .	37
5.12 Drawing and contents of slim form probe 'option 102' of keysight N1501A dielectric probe kit: 6. Slim form probe. 7. Slim form short. 8. Slim form probe holder bracket. 9. O-rings 10. SMA adapter. [52]. . . . .	37

---

5.13 Planar phantom setup for two-layer hot and cold liver phantom transmission experiments: BMA & microwave applicator dipped in TX-100 30% (cold) and TX-100 70% (hot) tissue phantoms respectively at 3 cm, 4 cm and 5 cm fixed distances between the applicator and BMA [63]. . . . .	39
5.14 Planar phantom setup with a sliding mechanism for moving the applicator and BMA during the liver phantom transmission experiments [65]. . . . .	40
5.15 Cylindrical phantom experimental setup of two-layer hot and cold liver phantom for transmission experiments with variable hot tissue diameters ( $r$ ) and four fixed distances between the applicator and BMA [66]. . . . .	40
5.16 Elliptical cross-sectional phantom setup of two-layer hot and cold liver phantom for transmission experiments with variable hot tissue diameters ( $r$ ) and 6 fixed distances between the applicator and BMA [67]. . . . .	41
5.17 Experimental setup for MWA monitoring and temperature measurement during MWA in SP [39]. . . . .	42
5.18 Calibration of the test setup for measuring the network loss due to power cables [39]. . . . .	43
5.19 Testing of the experimental setup for MWA experiments in water as a medium [39]. . . . .	43
5.20 Block diagram of test setup inside and outside the anechoic chamber for: (i) Measuring dielectric properties of liver during MWA using slim-form probe. (ii) Measurement of temperature near ablation zone during MWA. (iii) Monitoring of received and reflected power during MWA in ex-vivo liver. . .	44
5.21 Preparation of the temperature sensor using the catheter as a guide for positioning in the liver tissue. a) Catheter tip is parallel to the applicator slot center. b) Measuring tip of the temperature sensor is parallel to the applicator slot center. C) Catheter rod for cleaning the guide. . . . .	45

5.22 Experimental setup corresponding to the block diagram shown in figure 5.20 for measuring of dielectric properties of liver, temperature near ablation zone, and monitoring received and reflected power during MWA in the ex-vivo liver in an anechoic chamber. . . . .	46
6.1 Microwave applicator initial design at 915 MHz and 4775 MHz. The simulation model and simulated reflection loss ( $S_{11}$ ) [51]. . . . .	48
6.2 Microwave applicator design at 2.45 GHz: the simulation and fabricated model. . . . .	49
6.3 Simulated and measured reflection loss of microwave applicator inserted in the liver. . . . .	50
6.4 Emprint microwave applicator from Medtronic: The water pipes are removed and an SMA connector is installed at the other end of the power cable. . . . .	51
6.5 Time-domain reflectivity (TDR) measurements before and after connecting the SMA connector on the other end of the power cable. The change in the reflection point shows it is near the tip of the commercial applicator. . . . .	51
6.6 Reflection loss of Emprint applicator in air, water, skin, and sweet potato. . . . .	52
6.7 Simulated and fabricated model of UWB Bowtie-slot BMA on the liver. . . . .	53
6.8 Measurement setup for reflection loss measurement of UWB Bowtie-slot BMA on PVP-based liver phantom. . . . .	53
6.9 Simulated and measured reflection loss of UWB bowtie-slot BMA on PVP-based liver phantom, hand-skin, and jeans. . . .	54
6.10 Simulated & fabricated models of bowtie-slot surface & dipped BMAs. . . . .	55
6.11 Simulated and measured reflection loss ( $ S_{22} $ ) of surface BMA on the liver and dipped BMA in 30% TX-100 solution. . . .	56



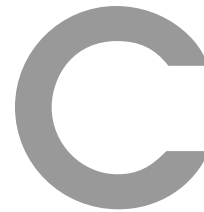
---

6.12 Design variables (shown in table 6.1), simulation models with & without MM, and boundary condition of circularly polarized CPA [83]. . . . .	58
6.13 Top and back view of the fabricated CPA designs with and without matching medium in comparison with 50 cents coin.	59
6.14 Test setups for measurement of reflection loss of the CPA with and without matching medium on sweet potato surface. . . .	60
6.15 Simulated and measured reflection loss of CPA with and without MM on liver and sweet potato surfaces. . . . .	60
6.16 Measurement setups for transmission coefficient of CPA . . . .	61
6.17 Measured $S_{21}$ of CPAs rotated at $0^\circ$ and $90^\circ$ to each other. . . .	62
6.18 Simulated axial ratio of CPA with and without MM. Measured AR of CPA inside and outside Anechoic chamber. . . . .	63
6.19 Simulated AR beam-width of the CPA at 2.45 GHz. . . . .	63
6.20 Simulated gain of CPA with MM at 2.45 GHz. . . . .	64
6.21 Variation in calculated and measured $ S_{21} $ values for different 3 cm, 4 cm, and 5 cm fixed distances between microwave applicator and BMAs dipped in hot and cold tissue phantoms in planar compartments with increasing transition distance ( $r$ ) through the hot tissue (hot tissue radius). . . . .	66
6.22 Simulation model of BMAs and microwave applicator dipped in two layers of a hot and a cold tissue phantom for transmission experiments with variable ablation zone radii for mimicking MWA experiments with high power microwave [66]. . . .	66
6.23 Variation in simulated and measured $ S_{21} $ values for different fixed distances between microwave applicator and BMAs dipped in hot and cold tissue phantoms in cylindrical compartments with increasing radius of hot tissue compartment.	67
6.24 S-paramters measurement of self-developed microwave applicator, commercial applicator, and BMA in SP. . . . .	69

6.25 Comparison of reflected powers of commercial and self-developed applicators for 80 W MWA and poor and good examples of self-developed applicator matching for 50 W MWA in SP . . . . .	69
6.26 Received and reflected power vs. time for 50 W MWA in SP. . .	70
6.27 $S_{11}$ as a function of time for 25 W, 40 W, and 50 W MWA experiments. . . . .	71
6.28 Ablation zone SAD as a function of time for 50 W & 80 W in SP & liver. . . . .	72
6.29 Temperature vs. time in MWA experiments. . . . .	72
6.30 Relative received power vs. temperature for 50 W MWA in SP.	73
6.31 MWA in SPs for different times and powers. . . . .	74
6.32 EM-thermal co-simulation model of a surface BMA and microwave applicator at a distance of 4 cm from each other and temperature profiles for 10 minutes ablation with 50 W microwave power at 2.45 GHz. . . . .	75
6.33 The temperature dispersive dielectric properties of bovine liver defined in the EM-simulation as given in [36]. . . . .	76
6.34 Measured dielectric properties of bovine liver during and after ablation with 50 W switching microwave power at 2.45 GHz.	77
6.35 Simulated and Measured SADs and LADs for 50 W power at various time instants during MWA in the ex-vivo liver. . . . .	77
6.36 Ablation zones produced after 5,7,8 and 10 minutes MWA of the ex-vivo liver. . . . .	78
6.37 EM-thermal co-simulation and measured ex-vivo liver MWA results: scaled magnitude of reflection loss of microwave applicator ( $ S_{11} $ ) and scaled magnitude of power received by BMA ( $ S_{21} $ ) during MWA. . . . .	79
6.38 Temperature rise during MWA in the ablation zone in the ex-vivo liver with 50 W continuous and switching powers. . . . .	80

6.39 Relative received power to initially received power for continuous and switched transmit power during MWA in the ex-vivo liver. . . . .	81
--	----





## List of Tables

5.1	Comparison of the physical properties at room temperature of the ex-vivo animal liver and sweet potato at 2.45 GHz [39].	31
5.2	Dielectric properties of sweet potato at 2.45 GHz in 20-75 °C temperature range [39]. . . . .	32
5.3	Recipe for salt, distilled water and TX-100-based liver phantoms at 1.5 GHz [62]. . . . .	35
5.4	TX-100 based liver phantoms for cold and hot liver at 2.45 GHz. [63] . . . . .	36
6.1	Dimensions of CPA with and without MM [83]. . . . .	57
6.2	Values used for the theoretical model for EM transmission from hot to cold liver at 2.45 GHz [54]. . . . .	65
7.1	Summary of all quantitative results for 50 W and 80 W MWA experiments with SP . . . . .	86
7.2	Comparison between SP and animal liver MWA . . . . .	87
7.3	Comparison of results for 50 W - 2.45 GHz MWA experiments at 4 cm distance between the microwave applicator and the BMA. . . . .	90
7.4	Change in $ S_{21} $ and relative received power for 10 min. ablation with 50 W power and 4 cm distance between microwave applicator and BMA. . . . .	91





## Bibliography

- [1] *Frequenzplan*. Postfach 8001, 53105 BONN: Bundesnetzagentur, 2019. [Online]. Available: <http://www.bundesnetzagentur.de/Frequenzplan>
- [2] A. Gartshore, M. Kidd, and L. T. Joshi, "Applications of microwave energy in medicine," *Biosensors*, vol. 11, no. 4, 2021.
- [3] A. Yezdani, K. Mahalakshmi, and K. Padmavathy, "Orthodontic instrument sterilization with microwave irradiation," *Journal of pharmacy & bioallied sciences*, vol. 7, no. Suppl 1, pp. S111–5, 2015.
- [4] A. Sahuquillo, R. Rubio, J.M. Ribó, E. Ros, and M. Vela, "Application of focused-microwave wet digestion to the determination of trace metals in human gallstones by icp/aes," *Journal of Trace Elements in Medicine and Biology*, vol. 14, no. 2, pp. 96–99, 2000. [Online]. Available: <https://www.sciencedirect.com/science/article/pii/S0946672X00800383>
- [5] T. M. Santaus, F. Zhang, S. Li, O. C. Stine, and C. D. Geddes, "Effects of lyse-it on endonuclease fragmentation, function and activity," *PloS one*, vol. 14, no. 9, p. e0223008, 2019.
- [6] M. Giersig, I. Firkowska, and J. Trosczynska, "Novel electroporation system for both gram-negative and gram-positive bacteria assisted by multi-walled carbon nanotubes," *MRS Online Proceedings Library 845*, no. 2, p. 145–150, 2004. [Online]. Available: <https://link.springer.com/article/10.1557%2FPROC-845-AA5.21>

- [7] M. H. H. Tehrani, M. Soltani, F. M. Kashkooli, and K. Raahemifar, "Use of microwave ablation for thermal treatment of solid tumors with different shapes and sizes—a computational approach," *PloS one*, vol. 15, no. 6, pp. 1–20, 2020.
- [8] Meghan G. Lubner, Christopher L. Brace, J. Louis Hinshaw, and Fred T. Lee, "Microwave tumor ablation: Mechanism of action, clinical results, and devices," *Journal of Vascular and Interventional Radiology*, vol. 21, no. 8, Supplement, pp. S192–S203, 2010. [Online]. Available: <https://www.sciencedirect.com/science/article/pii/S1051044310004112>
- [9] H. Bahramiabarghouei, E. Porter, A. Santorelli, B. Gosselin, M. Popović, and L. A. Rusch, "Flexible 16 antenna array for microwave breast cancer detection," *IEEE Transactions on Biomedical Engineering*, vol. 62, no. 10, pp. 2516–2525, Oct 2015.
- [10] E. Porter, H. Bahrami, A. Santorelli, B. Gosselin, L. A. Rusch, and M. Popović, "A wearable microwave antenna array for time-domain breast tumor screening," *IEEE Transactions on Medical Imaging*, vol. 35, no. 6, pp. 1501–1509, June 2016.
- [11] D. Byrne, M. Sarafianou, and I. J. Craddock, "Compound radar approach for breast imaging," *IEEE Transactions on Biomedical Engineering*, vol. 64, no. 1, pp. 40–51, Jan 2017.
- [12] A. W. Preece, I. Craddock, M. Shere, L. Jones, and H. L. Winton, "Maria m4: clinical evaluation of a prototype ultrawideband radar scanner for breast cancer detection," *Journal of Medical Imaging*, vol. 3, pp. 3 – 3 – 7, 2016. [Online]. Available: <https://doi.org/10.1117/1.JMI.3.3.033502>
- [13] N. K. Nikolova, "Microwave imaging for breast cancer," *IEEE Microwave Magazine*, vol. 12, no. 7, pp. 78–94, Dec 2011.
- [14] C. Li, V. M. Lubecke, O. Boric-Lubecke, and J. Lin, "Sensing of life activities at the human-microwave frontier," *IEEE Journal of Microwaves*, vol. 1, no. 1, pp. 66–78, 2021.
- [15] J. Ferlay, M. Colombet, I. Soerjomataram, C. Mathers, D. Parkin, M. Piñeros, A. Znaor, and F. Bray, "Estimating the global cancer



- 
- incidence and mortality in 2018: Globocan sources and methods,” *International Journal of Cancer*, vol. 144, no. 8, pp. 1941–1953, 2019. [Online]. Available: <https://onlinelibrary.wiley.com/doi/abs/10.1002/ijc.31937>
- [16] E. C. I. C. (ECIC). Estimates of cancer incidence and mortality in 2020. [Online]. Available: <https://ecis.jrc.ec.europa.eu/explorer>
- [17] C. L. Brace, “Radiofrequency and microwave ablation of the liver, lung, kidney, and bone: what are the differences?” *Current Problems in Diagnostic Radiology*, vol. 38, no. 3, pp. 135–143, 2009.
- [18] W. Zhou, X. Zha, X. Liu, Q. Ding, L. Chen, Y. Ni, Y. Zhang, Y. Xu, L. Chen, Y. Zhao, and S. Wang, “Us-guided percutaneous microwave coagulation of small breast cancers: a clinical study,” *Radiology*, vol. 263, no. 2, pp. 364–373, 2012.
- [19] Y. Park, D. Choi, H. K. Lim, H. Rhim, Y.-s. Kim, S. H. Kim, and W. J. Lee, “Growth rate of new hepatocellular carcinoma after percutaneous radiofrequency ablation: Evaluation with multiphase ct,” *American Journal of Roentgenology*, vol. 191, no. 1, pp. 215–220, 2008.
- [20] N. Medical. Neuwave™ percutaneous microwave ablation system. [Online]. Available: <https://www.jnjmedicaldevices.com/en-US/product/neuwave-microwave-ablation-system-percutaneous>
- [21] Y.-K. Hue, A. R. Guimaraes, O. Cohen, E. Nevo, A. Roth, and J. L. Ackerman, “Magnetic resonance mediated radiofrequency ablation,” *IEEE Transactions on Medical Imaging*, vol. 37, no. 2, pp. 417–427, 2018.
- [22] J. Short and P. Turner, “Physical hyperthermia and cancer therapy,” *Proceedings of the IEEE*, vol. 68, no. 1, pp. 133–142, 1980.
- [23] E. V. Sonnenberg, W. McMullen, and L. Solbiati, Eds., *Tumor Ablation Principles and Practice*, 1st ed. Springer-Verlag New York, 2005.
- [24] T. J. Vogl, T. Helmberger, M. G. Mack, and M. F. Reiser, Eds., *Percutaneous Tumor Ablation in Medical Radiolog*, 1st ed. Springer-Verlag Berlin Heidelberg, 2008.

- [25] M. Ahmed, C. L. Brace, F. T. Lee, and S. N. Goldberg, "Principles of and advances in percutaneous ablation," *Radiology*, vol. 258, no. 2, pp. 351–369, 2011.
- [26] J. Mendecki, E. Friedenthal, and C. Botstein, "Microwave applicators for localized hyperthermia treatment of malignant tumors," *Journal of Bioengineering*, vol. 1, pp. 511–518, 1977.
- [27] Jozef Mendecki, Esther Friedenthal, Charles Botstein, Fred Sterzer, Robert Paglione, Markus Nowogrodzki, and Elvira Beck, "Microwave-induced hyperthermia in cancer treatment: Apparatus and preliminary results," *International Journal of Radiation Oncology\*Biological\*Physics*, vol. 4, no. 11, pp. 1095–1103, 1978. [Online]. Available: <https://www.sciencedirect.com/science/article/pii/0360301678900263>
- [28] L. Taylor, "Implantable radiators for cancer therapy by microwave hyperthermia," *Proceedings of the IEEE*, vol. 68, no. 1, pp. 142–149, 1980.
- [29] C. Brace, "Thermal Tumor Ablation in Clinical Use," *IEEE Pulse*, vol. 2, no. 5, pp. 28–38, Sep. 2011.
- [30] M. F. Meloni, J. Chiang, P. F. Laeseke, C. F. Dietrich, A. Sannino, M. Solbiati, E. Nocerino, C. L. Brace, and F. T. Lee, JR, "Microwave ablation in primary and secondary liver tumours: technical and clinical approaches," *International Journal of Hyperthermia*, vol. 33, no. 1, pp. 15–24, 2017.
- [31] S. Sartori, F. Di Vece, F. Ermili, and P. Tombesi, "Laser ablation of liver tumors: An ancillary technique, or an alternative to radiofrequency and microwave?" *World Journal of Radiology*, vol. 9, no. 3, pp. 91–96, 2017.
- [32] P. Tombesi, F. D. Vece, L. Bianchi, and S. Sartori, "Thermal Ablation of Liver Tumours: How the Scenario Has Changed in the Last Decade," *European Medical Journal*, vol. 6, no. 1, pp. 88–94, May 2018.
- [33] C. Gabriel, *Compilation of the dielectric properties of body tissues at RF and microwave frequencies*. King's College London, 1996. [Online]. Available: <https://apps.dtic.mil/sti/pdfs/ADA309764.pdf>

- 
- [34] Z. Ji and Christopher L. Brace, "Expanded modeling of temperature-dependent dielectric properties for microwave thermal ablation," *Physics in Medicine and Biology*, vol. 56, no. 16, Jul. 2011.
- [35] V. Lopresto, R. Pinto, G. A. Lovisolo, and M. Cavagnaro, "Changes in the dielectric properties of ex vivo bovine liver during microwave thermal ablation at 2.45 ghz," *Physics in Medicine and Biology*, vol. 57, no. 8, Apr. 2012.
- [36] H. Fallahi, J. Sebek, and P. Prakash, "Broadband dielectric properties of ex vivo bovine liver tissue characterized at ablative temperatures," *IEEE Transactions on Biomedical Engineering*, vol. 68, no. 1, pp. 90–98, 2021.
- [37] C. Ianniello, J. A. de Zwart, Q. Duan, C. M. Deniz, L. Alon, J. S. Lee, R. Lattanzi, and R. Brown, "Synthesized tissue-equivalent dielectric phantoms using salt and polyvinylpyrrolidone solutions." *Magnetic resonance in medicine*, vol. 80, no. 1, p. 413–419, 2018.
- [38] S. Abedi, N. Joachimowicz, O. Meyer, D. Picard, and H. Roussel, "Phantoms for a novel generation of medical microwave imaging devices," in *2019 13th European Conference on Antennas and Propagation (EuCAP)*, 2019, pp. 1–4.
- [39] M. S. Khan, M. Hawlitzki, S. M. Taheri, G. Rose, B. Schweizer, and A. Brensing, "Investigation of microwave ablation process in sweet potatoes as substitute liver," *Sensors*, vol. 21, no. 11, 2021. [Online]. Available: <https://www.mdpi.com/1424-8220/21/11/3894>
- [40] S. Nelson, W. Forbus Jr., and K. Lawrence, "Permittivities of fresh fruits and vegetables at 0.2 to 20 ghz," pp. 81–93, 1994.
- [41] M. Bedoya, A. M. del Rio, J. Chiang, and C. L. Brace, "Microwave ablation energy delivery: Influence of power pulsing on ablation results in an ex vivo and in vivo liver model," *Medical Physics*, vol. 41, no. 12, p. 123301, 2014. [Online]. Available: <https://aapm.onlinelibrary.wiley.com/doi/abs/10.1118/1.4901312>
- [42] M. Jelbuldina, A. Korobeinyk, S. Korganbayev, D. Tosi, K. Dukenbayev, and V. J. Inglezakis, "Real-time temperature monitoring in liver during magnetite nanoparticle-enhanced microwave ablation with fiber

- bragg grating sensors: Ex vivo analysis," *IEEE Sensors Journal*, vol. 18, no. 19, pp. 8005–8011, 2018.
- [43] M. Wang, R. Scapatucci, M. Cavagnaro, and L. Crocco, "Towards a microwave imaging system for continuous monitoring of liver tumor ablation: Design and in silico validation of an experimental setup," *Diagnostics*, vol. 11, no. 5, 2021. [Online]. Available: <https://www.mdpi.com/2075-4418/11/5/866>
- [44] R. Scapatucci, G. G. Bellizzi, M. Cavagnaro, V. Lopresto, and L. Crocco, "Exploiting Microwave Imaging Methods for Real-Time Monitoring of Thermal Ablation," *International Journal of Antennas and Propagation*, vol. 2017, no. 1, p. 13, October 2017.
- [45] K. Kanazawa, K. Noritake, Y. Takaishi, and S. Kidera, "Microwave imaging algorithm based on waveform reconstruction for microwave ablation treatment," *IEEE Transactions on Antennas and Propagation*, vol. 68, no. 7, pp. 5613–5625, 2020.
- [46] S. Kidera, L. M. Neira, B. D. Van Veen, and S. C. Hagness, "Tdoa-based microwave imaging algorithm for real-time microwave ablation monitoring," *International Journal of Microwave and Wireless Technologies*, vol. 10, no. 2, pp. 169–178, 2018.
- [47] D. B. Rodrigues, P. F. Maccarini, S. Salahi, T. R. Oliveira, P. J. S. Pereira, P. Limão-Vieira, B. W. Snow, D. Reudink, and P. R. Stauffer, "Design and optimization of an ultra wideband and compact microwave antenna for radiometric monitoring of brain temperature," *IEEE Transactions on Biomedical Engineering*, vol. 61, no. 7, pp. 2154–2160, July 2014.
- [48] P. R. Stauffer, B. W. Snow, D. B. Rodrigues, S. Salahi, T. R. Oliveira, D. Reudink, and P. F. Maccarini, "Non-invasive measurement of brain temperature with microwave radiometry: Demonstration in a head phantom and clinical case," *The Neuroradiology Journal*, vol. 27, no. 1, pp. 3–12, 2014, pMID: 24571829. [Online]. Available: <https://doi.org/10.15274/NRJ-2014-10001>
- [49] R. Scheeler, E. F. Kuester, and Z. Popović, "Sensing depth of microwave radiation for internal body temperature measurement,"

- 
- IEEE Transactions on Antennas and Propagation*, vol. 62, no. 3, pp. 1293–1303, March 2014.
- [50] B. Stec, A. Dobrowolski, and W. Susek, “Multifrequency microwave thermograph for biomedical applications,” *IEEE Transactions on Biomedical Engineering*, vol. 51, no. 3, pp. 548–550, 2004.
- [51] M. S. Khan, G. Rose, B. Schweizer, and A. Brensing, “Em-thermal co-simulation of microwave ablation applicator in liver tissue phantom with bowtie-slot surface antenna,” in *2020 14th European Conference on Antennas and Propagation (EuCAP)*, 2020.
- [52] *N1501A Dielectric Probe Kit 10 MHz to 50 GHz*, Keysight Technologies, Lyoner Str. 20, 60528 Frankfurt am Main. [Online]. Available: <https://www.keysight.com/us/en/assets/7018-04631/technical-overviews/5992-0264.pdf>
- [53] H. H. Pennes, “Analysis of tissue and arterial blood temperatures in the resting human forearm,” *Journal of Applied Physiology*, vol. 1, no. 2, pp. 93–122, 1948, PMID: 18887578. [Online]. Available: <https://doi.org/10.1152/jappl.1948.1.2.93>
- [54] M. Hawlitzki, “Aufbau und charakterisierung eines mikrowellenhochleistungsmessstands zur ablation simulation an gewebephantomen,” Bachelor’s thesis, RheinMain University of Applied Sciences, Am Brückweg 26, 65428 Rüsselsheim, Nov. 2020.
- [55] *KUSG 2.45-250 A2.45 GHz ISM-Band Microwave Generator*, v1.0.3 ed., Kuhne electronic GmbH, Scheibenacker 3, 95180 Berg, Germany, Jul. 2021. [Online]. Available: <https://www.kuhne-electronic.de/funk/de/shop/KUSG245250AMikrowellengenerator/?card=1767>
- [56] S. M. Taheri, “Ex-vivo untersuchung der mikrowellenablation an rinderleber,” Master’s thesis, RheinMain University of Applied Sciences, Am Brückweg 26, 65428 Rüsselsheim, 2021.
- [57] S. Niehues, J. Unger, and M. Malinowski, “Liver volume measurement: reason of the difference between in vivo ct-volumetry and intraoperative ex vivo determination and how to cope it,” *European Journal of Medical Research*, 2010.

- [58] A. Kakimov, A. Suychinov, A. Tsoy, N. Mustambayev, N. Ibragimov, N. Kuderinova, G. Mirasheva, and Z. Yessimbekov, "Nutritive and biological value of liver and blood of various slaughtered animals," *Journal of Pharmaceutical Research International*, pp. 1–5, 2018.
- [59] Keysight, *N1501A Dielectric Probe Kit*, Keysight Technologies 2000–2021, Herrenberger Strasse 130 71034 Böblingen, Germany, May 2020. [Online]. Available: <https://www.keysight.com/de/de/assets/7018-04631/technical-overviews/5992-0264.pdf>
- [60] S. Sikdar, "Entwicklung eines gewebephantoms zur mikrowellen-diagnostik von thermischen ablationen," Bachelor's thesis, RheinMain University of Applied Sciences, Am Brückweg 26, 65428 Rüsselsheim, Jul. 2019.
- [61] M. Heil, "Mikrowellen-reflexionsverfahren zur bestimmung der permittivität von verlustbehafteten dielektrika," Bachelor's thesis, RheinMain University of Applied Sciences, Am Brückweg 26, 65428 Rüsselsheim, Feb. 2019.
- [62] A. Moukam, "Untersuchung von mikrowellen eigenschaften von wässrigen triton x-100 lösungen," Bachelor's thesis, RheinMain University of Applied Sciences, Am Brückweg 26, 65428 Rüsselsheim, Feb. 2020.
- [63] E. Oezkan, "Entwicklung eines mehrschicht-gewebephantoms für die mikrowellen-ablation," Bachelor's thesis, RheinMain University of Applied Sciences, Am Brückweg 26, 65428 Rüsselsheim, Nov. 2020.
- [64] S. Zealouk, "Bestimmung der komplexen permittivität von flüssigkeiten bei 2,45 ghz mittels eines mikrowellen-reflexionsverfahren," Bachelor's thesis, RheinMain University of Applied Sciences, Am Brückweg 26, 65428 Rüsselsheim, Nov. 2020.
- [65] C. Oumhamed, "Entwicklung eines gewebephantoms mit einer fettschicht für die mikrowellenablation," Bachelor's thesis, RheinMain University of Applied Sciences, Am Brückweg 26, 65428 Rüsselsheim, 2021.
- [66] S. Sikdar, "Rekonstruktion der räumlichen ausdehnung von gewebeeränderungen in der mikrowellen-ablation," Master's thesis, Rhein-

- 
- Main University of Applied Sciences, Am Brückweg 26, 65428 Rüsselsheim, 2021.
- [67] M. Hawlitzki, “Multi-antennenmessung der mikrowellenablation an phantomkörpern,” Master’s thesis, RheinMain University of Applied Sciences, Am Brückweg 26, 65428 Rüsselsheim, Dec. 2021.
- [68] M. Riedel, “Fiber-optic temperature measurement solves hv challenges in e-mobility,” imc Test Measurement GmbH, Voltastr. 5, 13355 Berlin, Germany, Tech. Rep., 2021. [Online]. Available: [https://www.imc-tm.com/fileadmin/Public/Downloads/Whitepapers/WP\\_EN/WP\\_eng\\_Fiber-optic\\_Measurement\\_Technology\\_RESEAU\\_MESURE.pdf](https://www.imc-tm.com/fileadmin/Public/Downloads/Whitepapers/WP_EN/WP_eng_Fiber-optic_Measurement_Technology_RESEAU_MESURE.pdf)
- [69] *Luxtron m920 Serie*, LumaSense Technologies, 3033 Scott Blvd. Santa Clara, CA 95054, 2021. [Online]. Available: <https://www.advancedenergy.com/de/products/temperature-measurement-products/fiber-optic-temperature-sensors/luxtron-m920-series/>
- [70] C. L. Brace, “Microwave tissue ablation: Biophysics, technology, and applications,” *Critical Reviewstrade; in Biomedical Engineering*, vol. 38, no. 1, pp. 65–78, 2010.
- [71] A. Z. Ibitoye, E. O. Nwoye, A. M. Aweda, A. A. Oremosu, C. C. Anunobi, and N. O. Akanmu, “Microwave ablation of ex vivo bovine tissues using a dual slot antenna with a floating metallic sleeve,” *International Journal of Hyperthermia*, vol. 32, no. 8, pp. 923–930, 2016, pMID: 27431435. [Online]. Available: <https://doi.org/10.1080/02656736.2016.1211323>
- [72] M. Dimitri, F. Staderini, M. Brancadoro, F. Frosini, A. Coratti, L. Capineri, A. Corvi, F. Cianchi, and G. B. Gentili, “A new microwave applicator for laparoscopic and robotic liver resection,” *International Journal of Hyperthermia*, vol. 36, no. 1, pp. 75–86, 2019, pMID: 30484344. [Online]. Available: <https://doi.org/10.1080/02656736.2018.1534004>
- [73] C. Hessinger née Reimann, B. Bazrafshan, M. Schüßler, S. Schmidt, C. Schuster, F. Hübner, T. J. Vogl, and R. Jakoby, “A dual-mode coaxial

- slot applicator for microwave ablation treatment,” *IEEE Transactions on Microwave Theory and Techniques*, vol. 67, no. 3, pp. 1255–1264, 2019.
- [74] *EMPRINT™ SX NAVIGATION ANTENNAS AND ACCESSORIES*, MEDTRONIC COVIDIEN, 710 Medtronic Parkway, Minneapolis, MN, 55432-5604, USA. [Online]. Available: <https://www.medtronic.com/covidien/en-us/products/ablation-systems/emprint-sx-ablation-system-accessories.html>
- [75] *Formable microwave cable*, HUBER+SUHNER, Mehlbeerenstrasse 6 Taufkirchen, Germany, Dec. 2020. [Online]. Available: [https://eu.mouser.com/datasheet/2/829/HUBER\\_2bSUHNER\\_SR\\_86\\_CU\\_TP\\_M17\\_COIL\\_DataSheet-1489480.pdf](https://eu.mouser.com/datasheet/2/829/HUBER_2bSUHNER_SR_86_CU_TP_M17_COIL_DataSheet-1489480.pdf)
- [76] X. Li, M. Jalilvand, Y. L. Sit, and T. Zwick, “A compact double-layer on-body matched bowtie antenna for medical diagnosis,” *IEEE Transactions on Antennas and Propagation*, vol. 62, no. 4, pp. 1808–1816, April 2014.
- [77] J. Jeong, K. Park, and C. Lee, “Design of cavity-backed bow-tie antenna with matching layer for human body application,” *Sensors*, vol. 19, no. 18, 2019. [Online]. Available: <https://www.mdpi.com/1424-8220/19/18/4015>
- [78] O. Fiser, V. Hruby, J. Vrba, T. Drizdal, J. Tesarik, J. Vrba, and D. Vrba, “Uwb bowtie antenna for medical microwave imaging applications,” *IEEE Transactions on Antennas and Propagation*, pp. 1–1, 2022.
- [79] U. Rafique, S. Pisa, R. Cicchetti, O. Testa, and M. Cavagnaro, “Ultra-wideband antennas for biomedical imaging applications: A survey,” *Sensors*, vol. 22, no. 9, 2022. [Online]. Available: <https://www.mdpi.com/1424-8220/22/9/3230>
- [80] *Manual ProtoMat S100*, Osteriede 7, D-30827 Garbsen., Feb. 2006. [Online]. Available: [http://www.lpkfusa.com/downloads/support/docs/man\\_s100.pdf](http://www.lpkfusa.com/downloads/support/docs/man_s100.pdf)
- [81] *SMA edge launch connector*, Würth Elektronik, Elsenheimerstr. 11, 80687 Munich, Germany, May 2018. [Online]. Available: <https://www.mouser.de/datasheet/2/445/60312202114514-1717657.pdf>



- 
- [82] RS®ZVL *Vector Network Analyzers*, Rohde Schwarz GmbH Co. KG, Muehldorfstrasse 15, 81671 Munich, Germany. [Online]. Available: [https://www.rohde-schwarz.com/de/produkt/zvl-produkt-startseite\\_63493-9014.html](https://www.rohde-schwarz.com/de/produkt/zvl-produkt-startseite_63493-9014.html)
- [83] M. S. Khan, B. Schweizer, A. Brensing, and G. Rose, "A circularly polarized patch antenna matched to liver surface with tx coupling medium," in *2021 IEEE International Symposium on Antennas and Propagation and USNC-URSI Radio Science Meeting (APS/URSI)*, 2021, pp. 811–812.
- [84] M. S. Khan, G. Rose, B. Schweizer, and A. Brensing, "Circularly polarized patch antenna matched to liver tissue with optimum placement positions," in *2021 15th European Conference on Antennas and Propagation (EuCAP)*, 2021, pp. 1–2.
- [85] S. Ahdi Rezaeieh, Y.-Q. Tan, and A. Abbosh, "Design of coupling medium for pulmonary edema microwave detection system," in *2013 IEEE Antennas and Propagation Society International Symposium (APSURSI)*, 2013, pp. 2057–2058.
- [86] L.-J. Xu, J.-P. Xu, Z.-J. Chu, S. Liu, and X. Zhu, "Circularly polarized implantable antenna with improved impedance matching," *IEEE Antennas and Wireless Propagation Letters*, vol. 19, no. 5, pp. 876–880, 2020.
- [87] Z. Xia, H. Li, Z. Lee, S. Xiao, W. Shao, X. Ding, and x. Yang, "A wideband circularly polarized implantable patch antenna for ism band biomedical applications," *IEEE Transactions on Antennas and Propagation*, vol. 68, no. 3, pp. 2399–2404, 2020.
- [88] M. Becvar, "Modellierung der signaldetektion durch mikrowellen antennen in medizinischer anwendung," Master's thesis, RheinMain University of Applied Sciences, Am Brückweg 26, 65428 Rüsselsheim, 2021.



# Ehrenerklärung

„Ich versichere hiermit, dass ich die vorliegende Arbeit ohne unzulässige Hilfe Dritter und ohne Benutzung anderer als der angegebenen Hilfsmittel angefertigt habe. Die Hilfe eines kommerziellen Promotionsberaters habe ich nicht in Anspruch genommen. Dritte haben von mir weder unmittelbar noch mittelbar geldwerte Leistungen für Arbeiten erhalten, die im Zusammenhang mit dem Inhalt der vorgelegten Dissertation stehen. Verwendete fremde und eigene Quellen sind als solche kenntlich gemacht.

Ich habe insbesondere nicht wissentlich:

- Ergebnisse erfunden oder widersprüchliche Ergebnisse verschwiegen,
- statistische Verfahren absichtlich missbraucht, um Daten in ungerechtfertigter Weise zu interpretieren,
- fremde Ergebnisse oder Veröffentlichungen plagiiert,
- fremde Forschungsergebnisse verzerrt wiedergegeben

Mir ist bekannt, dass Verstöße gegen das Urheberrecht Unterlassungs- und Schadensersatzansprüche des Urhebers sowie eine strafrechtliche Ahndung durch die Strafverfolgungsbehörden begründen kann.

Ich erkläre mich damit einverstanden, dass die Dissertation ggf. mit Mitteln der elektronischen Datenverarbeitung auf Plagiate überprüft werden kann.

Die Arbeit wurde bisher weder im Inland noch im Ausland in gleicher oder ähnlicher Form als Dissertation eingereicht und ist als Ganzes auch noch nicht veröffentlicht.“

Weinheim, 12.01.2024  
(Ort, Datum)

Muhammad Saad Khan  
(Unterschrift)

# Declaration of Honor

"I hereby declare that I produced this thesis without prohibited external assistance and that none other than the listed references and tools have been used. I did not make use of any commercial consultant concerning graduation. A third party did not receive any nonmonetary perquisites neither directly nor indirectly for activities which are connected with the contents of the presented thesis.

All sources of information are clearly marked, including my own publications.

In particular I have not consciously:

- Fabricated data or rejected undesired results.
- Misused statistical methods with the aim of drawing other conclusions than those warranted by the available data.
- Plagiarized data or publications.
- Presented the results of other researchers in a distorted way.

I do know that violations of copyright may lead to injunction and damage claims of the author and also to prosecution by the law enforcement authorities. I hereby agree that the thesis may need to be reviewed with an electronic data processing for plagiarism.

This work has not yet been submitted as a doctoral thesis in the same or a similar form in Germany or in any other country. It has not yet been published as a whole."

Weinheim, 12.01.2024  
(Place, Date)

Muhammad Saad Khan  
(Signature)